

LOW MODAL VOLUME SINGLE-CRYSTAL SAPPHIRE OPTICAL FIBER

William C. Hill

Dissertation submitted to the Faculty of
Virginia Polytechnic Institute and State University
in partial fulfillment of the requirements for the degree of

Doctor of Philosophy
in
Materials Science and Engineering

Gary R. Pickrell, Chair

William T. Reynolds

Thomas W. Staley

Anbo B. Wang

December 9, 2015

Blacksburg, VA

Keywords: Sapphire, modal volume, single mode, etching, optical fiber, optics

Copyright © 2015 W. Cary Hill

ABSTRACT

Low Modal Volume Single Crystal Sapphire Optical Fiber
William C. Hill

This research provides the first known procedure for cleanly and consistently reducing the diameter of single-crystal sapphire optical fiber (SCSF) below the limits of standard production methods, including the first production of subwavelength-diameter optical fiber (SDF) composed of single-crystal sapphire. The first known demonstration of an air-clad single crystal sapphire optical fiber demonstrating single-mode behavior is also presented, and the single-mode cutoff wavelength and diameter are determined.

Theoretical models describing and predicting the optical behavior of low modal volume sapphire optical fibers are also presented. These models are built upon standard weakly-guiding optical fiber theory, which is found to be accurate once experimentally-determined properties of the SCSF are substituted for theoretical values.

Reduced modal dispersion is also observed in the form of decreased laser pulse broadening in reduced-diameter SCSF. The improvements in spatial resolution for distributed sensing systems such as Raman distributed temperature sensing are also predicted based on the measured decrease in pulse duration.

This research also provides an enhanced understanding of the etching behavior of sulfuric and phosphoric acids on sapphire surfaces, including the first reporting of etching rates and activation energies for a-plane sapphire surfaces. Morphological changes of sulfuric and phosphoric acids at and beyond the temperature ranges used in etching were also tested and discussed in detail, especially regarding their practical impact on observed etching behavior.

The demonstration of LMV single-crystal sapphire optical fibers enables the adaptation of numerous sensing schemes requiring low modal volume or single-mode behavior to be utilized in extreme environments.

ACKNOWLEDGEMENTS

I would like to acknowledge financial support for significant portions of this work from the National Energy Technology Lab (NETL) at the U.S. Department of Energy (DOE) under contract DE-FE0012274. I would also like to thank my advisor, Dr. Gary Pickrell, for his constant assistance, support, and advice as this work was planned and enacted. I am especially grateful for Dr. Pickrell's patience and procurement of resources when I was initially learning the fundamentals of this field in which I had little prior knowledge or training.

The initial concept of applying a wet-acid etching method to sapphire optical fiber (which was fundamental to this research) was conceived by Dr. Dan Homa; I am grateful that he so freely discussed his initial findings with me and encouraged me to carry the work forward to its current state. Dan also provided key advice and training at numerous intervals in this research for which I am thankful in addition to his general mentorship. I also appreciate the advice, encouragement, and refining wisdom provided by my committee members: Dr. Bill Reynolds, Dr. Tom Staley (who allowed and monitored my experiments with caustic substances in his TGA), and Dr. Anbo Wang.

Dr. Zhihao Yu and Bo Liu provided patient advice whenever I sought their wisdom, which was extremely valuable in guiding the analysis of samples I produced. Bo provided crucial assistance in designing and setting up the modal analysis and modal dispersion measurement methods and was always willing to give his time and expertise freely and expediently and with admirable selflessness. Several of my group-mates and fellow

students have provided other support and assistance throughout this work, especially Adam Floyd and Yujie Cheng.

Personally, I thank my wife and twin boys (almost 4 years old at the time of this writing) for their continued patience and support. My wife, who could have balked and criticized when the timeline for this research stretched beyond what I expected instead provided constancy, understanding, and companionship, which I will always remember as a cornerstone of her character. My boys slept through the night most of the time, the helpfulness of which cannot be overstated. Most of all, I thank the Lord Jesus for the life, skills, and brain given to me, such as they are. I simply would not have even attempted to complete this degree with a wife and twins to support without full faith that I was merely following a path set before me and all our needs would be provided. He has indeed proved faithful.

I'll also thank the reader of this dissertation, whomever it may be to come across this work beyond those directly involved with its review and defense. I hope that some of the information in here proves useful to your own endeavors, and that you'll continue to contribute to the field by building upon (or if need be, correcting) the conclusions presented in this body of work.

Table of Contents

Abstract	ii
Acknowledgements	iii
List of Figures	vii
List of Tables	xiii
1 Introduction and Motivation	1
2 Theoretical Background	6
2.1 Modal Volume Reduction.....	6
2.1.1 Modal Volume: Exact Calculations	8
2.1.2 Modal Volume Estimates	15
2.1.3 Modal Volume Calculation Comparison	18
2.1.4 Methods for Reducing Modal Volume.....	19
2.1.5 Methods for Measuring Modal Volume	24
2.2 Numerical Aperture Measurement.....	34
2.3 Core Confinement.....	37
2.3.1 Poynting Vector Derivation	38
2.3.2 Core Confinement Calculations	40
2.4 Wet-Acid Etching Chemistry	42
2.4.1 Historical Overview: Wet Etching of Sapphire Components	42
2.4.2 Etch Deposits.....	45
3 Experimental Procedures	48
3.1 Sapphire Optical Fiber Etching Procedure	48
3.1.1 Etch Equipment Evolution	48
3.1.2 Method for Producing Low-Modal Volume Sapphire Optical Fiber	53
3.1.3 Etching Equipment for Production of LMV Sapphire Fiber.....	59
3.1.4 Sample Mounting and Preparation	65
3.2 Optical Analysis Methods	69
3.2.1 Far-Field Projection Modal Volume Measurement Method	69
3.2.2 Numerical Aperture Measurement.....	74
3.2.3 Modal Dispersion and Laser Pulse Broadening Measurement	75
4 Results and Discussion	78
4.1 Etch Reaction Chemistry.....	78

4.1.1	Chemical Analysis of Etching Solution.....	78
4.1.2	Initial Measured Etch Rates of Sapphire Optical Fiber.....	87
4.1.3	Etching Rates.....	90
4.1.4	Differences in c-plane and a-plane Etching Behavior.....	95
4.1.5	Etched Fiber Diameter Consistency and Surface Cleanliness.....	99
4.2	Reduced Diameter Single-Crystal Sapphire Optical Fibers.....	103
4.2.1	Submicron Diameter Sapphire Fiber.....	103
4.2.2	Tapered Sapphire Optical Fiber.....	104
4.3	LMV Sapphire Fiber Analysis.....	112
4.3.1	Numerical Aperture of LMV Sapphire Optical Fiber.....	112
4.3.2	Reduced Laser Pulse Broadening and Modal Dispersion.....	114
4.3.3	LMV Sapphire Optical Fiber Measurements.....	117
4.3.4	Mode Propagation Stability.....	121
4.3.5	Discussion of Observed Results in Comparison with Theoretical Models.....	127
5	Conclusions.....	131
6	Future Work.....	135
	References.....	136
	Appendix A: Refractive Index of Sapphire vs. Wavelength.....	141
	Appendix B: Mathematica Code.....	142
	Appendix B.1: Modal Volume Measurement.....	142
	Appendix B.2: Core Confinement.....	143

LIST OF FIGURES

Figure 1: Simplistic ray approach illustrating total internal reflection.....	7
Figure 2: At left, a simple mode with high core confinement is represented (where regions of highest intensity are red and lowest are blue). At right, a more complex, higher-order mode is illustrated. Mode illustrations provided by RP Fiber Calculator software.	7
Figure 3: Cylindrical coordinate system in an optical fiber.....	9
Figure 4: Radial intensity profiles of individual modes as described by the indices m and l ³⁹	13
Figure 5: 23 intersections are counted over all azimuthal indices for a fiber radius of $2\mu\text{m}$ and $\lambda=1450\text{nm}$	14
Figure 6: Eq. 19 estimates an extremely high number of modes supported by sapphire in air.	17
Figure 7: Maximum theoretical sapphire fiber radius for single-mode operation in air (i.e. the radius at which $V=2.405$ using the theoretical NA for air-clad sapphire). The change in slope near $\lambda=1.000\mu\text{m}$ is directly related to the measured change in refractive index of c-plane sapphire (Appendix 9.2).....	18
Figure 8: Comparison of V-number vs. number of modes for the precision calculation and the estimate reveals reasonable agreement.....	19
Figure 9: Numerical aperture of an overfilled waveguide can be determined through measurement of output beam widths W_1 and W_2 at distances D_1 and D_2 , yielding a vergence angle φ	36
Figure 10: Characteristic equation solution for the fundamental mode for $a = 200\text{nm}$ and $\lambda = 1500\text{nm}$. Axes are unitless.....	39
Figure 11: Fraction of power confined to core vs. core radius for $\lambda = 520\text{nm}$ (left) and $\lambda = 1500\text{nm}$ (right).	41
Figure 12: Relevant crystallographic orientations of sapphire. Yellow arrows indicate direction of etching for surface preparation of traditional sapphire wafers; green arrows represent direction of etching for reducing the diameter of a sapphire optical fiber in this research.	43

Figure 13: Insoluble etch products formed on the surface of a sapphire fiber in the location of the air-acid interface.....	46
Figure 14: Energy-Dispersive X-ray Spectroscopy (EDS) confirms the exclusive presence of a.) aluminum, b.) oxygen, and c.) sulfur in the crystalline deposits formed during etching. Composite image layered upon SEM image in d.).....	47
Figure 15: Refractory brick is hollowed out to support a beaker.....	49
Figure 16: Resistive heating wire is wound through the bottom plate.....	50
Figure 17: The heating plate is inserted with wire coiling to exit.....	50
Figure 18: Completed setup as it boils water in an initial test.....	51
Figure 19: Completed U-shaped setup heating water.....	52
Figure 20: Larger hotplate-style equipment accommodates large Erlenmeyer flask.....	52
Figure 21: Prolific deposits adhered to the sapphire fiber at the air-acid interface (right) but were absent at segments fully immersed in the etching solution (left).....	54
Figure 22: Irremovable deposits accumulating at the air-acid interface during etching caused severe surface scattering during testing using a 532nm green laser.....	54
Figure 23: Etch deposits wicked into the borosilicate shielding tube and contaminated the fiber if it was not sealed properly.....	56
Figure 24: A hydrogen-oxygen torch on a rotating glass lathe was used to gently collapse the borosilicate tube around sapphire optical fiber to form a protective seal.....	57
Figure 25: The 125 μ m sapphire fiber was easily centered within a 140 μ m ID ferrule and then polished to a final lapping film grit of 0.1 μ m. The two-tone appearance of the image is an artifact of the CRT monitor.....	58
Figure 26: External tube protects the sapphire fiber device from accidental breakage while allowing access to the etching fiber region.....	59
Figure 27: Shielded, protected sapphire fiber during testing after etching.....	59

Figure 28: A fused quartz tube with one end collapsed forms the primary containment vessel.....	60
Figure 29: Porous aluminosilicate rings added thermal mass surrounding the quartz tube.	61
Figure 30: Graphical illustration of the winding of the resistive heating wire (represented in gray) through porous aluminosilicate rings.....	62
Figure 31: Completed etching apparatus used in production of LMV sapphire samples.	63
Figure 32: Heating profile of a 16-hour etching session as monitored and recorded by the datalogging thermometer.....	64
Figure 33: Etch deposits completely covering a sapphire fiber after 6 hours at 310°C.....	66
Figure 34: EDS of beaker deposits indicates high silicon, phosphorus, and oxygen content.	67
Figure 35: Silica fiber (right) does not etch after 7 hours at 340°C; sapphire etches as expected (left).....	67
Figure 36: Teflon was used to securely mount fiber samples for initial etching studies. Fiber locations are circled.	69
Figure 37: Shielded, connected sapphire optical fiber during testing using a 532nm laser.	72
Figure 38: A stereoscope mounted to observe polishing of few-micron-diameter sapphire fiber proved necessary to ensure proper polishing occurred without breaking the miniscule fiber	73
Figure 39. Preferential etching of the r-plane (left) causes faceting on the fiber endface (right), which must be polished to prevent distortion of far-field patterns.....	74
Figure 40: Far-field pattern of a 6.5µm-diameter sapphire fiber before polishing (left) and after polishing (right) using a 532nm laser.....	74
Figure 41: TGA of 98% sulfuric acid up to 300°C. Left axis and the green line represent the total % weight change with temperature, and the right axis and blue line represent the	

derivative of the % weight change per °C. Points of discussion are labeled, with temperature/weight% above and slope below.....	80
Figure 42: TGA of 85% phosphoric acid up to 700°C. Left axis and the green line represent the total % weight change with temperature, and the right axis and blue line represent the derivative of the % weight change per °C. Points of discussion are labeled.....	81
Figure 43: Rescaled TGA of 85% phosphoric acid up to 700°C reveals the temperature of diacid formation at a heating rate of 20°C/min.	82
Figure 44: The etching rate of sapphire fiber by phosphoric acid at 320°C is much greater if the phosphoric acid solution is fresh (left) compared with phosphoric acid that has been heated for several hours (right). Differences in coloration are due to use of polarizing filter during optical microscopy of the birefringent sapphire fiber to help discern fiber edges. ..	84
Figure 45: Heating of phosphoric acid to temperatures above 350°C for extended periods of time initiates dehydration of polyphosphoric acid to phosphorus pentoxide.....	85
Figure 46: EDS supports the assumption that the composition of the white powder formed after extended heating of phosphoric acid is indeed phosphorous pentoxide.....	86
Figure 47: Sapphire optical fiber diameter etch rate is much faster for 3:1 H ₂ SO ₄ :H ₃ PO ₄ than sulfuric acid or phosphoric acid alone at 320°C.	87
Figure 48: 200µm diameter sapphire fiber remained unchanged after 5.5 hours exposure to etch solution at 270°C.	89
Figure 49: The etch rate of sapphire optical fiber in 3:1 molar H ₂ SO ₄ :H ₃ PO ₄ increases as temperature increases.	89
Figure 50: Diameter of a sapphire fiber is reduced linearly during etching. Error bars are present but not visible in the chart, as measured variation along this single sample was very small.....	90
Figure 51: Published etch rates of c-plane sapphire as a function of reciprocal temperature ⁷⁶ . Reprinted with permission from the Electrochemical Society.	91
Figure 52: The measured etch rates of a-plane sapphire varied according to etchant composition.....	93

Figure 53: Significant occurrence of pitting and other surface defects were observed when using pure phosphoric acid as an etchant of a-plane sapphire at elevated temperatures (temperature during etching of pictured sapphire fiber was 365°C). 94

Figure 54: No discernible surface defects are observable when a 3:1 ratio of sulfuric and phosphoric acids are used to etch sapphire fiber at around 340°C. 95

Figure 55: Etch rate of a-plane sapphire by phosphoric acid versus temperature follows the expected linear fit through 350°C. Measured etch rates at 375°C, 385°C, and 395°C strongly deviate from linear behavior. 96

Figure 56: One sapphire fiber sample whose mode characteristics were measured tapered from 9.1µm at its base (left) to 6.5µm at its polished tip (right) over the course of its 10cm length. The two images are of different magnifications..... 102

Figure 57: The heating profile was consistent between processing of three separate 1-meter long sapphire fibers. 103

Figure 58: A 50µm diameter sapphire fiber was etched to a final minimum diameter of less than 800nm. 104

Figure 59: A temperature gradient of around 10°C is induced in the formation of tapered sapphire fibers. T1, red, represents the data recorded by the thermocouple tip located closer to the bottom of the vessel, while T2, green, was located a few centimeters higher. 105

Figure 60: The topmost exposed area of 50µm sapphire fiber was reduced to 25µm through etching. 106

Figure 61: The tip of a tapered sapphire fiber measured around 70nm in diameter. 106

Figure 62: The only deposit or defect visible along the entire length of a submicron-diameter fiber were small globules concentrated near the fiber tip. 107

Figure 63: SEM micrograph of globule analyzed using EDS..... 108

Figure 64: EDS analysis revealed globule to contain a.) oxygen, d.) phosphorous, and e.) sulfur. Other components of potential deposits such as b.) aluminum and c.) fluorine were not detected in the globule. 109

Figure 65: Overlay of EDS analysis highlights the presence of sulfur, phosphorous, and oxygen in the globule adhered to the sapphire fiber. 110

Figure 66: EDS spectrum reveals the only elements present in appreciable quantities are oxygen, fluorine, aluminum, phosphorous, and sulfur. Peaks around 0.3keV, 2.1keV, and 2.8keV are signatures from incidental carbon and the conductive gold/palladium coating. 110

Figure 67. A sapphire nanofiber tapers down to a measured diameter of less than 5nm at its tip 111

Figure 68. A sapphire microfiber demonstrated a bend radius of less than 10 μ m..... 112

Figure 69: The pulse duration of the reduced-diameter sapphire fiber (\sim 50 μ m diameter at one end and \sim 40 μ m at the other) was determined to be less than that of a standard 125 μ m sapphire fiber. 115

Figure 70: The conclusion that LP₀₁ and LP₁₁ modes were observed was supported by altering the injection angle of the laser light and observing the far-field patterns. The etched sapphire fiber with its tip diameter of 6.5 μ m is circled, though of course it is too small to be visible in the image. The polished tip of the fiber is inserted into a foil aperture in front of the beam profiler detector. 120

Figure 71: Use of the measured effective NA produces predictions that are perfectly in line with observed single-mode cutoff diameter and wavelength, contrasting predictions using the theoretical NA. 129

Figure 72: Use of precise modal volume calculation methods also indicates a single mode is supported for an air-clad 6.5 μ m-diameter sapphire fiber with an effective NA of 0.09 at λ =783nm (left) and λ =983 (right)..... 129

LIST OF TABLES

Table 1: Review of modal analysis methods applicable to optical fiber experimentation....	25
Table 2: Etching rates of relevant acids of c-plane sapphire reported by Dwikusama at 320°C.....	91
Table 3: Etching of sapphire fiber to a desired diameter can be conducted cleanly and predictably using the developed etching equipment. As the 1.7 μ m fiber was imaged at maximum magnification (1000x), the image at the bottom of the table is digitally enlarged for greater visibility.	100
Table 4: Three 1-meter length sapphire fibers etched separately under the same conditions and duration measured very similar in final diameter from one end to the other.	102
Table 5: The measured effective numerical apertures for air-clad sapphire fiber differs greatly from the theoretically-calculated numerical aperture of ~ 1.4	113
Table 6: Far-field patterns demonstrated reduced modal interference as fiber diameter was decreased, ultimately resulting in the appearance of LP ₀₁ and LP ₁₁ modes. The area circled in red in one of the images is incident light from elsewhere in the room during testing....	118
Table 7: Far-field patterns of the sapphire optical fiber with etched diameter of 6.5 μ m were largely similar regardless of whether light was input using direct free-space coupling or butt-coupled with SMF-28e or 50/125 step-index MMF patch cables.	121
Table 8: Far-field patterns captured from different lengths of SMF-28 were largely consistent for a given test wavelength regardless of fiber length or input condition. Interference (likely from unstripped cladding modes) was apparent at short lengths.....	122
Table 9: Far-field patterns were also consistent for various lengths of 50/125 step index MMF for a given test wavelength. The input method did significantly affect the observed far-field projections for MMF, unlike tested SMF or sapphire samples.....	124
Table 10: Lower-order modes from a SMF input into 2.5m length of MMF were still apparent, but higher-order modes appeared to be increasing in intensity.	126
Table 11: The input condition affected intensity of far-field projections of 125 μ m-diameter sapphire fiber at a wavelength of 532nm but did not drastically affect the modal interference pattern.....	127

1 INTRODUCTION AND MOTIVATION

Aluminum oxide finds use in a wide range of applications due to its many unique and useful properties. The most stable and commonly procured form of aluminum oxide is the α -alumina crystalline phase encountered naturally as the mineral corundum, exhibiting trigonal symmetry of the class $D_{3d}^6-R\bar{3}C$. Other metastable polymorphs of aluminum oxide exist with different crystallographic structures. Face-centered cubic (fcc) packing structures of Al_2O_3 are found in metastable γ , η (cubic), θ (monoclinic), and δ (tetragonal or orthorhombic) phases, while hexagonal-close-packed (hcp) structures are represented by the thermodynamically-stable α -phase (trigonal) and metastable χ (hexagonal) phase¹. These metastable polymorphs can be used in powder form as catalysts or in coatings, but are not used in bulk applications since temperatures required for sintering result in conversion to the thermodynamically stable α -phase.

Single-crystal α - Al_2O_3 is known by many names depending on its use and physical appearance. The base mineral corundum can be vibrantly colored by even trace amounts of other elements; ruby is formed by insertion of chromium into the lattice resulting in red hues, and traces of other elements such as iron or titanium yield a variety of colors that historically fall under the sapphire nomenclature.

Synthetic ultra-pure monolithic single crystal α -alumina is also given the sapphire label. Without trace elements added, single crystal sapphire is a transparent material that displays slight birefringence in directions other than its c-axis because of its trigonal crystal symmetry.

Initial uses of polycrystalline α -aluminum oxide took advantage of its physical properties such as its extreme hardness (9 out of 10 on the Mohs scale) in the machining of steels² and other related uses. As technology advanced, developments in manufacturing and energy generation processes required transparent materials able to withstand higher temperatures and pressures than conventional silica-based glasses, leading to development and use of single-crystal sapphire³ windows.

More recently, sapphire has been deemed valuable in the field of optical sensing due to its high melting point and corrosion resistance compared with traditional silica-based optical fibers. As methods for the production of high-purity single-crystal sapphire optical fibers (SCSF) were improved⁴, innovators began applying traditional sensing techniques to sapphire components, resulting in temperature⁵⁻⁷ and gas sensors⁸ with high levels of accuracy in extremely hot and corrosive environments. The advent of such resilient optical sensing devices enabled monitoring and control of high temperature processes, allowing continuous operation for longer periods of time than can be provided by glass and platinum-based sensors⁹.

However, sapphire is far from ideal for use in optical sensors and data transmitters. Its large refractive index relative to surrounding air and large core size results in an extremely high modal volume, which contributes to high loss, modal dispersion, and decreased detection sensitivity^{10,11}. These shortcomings reduce the contrast and resolution of established sensing techniques, prevent effective distributed sensing, and can even preclude the use of certain sensing methods altogether^{12,13}.

The extreme environments in which sapphire optics are applied prohibit the application of traditional cladding techniques to reduce the refractive index disparity, and current sapphire fiber fabrication methods are limited to production of relatively large fiber diameters (sapphire fibers measuring no less than 50 μ m in diameter are currently available commercially). As a result, sapphire-based optical devices are often inferior to silica counterparts in all regards excluding survivability. As sapphire remains the most promising material for extreme environment optics, reducing the modal volume of sapphire optical fibers below that of current commercially available items would enable tremendous advancements for sensing in high temperature and highly corrosive locations.

Tapered sapphire optical fibers have not yet been demonstrated in the literature, though the effects of tapering on an optical fiber's properties have been demonstrated in silica. Tapers can be used to increase the sensitivity of sensing schemes or produce spectral broadening^{14,15}, as well as reduce loss¹⁶⁻¹⁸ or even alter the mode field profile¹².

Other sensing methods are enabled when one or more dimensions of a waveguide are less than that of the light it is guiding. Very interesting and useful properties may be exploited; increased power in the evanescent field (the field of light guided outside the core of the optical fiber)^{18,19} enables higher-sensitivity gas detection²⁰⁻²³ and refractive index sensing^{24,25} than standard-diameter fibers, while a tapering effect can add increased sensing capabilities^{26,27}, reduce loss^{16,17}, and even introduce spectral broadening or supercontinuum generation (where the wavelength of light exiting the fiber shifts substantially from that which entered the fiber)²⁸.

Silica-based subwavelength-diameter fibers (SDF's) can be produced by modifying the standard manufacturing method and continuing the draw of the fiber until its diameter is sufficiently small^{29,30}. However, as the very properties that make sapphire ideal for high-temperature sensing prevent this type of manufacture, no successful attempts have previously been reported to produce a sapphire optical fiber with subwavelength diameter, or to describe its anticipated or observed properties.

The development of a procedure to predictably reduce the diameter of single crystal sapphire optical fiber from its commercially-obtainable size to diameters that support much lower modal volume represents an enormous step in the development of high temperature and extreme environment sensors. With modal dispersion reduced, the resolution in distributed sensing systems that has been demonstrated in silica optical fiber systems could be applied to their high-temperature sapphire counterparts, and production of single-mode sapphire fiber would enable utilization of features such as intrinsic Bragg gratings (sapphire FBG's) for enhanced reflectance-based strain and temperature sensing systems. The capability to further reduce sapphire optical fiber to subwavelength diameters also enables an entire class of evanescent field sensing; in addition to higher temperature survivability, sapphire SDF's do not suffer from attack by water vapor that is devastating to silica SDF's²³, meaning a sapphire SDF sensor has inherent value at normal operating temperatures in addition to extreme environments.

The remainder of this document describes the theoretical design considerations for LMV sapphire optical fiber, the experimental procedures used to produce these fibers, and the observed behavior of LMV sapphire devices; the correlation of observed data with

theoretical predictions is discussed as well as the practical implications of all findings on related sensor design.

2 THEORETICAL BACKGROUND

There are a plethora of important and interesting properties to consider when attempting to predict and model the useful qualities of a reduced-mode sapphire device. Two pertinent aspects to consider that encompass the majority of properties relevant to low-modal volume fiber are the calculation of supported modal volume and fraction of core confinement in a reduced-diameter device.

2.1 Modal Volume Reduction

A foundational principle in the field of fiber optics regards the fact that light can be guided by a transparent material if the refractive index of the *core* (the central portion in which light is transmitted) is greater than that of the *cladding* (the medium surrounding the core), forming a *waveguide*. Light is considered to be guided if the majority of its power is contained by the waveguide as it transmits from one position in the waveguide to another. The difference between the refractive indices of the core and cladding have a great effect on the angle at which light is internally reflected.

The core-cladding refractive index disparity is expressed as the sine of the maximum angle of acceptance for light entering the fiber, or the angle at which light may enter the fiber and be totally reflected internally rather than refracted through the cladding or reflected off the endface. This is known as the *numerical aperture* and is estimated mathematically in Eq.

1.³¹

$$NA = \frac{1}{n_0} \sqrt{n_{core}^2 - n_{cladding}^2} \quad \text{Eq. 1}$$

Where n_0 is the refractive index of the surrounding medium (typically air).

The principle of total internal reflection is most simply represented in ray-optics form by diagrams such as Figure 1. In this illustration, one can easily envision an optical fiber guiding rays of light through a series of repeated total internal reflections.

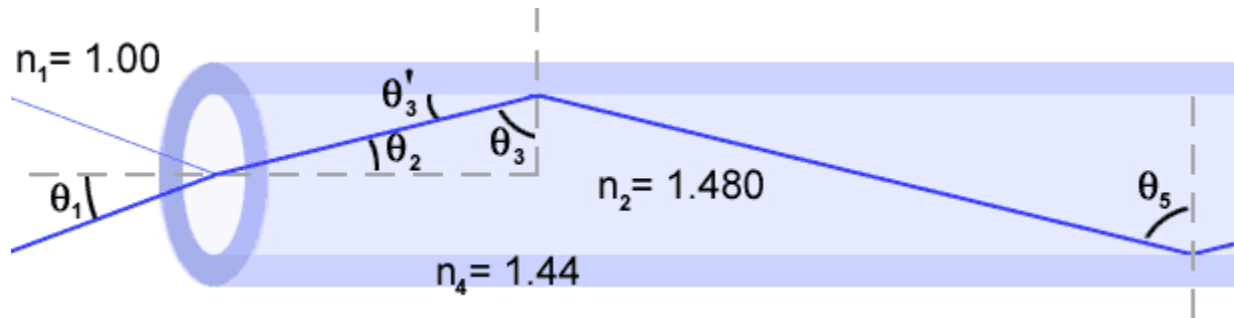


Figure 1: Simplistic ray approach illustrating total internal reflection³².

However, the transmittance of light through a waveguide is not nearly so simple. As light travels down the optical axis of a waveguide, it propagates in the form of distinct radial power distributions known as *modes*; two examples are illustrated in Figure 2. If an optical fiber supports the continued propagation of more than one mode, it is considered to be a *multimode fiber*.



Figure 2: At left, a simple mode with high core confinement is represented (where regions of highest intensity are red and lowest are blue). At right, a more complex, higher-order mode is illustrated. Mode illustrations provided by RP Fiber Calculator software³³.

High modal volume can present issues in many applications; higher-order modes contain more complex radial intensity distributions and are often more “lossy” than low-order modes, meaning they allow a higher percentage of light to propagate beyond the core region and into the cladding, where it typically cannot continue to propagate and eventually escapes.

As a result of the difference in core-cladding power distribution among modes, each mode is defined by its own *effective refractive index* which varies slightly from the refractive index of the baseline waveguide material, causing different modes to travel at slightly different velocities. This *modal dispersion* causes light to spread along its path as it traverses the waveguide, which can adversely affect a multimode waveguide’s transmission and sensing properties. Modal dispersion limits the rate of data transfer (the slowest modes of one packet of information must reach the sensor before the fastest modes of the next packet of information) and causes individual laser pulses to broaden in distributed sensing applications, reducing resolution.

2.1.1 Modal Volume: Exact Calculations

Modal volume can be predicted with high degrees of accuracy using complex derivations that encompass the entirety of relevant optical theory. While these equations are unwieldy, a few dozen lines of code in a program such as *Mathematica*³⁷ allows a computer to take out the complexity (provided enough memory and time for calculation). This section describes the derivation and use of precise modal volume calculations; deeper discussion of these derivations may be found in fundamental photonic and waveguide theory textbooks.^{31,38}

We will start with the Helmholtz equation as it is modified for a cylindrical coordinate system (Eq. 2). It will be helpful in envisioning the utility of these equations to keep the cylindrical coordinate system in mind as it relates to an optical fiber (Figure 3).

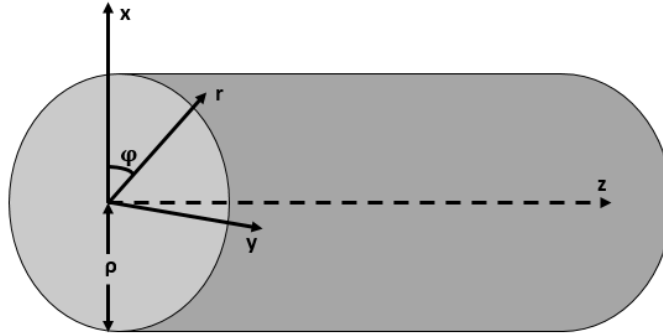


Figure 3: Cylindrical coordinate system in an optical fiber.

$$\frac{\delta^2 U}{\delta r^2} + \frac{1}{r} \frac{\delta U}{\delta r} + \frac{1}{r^2} \frac{\delta^2 U}{\delta \varphi^2} + \frac{\delta^2 U}{\delta z^2} + n^2 k_0^2 U = 0 \quad \text{Eq. 2}$$

Where U represents the field distribution ($U = U(r, \varphi, z)$), n is the refractive index (of core/cladding, to be distinguished later) and k_0 is the vacuum wavenumber ($k = \frac{2\pi}{\lambda}$).

Guided modes travel along the z -axis with unique propagation constants labeled β , which may be numerically determined after constraints are set to reduce unknown variables. The z -direction dependence of U is represented by $e^{-j\beta z}$. Since the angle φ is periodic, $U(\varphi)$ can take the harmonic form e^{-jlz} , where l is an integer representing the periodicity of the function.

By substitution of the $U(z)$ and $U(\varphi)$ relations, Eq. 2 becomes

$$\frac{d^2u}{dr^2} + \frac{1}{r} \frac{du}{dr} + \left(n^2(r)k_0^2 - \beta^2 - \frac{l^2}{r^2} \right) u = 0 \quad \text{Eq. 3}$$

A mode is bound if the value of its propagation constant is between that of the wavenumber in the core and cladding ($n_{cl}k_0 < \beta < n_{co}k_0$). We can use this relation to define two parameters to simplify future steps.

$$k_T^2 = n_{co}^2 k_0^2 - \beta^2 \quad \text{Eq. 4}$$

$$\gamma^2 = \beta^2 - n_{cl}^2 k_0^2 \quad \text{Eq. 5}$$

These relations can be used to distinguish the rate of change of field distribution in the core (using k_T) from that in the cladding (γ). Substitution into Eq. 3 results in distinct differential equations describing the field distribution of the core and cladding separately.

$$\frac{d^2u}{dr^2} + \frac{1}{r} \frac{du}{dr} + \left(k_T^2 - \frac{l^2}{r^2} \right) u = 0 \quad \text{for } r < a \text{ (core)} \quad \text{Eq. 6}$$

$$\frac{d^2u}{dr^2} + \frac{1}{r} \frac{du}{dr} - \left(\gamma^2 + \frac{l^2}{r^2} \right) u = 0 \quad \text{for } r > a \text{ (cladding)} \quad \text{Eq. 7}$$

Eq. 6 and Eq. 7 are standard differential equations whose solutions are two varieties of standard Bessel functions. Therefore, the solutions of these equations can be described by Eq. 8.

$$u(r) \propto \begin{cases} J_l(k_T r), & r < a \text{ (core)} \\ K_l(\gamma r), & r > a \text{ (cladding)} \end{cases} \quad \text{Eq. 8}$$

Where $J_l(x)$ is the Bessel function of the first kind and order l and $K_l(x)$ is the modified Bessel function of the second kind and order l . Mathematically, there are multiple solutions possible but only the real solution is relevant to these derivations.

The separation of $u(r)$ into distinct functions representing the core and cladding field distributions allows us to set an important boundary condition that will help reduce the number of unknown variables to a solvable quantity. We know that the field distribution must be continuous at the core-cladding interface, so we can begin to work toward an equation that takes advantage of this assumption.

First, we will normalize the parameters k_T and γ to the core radius and redefine them for convenience:

$$X = k_T a \quad \text{Eq. 9}$$

$$Y = \gamma a \quad \text{Eq. 10}$$

If we reason from Eq. 4 and Eq. 5 that the following statement is true:

$$k_T^2 + \gamma^2 = (n_1^2 - n_2^2)k_0^2 = (NA)^2 * k_0^2 \quad \text{Eq. 11}$$

Then we can arrive at Eq. 12 through substitution and simplification.

$$X^2 + Y^2 = V^2 \quad \text{Eq. 12}$$

Now, with these substitutions and simplifications in place, we can enforce our boundary condition, asserting that $u(r)$ is continuous and has a continuous derivative at the core-cladding interface (where $r = a$). This results in Eq. 13.

$$\frac{k_T a J_1'(k_T a)}{J_1(k_T a)} = \frac{\gamma a K_1'(\gamma a)}{K_1(\gamma a)} \quad \text{Eq. 13}$$

Changing the derivatives of the Bessel functions to their mathematical identities (Eq. 14 and Eq. 15) will simplify the final equation.

$$J_l'(x) = \pm J_{l\pm 1}(x) \pm l \frac{J_l(x)}{x} \quad \text{Eq. 14}$$

$$K_l'(x) = \pm K_{l\pm 1}(x) \pm l \frac{K_l(x)}{x} \quad \text{Eq. 15}$$

Substituting these identities into Eq. 13 along with the previously-established normalized parameters X and Y yields the *characteristic equation* for a step-index optical fiber:

$$X \frac{J_{l\pm 1}(X)}{J_l(X)} = Y \frac{K_{l\pm 1}(Y)}{K_l(Y)}, \quad Y = \sqrt{V^2 - X^2} \quad \text{Eq. 16}$$

Since we know V (dependent solely on the fiber's radius and refractive indices of core/cladding), we only have one unknown variable, X , for a given azimuthal index, l . The mode indices m and l describe the radial intensity pattern of a given mode in the manner illustrated in Figure 4 for several lower-order modes.

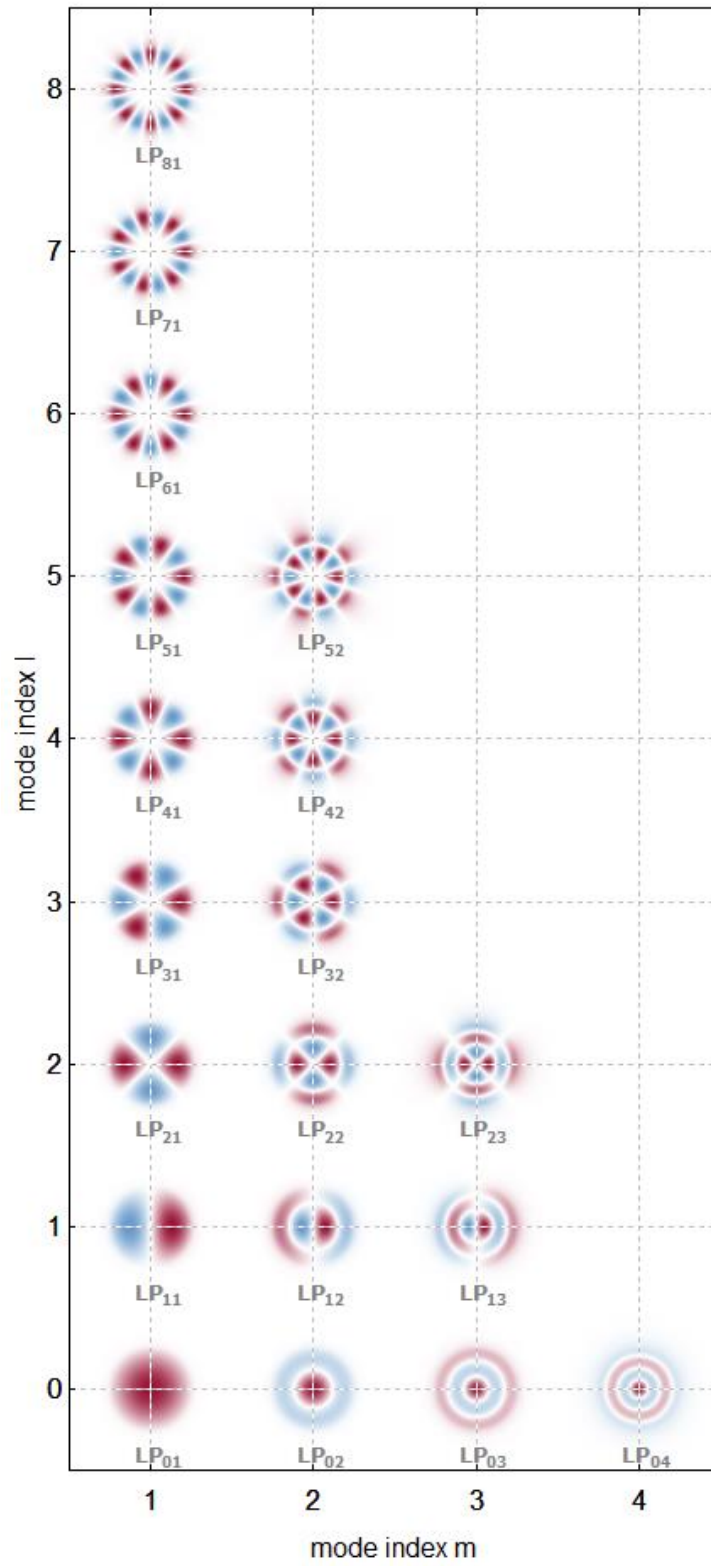


Figure 4: Radial intensity profiles of individual modes as described by the indices m and l ³⁹.

This equation will allow us to solve for the modal volume of our system by simply plotting the left-hand side (LHS) and right-hand side (RHS) of Eq. 16 together vs. X as $X \rightarrow V$ and counting the number of intersections of LHS and RHS (i.e. where LHS=RHS at a given value of X). Each intersection contains a value for the propagation constant (β) of a mode; since β is unique for each mode, the number of distinct propagation constants discovered is directly related to the total modal volume. A plot is made for each azimuthal index l and the number of modes represented by radial indices m are recorded, beginning with $l = 0$ and increasing l by integers until no solutions are found, then summing the total number of intersections to determine the total number of modes.

As an example, the process is illustrated in Figure 5 for a sapphire fiber in air with a radius of $2\mu\text{m}$ using a transmission wavelength of 1450nm . The maximum number of intersections is found when $l = 0$ and intersections continue to decrease until no solutions are found when $l = 10$.

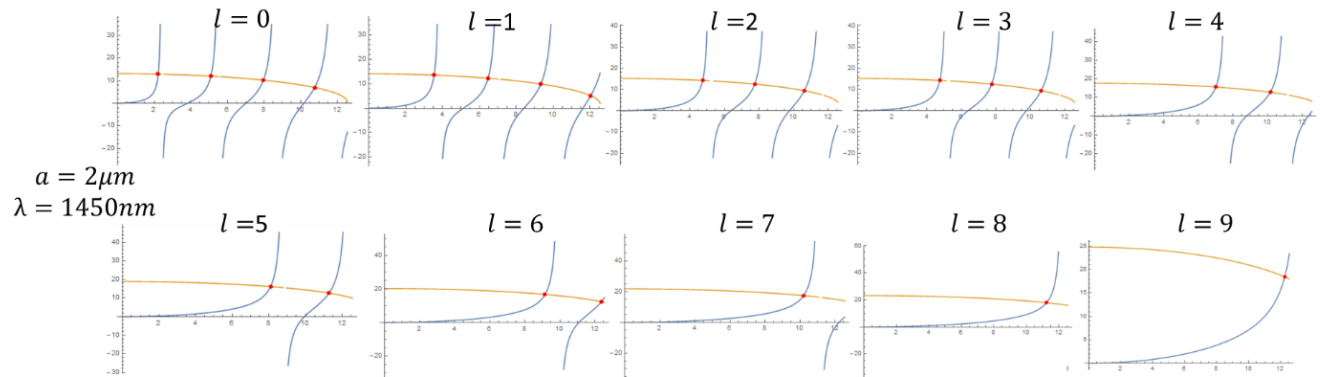


Figure 5: 23 intersections are counted over all azimuthal indices for a fiber radius of $2\mu\text{m}$ and $\lambda=1450\text{nm}$.

A total of 23 intersections can be counted for all azimuthal indices. Two modal polarizations are represented by every counted intersection, as well as another two helical polarities for every intersection except for those at $l = 0$. Therefore, for the 23

intersections counted above, a **total of 84 modes** are determined to be supported by this fiber system.

2.1.2 Modal Volume Estimates

Modal volume (the number of “bound” modes supported by a fiber) can be estimated numerically using a parameter referred to as the *V-number*, quantified in Eq. 17 (as derived from Eq. 12 and related mathematical substitutions). The following Eq. 17 through Eq. 19 may be found in most fundamental waveguide texts and are here displayed in the format presented by Saleh and Teich³¹.

$$V = \frac{2\pi}{\lambda} aNA \quad \text{Eq. 17}$$

Where λ is the wavelength of transmitted light, a is the radius of the core, and NA is the numerical aperture, defined previously in Eq. 1.

Essentially, a larger V-number indicates a larger number of supported modes. While the V-number itself is an exact, quantifiable parameter, using its value alone to predict the number of modes supported by a waveguide can only result in an estimate, as the propagation of modes is too complex to be modeled using such simple equations. The accepted estimation equations are therefore unable to accurately quantify very low modal volume (error is in the range of 50-200% depending on the estimation used when predicting the support of just a few modes) but quickly become accurate to within 8-10% as $V > 5$, and the amount of error becomes diminishingly small as V continues to increase.

There are several equations that may be used to estimate the number of modes supported by a waveguide using only the V-number. Each is suited for different geometries or

cladding types, such as a rectangular waveguide vs. circular fiber, or step-index cladding vs. graded index. For the purposes of modeling air-clad sapphire fibers the relation suited for a step-index fiber is best, where it is assumed that there is only one distinct value for the refractive index of the core or cladding.

$$M \approx \frac{4}{\pi^2} V^2 \quad \text{Eq. 18}$$

Eq. 18 is especially accurate at very high values of V (where V is well into the double digits, meaning the radius is very large, the wavelength is very small, and/or the refractive index difference between core and cladding is high). An alternative estimate is also accurate for step-index fibers, and tends to be more so at lower values of V (Eq. 19).

$$M \approx \frac{V^2}{2} \quad \text{Eq. 19}$$

It may be helpful at this point to give some practical numerical reference points for the equations and parameters just described. Because of the very large refractive index difference between sapphire and air ($n_{\text{sapphire}} \approx 1.76$ depending on wavelength and $n_{\text{air}} \approx 1$. The refractive index of silica is $\approx 1.45 - 1.55$ for reference³⁴), the calculated value for V based upon the theoretical NA is very large for unclad sapphire fiber, causing an extremely high number of modes to be supported. Figure 6 provides a graphical representation of the modal volume estimate for air-clad sapphire vs. wavelength using Eq. 19 and the theoretical numerical aperture based solely on refractive index of sapphire and air. These numbers are calculated assuming a core diameter of $50\mu\text{m}$, which is the smallest commercially available sapphire fiber diameter ever available at this time^{35,36}.

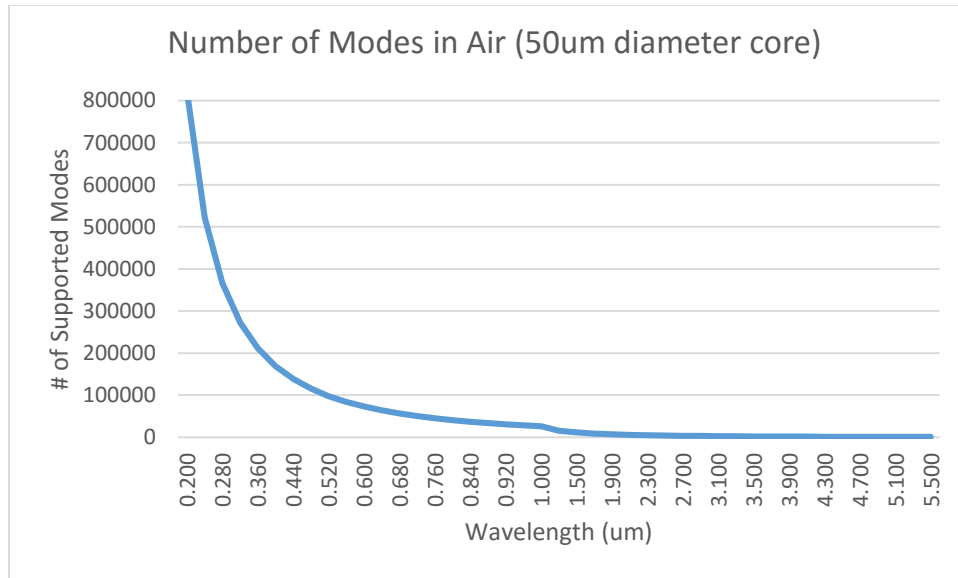


Figure 6: Eq. 19 estimates an extremely high number of modes supported by sapphire in air.

The estimation indicates that the number of modes supported by an unclad 50 μ m diameter sapphire optical fiber in air across its standard transmittable spectrum ranges from ~820,000 modes at $\lambda = 200nm$ to ~625 modes at $\lambda = 5500nm$; even at long wavelengths, many lossy higher-order modes will be supported.

It is also useful to calculate the maximum core radius that will only support one propagation mode (i.e. the largest single-mode sapphire fiber one can produce without cladding). While the number of modes using the V-number can only be estimated, the single-mode limit as it relates to fiber diameter can be calculated exactly. Using precise relations derived in Section 2.1.1, the single-mode limit occurs at $V = 2.405$. The maximum sapphire fiber radius where $V = 2.405$ based on theoretical NA vs. transmission wavelength is plotted graphically in Figure 7.

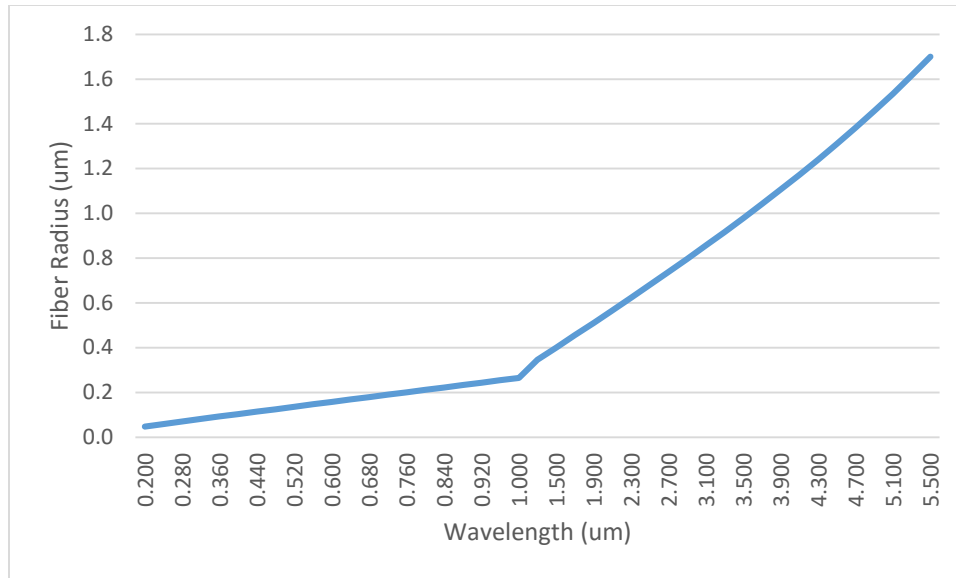


Figure 7: Maximum theoretical sapphire fiber radius for single-mode operation in air (i.e. the radius at which $V=2.405$ using the theoretical NA for air-clad sapphire). The change in slope near $\lambda=1.000\mu\text{m}$ is directly related to the measured change in refractive index of c-plane sapphire (Appendix 0)

Using this relation, it is determined that the theoretical maximum sapphire fiber diameter for single-mode operation in air is a miniscule 94nm at $\lambda = 200\text{nm}$ and $3.4\mu\text{m}$ at $\lambda = 5500\text{nm}$.

2.1.3 Modal Volume Calculation Comparison

The exact number of modes supported by a waveguide can be calculated using the process outlined in Section 2.1.1. However, as this method requires quite a bit of time and effort to complete (even with computer assistance), it is often more convenient to use one of the approximations previously described (Eq. 18 and Eq. 19).

Fortunately, these approximations are reasonably accurate, even at the relatively low V-number calculated for the system demonstrated in Figure 5. The exact number of modes calculated for this system (air-clad sapphire with radius $a = 2\mu\text{m}$ and wavelength $\lambda = 1450\text{nm}$) was found to be 84; the approximation of Eq. 19 estimates a reasonable 79

supported modes, and the amount of relative error for this approximation will only decrease as $V \rightarrow \infty$.

The Eq. 18 estimate ($M \approx \frac{4}{\pi^2} V^2$) is also found to be accurate; Figure 8 plots the V-number vs. calculated number of modes, where the exact modal volume is represented by the stair-step function and Eq. 18 is represented by the orange curve.

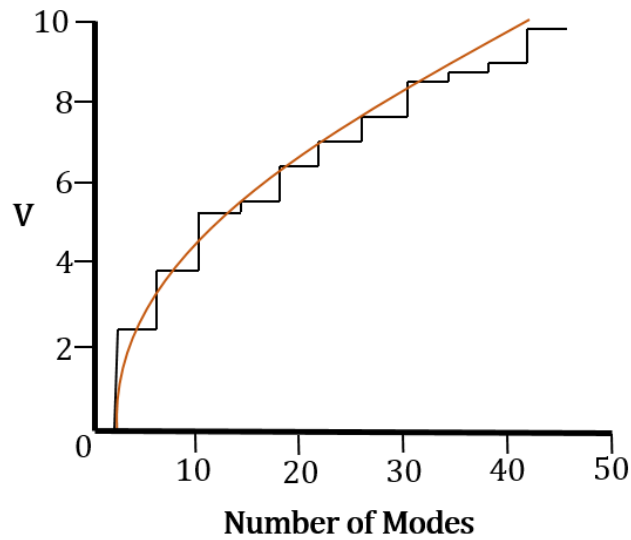


Figure 8: Comparison of V-number vs. number of modes for the precision calculation and the estimate reveals reasonable agreement.

2.1.4 Methods for Reducing Modal Volume

Since modal volume is a direct function of V in these estimations, lowering the V-number becomes the engineering focus when the production of LMV fibers is desired. It will be convenient to recall Eq. 17 at this point (with NA substituted for its equivalent terms).

$$V = \frac{2\pi}{\lambda} a \frac{1}{n_0} \sqrt{n_{co}^2 - n_{cl}^2} \quad \text{Eq. 20}$$

Survey of Eq. 20 reveals three possible methods for reducing the value of V . One may be to increase the value of the transmitted wavelength λ ; while this is very easily accomplished, it is not a practical solution since specific wavelengths are used for designed purposes (for example, low core material absorption wavelengths for low-loss transmission or wavelengths at which detectable gasses absorb strongly in sensing applications).

This leaves two viable methods for reducing modal volume if one would seek to retain freedom to tune the wavelength of transmitted light. One must either reduce the disparity between the refractive index of the core and cladding or reduce the radius of the fiber core. To some degree, designed optical fibers take both factors into account, though one parameter is typically given more attention depending on its end use.

Refractive Index Tuning: Claddings

Reducing the refractive index difference between core and cladding is the method most commonly attributed to modal volume reduction. There are three primary methods typically employed to tune the refractive index of the cladding so that it is only slightly less than that of the core.

The simplest method is to clad the fiber core with a material that has a slightly lower refractive index. In silica-based fibers, this is most commonly achieved by cladding the core with another glass containing specific additives or similarly doping the core to finely tailor the refractive index. The result is a *step-index* fiber, so-called because there is a distinct, constant difference between n_{core} and $n_{cladding}$ that is consistent at any point within the core or cladding. This model also applies to unclad fibers such as the sapphire-in-air model

that is most relevant to this research, where the sapphire fiber makes up the core and the surrounding air becomes the cladding as far as optical properties are concerned.

A second method involves cladding the core with a material that varies in composition radially from the core-cladding interface to the cladding-air interface using a very specific doping profile. The result is a *graded-index* fiber, where the refractive index difference may be very small near the core-cladding interface but then increases continuously outward.

One specific advantage of this type of cladding (in addition to modal volume reduction) is the ability to standardize the travel velocity of all supported modes. Since higher-order modes tend to travel more slowly than the fundamental modes and also propagate with more of their power near or into the cladding, a gradient-index profile can help reduce the difference in travel velocity and therefore increase the possible data transfer rate by reducing the time elapse between modal fronts of the same information pulse^{40,41}.

A third method involves the introduction of an arrangement of tubes or powder around the core of the fiber. The arrangement is then heated and/or drawn, resulting in a distribution of holes or pores that can be ordered or random depending on the design of the preform.

As long as the created holes or pores are within certain parameters, an effective *air-average index* is experienced by the transmitted light (i.e. the refractive index is somewhere in between that of the core material and air, reducing the overall refractive index of this region). While the function and utility of this method is much more complex than this simplistic explanation affords^{42,43}, the basic concept of so-called *holey optical fibers* can be understood in this manner.

Modal volume can also be altered through introduction of precisely uniform arrays of lengthwise holes forming a photonic crystal fiber (PCF)⁴⁴⁻⁴⁹. As the mechanism for modal manipulation in a PCF relies on an optical bandgap created by the periodic structure rather than altering the refractive indices of core and cladding, this variety of optical waveguide remains outside the scope of the previously described modal volume estimation methods.

Sapphire Cladding Difficulties

Cladding technology has been perfected for low-temperature optical fibers composed primarily of either polymers or silica and therefore is the preferred method for modal reduction and other such tailoring of favorable properties. However, high temperatures and harsh environments prevent seamless implementation of these tried-and-true cladding methodologies in application to sapphire optical fiber.

First of all, a suitable cladding must stand up to demands of use in high temperature and corrosive environments. The cladding itself must maintain its integrity at very high temperatures (sapphire optical fibers are usable up to $\sim 2000^{\circ}\text{C}$ depending on the sensing scheme^{7,50,51}) and must also have a coefficient of thermal expansion that is similar to that of sapphire to prevent delamination or other discontinuities. The cladding must be invulnerable or resistant to chemical attack in highly corrosive environments to qualify for use in many applications of interest.

Secondly, the cladding must not diffuse at these high service temperatures. Some effective traditional claddings utilize a specially-tailored dopant profile to achieve their fine refractive index matching which could change in a matter of hours in service, throwing off sensing calibrations and increasing the refractive index disparity that was so carefully

designed. If a cladding is formed from a single composition that happens to have a suitable refractive index (rather than using the core material as a base and adding dopants to adjust properties), it must also resist diffusion into the core, which could similarly disrupt properties and increase scattering.

Holey fibers are difficult to fabricate using sapphire, as its physical properties are such that many methods for producing pores in a silica fiber do not directly translate (similar to the difficulties in SDF fabrication described previously). To date, successful production of a random hole sapphire fiber has not been reported, though ordered-hole arrangements and sapphire PCF's have been demonstrated^{52,53}. Similar concepts could be applied to designed fiber geometries using masking and selective etching as an extension of the experimental work described later in this document.

Fiber Radius Reduction

The remaining method for reducing modal volume is to reduce the radius of the fiber core. This has been achieved in silica-based fibers through adjustment of the standard manufacturing parameters (specifically heat profile/temperature and draw rate) to reduce fiber radius. Through additional modification, silica fibers have been produced even down to subwavelength diameters^{18,22,23,28,30,54}.

Being crystalline rather than amorphous, sapphire does not soften like glass under heat and therefore cannot be drawn into fiber in this manner. Sapphire optical fibers must be grown from a seed crystal using equipment that requires high amounts of precision in its heating profile, material feed rate, and stage movement; restrictions in these parameters have resulted in a practical minimum sapphire fiber diameter of 50 μm or so^{35,36}. The most

common method for producing sapphire optical fiber is called laser-heated pedestal growth (LHPG) and is the method used by the manufacturer of SCSF used in this research.

2.1.5 Methods for Measuring Modal Volume

The total modal volume supported by a multimode fiber can be accurately estimated using the previously-described predictive equations and models, but it is difficult to verify experimentally. Fibers supporting only one or few modes can be analyzed using a range of methods with high levels of accuracy. As modal volume increases, however, the complexity of modal analysis methods and potential sources of error also rises.

Below, Table 1 provides a summary of nine published methods that can provide information pertaining to the modal volume supported by an optical fiber as well as specific advantages and disadvantages of each technique, including the relevance of each method to the measurement of modal volume reduction as a function of decreasing sapphire fiber diameter.

Table 1: Review of modal analysis methods applicable to optical fiber experimentation

Test method	Description, Purpose, Advantages	Limitations, Disadvantages, Relevance	References
<p>Spatially and Spectrally Resolved Imaging (S^2 imaging)</p>	<p>-Uses a single-mode fiber probe as a scanning spatial filter, which traverses the tip of the fiber in testing to gather local intensity information based on coordinates</p> <p>-Is interferometrically based; spatial and spectral data are collected and the optical spectrum is analyzed (Fourier transform) to distinguish relative power of individual higher-order modes propagating at the region of interest</p> <p>-Highly sensitive (can discern even weak higher-order modes)</p> <p>-Can distinguish between surface scattering and scattering occurring along the length of the fiber</p>	<p>-Limited to large-mode-area fibers (mode area $>100\mu\text{m}^2$, or even $>1000\mu\text{m}^2$) with low modal volume. Sapphire fiber samples demonstrating low modal volume (LMV) have a maximum mode area of $15\text{-}35\mu\text{m}^2$ at the tested wavelengths (assuming maximum core/fiber radius of $\sim 3\mu\text{m}$)</p> <p>-Information is gathered point-by-point using a SMF probe; LMV sapphire samples in question are smaller than typical SMF core ($>8\mu\text{m}$ diameter)</p> <p>-Requires the tip of the fiber to remain stable and secure during analysis since data is highly dependent on location-reduced-diameter sapphire fiber is too small to remain perfectly rigid, and attachment to a platform could alter the guiding properties</p>	<p>55</p>

<p>Wavelength-swept modified S^2 imaging</p>	<ul style="list-style-type: none"> -Uses fundamental concepts of S^2 imaging (data analysis) but sweeps wavelength and images/discerns/transforms the entirety of the observed output rather than physically moving a SMF probe to gain isolated local information -With known fiber length, wavelength, and group velocity of expected modes, the phase shifts between modes can be calculated, allowing for precise knowledge of interference locations (x,y) as well as individual mode power fraction -Not limited to large-mode-area fibers, since the entirety of the near-field pattern is magnified and analyzed rather than requiring a smaller probe to gain local information - Much faster than S^2 imaging since wavelength is swept rather than physical movement of a probe 	<ul style="list-style-type: none"> -Requires magnified near-field images (not far-field) -Expected modes must be known (values for group velocities for accurate deconvolution) -Requires a wavelength-sweeping source and corresponding camera or photodetector sensitive to those wavelengths -Still requires securing the fiber tip for accurate comparison of near-field projections 	<p>56</p>
<p>Near-field/Far-field algorithm</p>	<ul style="list-style-type: none"> -Uses observed near-field and far-field images to experimentally determine mode profiles after deconvolution using an algorithm 	<ul style="list-style-type: none"> -Requires use of a very complicated algorithm that is highly sensitive to non-symmetrical irregularities 	<p>47</p>

	<ul style="list-style-type: none"> -Merely requires near-field and far-field images to acquire mode information -Designed for use with PCF's of very small core radii (in the range of a few microns) 	<ul style="list-style-type: none"> -Ideally uses a wide range of wavelengths (such as a swept source) to increase accuracy 	
Transverse/Wavelength swept S ² imaging	<ul style="list-style-type: none"> -Essentially a combination of the standard S² imaging and wavelength-swept S² imaging techniques outlined above 	<ul style="list-style-type: none"> -Has all of the limitations described above for S² imaging and wavelength-swept S² imaging as well as their combined complexities 	57
Phase Mask Selective Mode Excitation	<ul style="list-style-type: none"> -A binary phase mask is inserted between the laser source and fiber to be tested, enabling excitation of specific modes, if they are supported -Additional refinements, such as wavelength scanning, provide enhanced mode stability information -Results in very clear mode intensity profile images 	<ul style="list-style-type: none"> -Not designed for characterization, but rather for practical application of selective mode excitation -Requires complex equipment to execute, and either amplitude information is discarded in the far-field projection or even more equipment and in situ adjustments are required -Conditions would need to be changed individually to excite modes one-by-one 	58,59

Spatial Light-Modulated Selective Mode Excitation	<ul style="list-style-type: none"> -Uses dynamic holographic generation to control input intensity and phase distribution to selectively excite desired modes -Allows for excitation and characterization of specific modes -Alterations can be made to the system (i.e. to change the desired mode to be characterized) without mechanical realignment 	<ul style="list-style-type: none"> - Requires very complicated setup -Mode excitation and analysis must be conducted one-by-one, although this could theoretically be done using software if a LCD mask is used 	44
Launch Condition Verification	<ul style="list-style-type: none"> -Near-field and far-field patterns are observed, then input conditions were varied (launch angle and position) -Bends and twists are introduced into the fiber and projections are again observed -If any of the above do not change the observed near-field and far-field patterns, single-mode guidance is strongly supported 	<ul style="list-style-type: none"> -Only supports observed occurrence of very low-order modes; cannot directly quantify modal volume 	45,46,60,61

<p>Cladding modes stripped launch condition verification</p>	<p>-Similar experimentation conducted as with the previous “launch condition verification”, except index-matching fluid is used to strip cladding modes</p> <p>-Near/far-field is observed to see whether it appears to be similar to known fundamental mode profile</p>	<p>-This method is irrelevant to current sapphire samples since the cladding is the surrounding air</p>	<p>46,60</p>
<p>Spatial interference</p>	<p>-Light from the test fiber is collimated with that from a known SMF; if a stable interference pattern is observed, single-mode behavior is likely</p>	<p>-Qualitatively supports observed single mode behavior; does not quantify modal volume of an LMV fiber</p>	<p>60,61</p>

To reduce the modal volume of air-clad sapphire fiber such that only relatively few modes are present in the visible-near IR wavelength range, the fiber must theoretically be a few microns in diameter or less. To date, no true quantitative method for analyzing the modal volume of a highly multimodal fiber has yet been developed. Several methods exist that can provide more detailed modal information than near-field and far-field analyses alone^{55,56}, and some can even help quantify modal volume if only a few modes are supported^{58,59}. These methods often require complicated setup and rely on human guidance to determine the parameters used in analysis and are therefore prone to error. It would be ideal to find a test method that allows for discernment of all excited modes to yield more accurate modal analysis.

S² imaging⁵⁵ offers an innovative potential solution since it has the ability to discern individual modes of relatively high order from the overwhelming signal of lower-order modes (as well as interference and superpositions of all modes). However, the proposed method would not be possible for small-diameter sapphire fiber samples, as its method of using a SMF fiber probe to scan the test fiber tip and gain local information limits its application to fibers with a much larger mode area (as well as fiber diameter itself). This method is not applicable to modal analysis of LMV air-clad sapphire fibers.

The wavelength-swept modified S² imaging method⁵⁶ is a viable testing option for LMV sapphire fiber samples. This method observes changes in near-field patterns as a function of wavelength (which is swept at fine intervals- the authors who originally proposed this method captured an image every 0.01nm), eliminating the need for a spatially-scanning

SMF probe, which in turn lifts the limitation of use solely in large mode area fibers. Near-field images are magnified and captured in their entirety and changes in spatial intensity are discerned as part of the data processing, which is essentially identical to the Fourier transform method used in the standard S^2 imaging process. The authors tested a PCF with a mode field diameter ($2.8\mu\text{m}$) that is comparable to that of LMV sapphire fiber produced in the research presented later in this document.

Logistically, one concern with using this method for reduced-diameter sapphire fiber analysis is securing the sapphire fiber tip without causing distortion of the data; air-clad LMV sapphire fiber is so small (only a few microns or less in diameter) that it can be deflected by small disturbances in the air around it; the tested fiber would need to be secured near its tip to ensure the mode fields can be aligned for analysis. However, as the fiber is unclad and furthermore is of reduced diameter with more power theoretically transmittable in the evanescent field, any method used to secure the fiber near its tip would likely cause changes in the observed output.

Additionally, obtaining near-field projections instead of far-field could be difficult since the mode-field properties of small LMV sapphire fibers yield an estimated Rayleigh length (the transition point between near-field and far-field projections) in the tens to hundreds of microns, so the magnifying objective lens would need to be placed within this distance to the tip of the fiber. There are also equipment limitations, as the only wavelength-sweeping source available in the laboratory at the time of this research is in the 1520-1570nm range but there is not a corresponding CCD camera or beam profiler at that range. If these difficulties could be overcome, this method may provide useful information, though the

literature proposing the technique does not fully explain the scope, limitations, or depth of this method, so it may be that it is not sufficiently precise to enable accurate modal volume analysis.

The near-field/far field algorithm method⁴⁷ is theoretically sufficient for testing of small sapphire fibers assuming near-field measurements can be accurately obtained, but it is very complicated and requires additional equipment (wavelength-swept source and corresponding beam profiler, just to name a few) to increase accuracy. Additionally, it is very sensitive to any irregularities; the author mentions that step-index fibers would require uniformity of refractive index in the core to 1 part in 10^5 . While the sapphire LMV production process described later in this document has demonstrated surprising cleanliness and repeatability, it may not be within the extraordinary tolerances needed for accurate measurement using this method.

The various selective mode excitation methods (most prominent being spatial light-modulated selective mode excitation⁵⁸ and phase mask selective excitation⁵⁹) have the potential to allow for individual counting of modes as long as the specific mode field patterns present are known. Section 2.1.2 contains a method for calculating the mode indices of all supported modes, so the mode field patterns can in fact be anticipated and used for these methods. However, these selective mode excitation methods still require modes to be analyzed one-by-one, which is not practical if any more than a few dozen modes are supported. Additionally, detector sensitivity becomes an issue, as many higher-order modes may be supported and present in the intensity profile but have intensities that are too low to be reliably discerned, therefore causing potential inaccuracies in

experimental measurements of modal volume. These methods also seem to assume stable mode propagation along the entire length of the fiber once a mode is selectively excited (i.e. light does not leak from the mask-induced mode to excite other modes during its propagation), but evidence from experiments described in Section 4.3.4 suggest this may not be a valid assumption at all fiber lengths.

The analysis methods described above appear to be designed either for in-depth exploratory analysis of individual mode profiles or for alteration of transmission behavior for operational use (i.e. to excite certain modes to reduce modal dispersion or have properties favorable to the application at hand), and are not particularly intended to discern the number of modes supported by an optical fiber.

The most practical methods for measurement of modal volume are qualitative in nature, though verification through application of several of these methods can provide strong support for observed modal behavior.

Direct observance of the far-field (or near-field) patterns^{46,60} provide relevant information regarding the actual intensity profile of light at given input, waveguide, and environmental conditions. Greater depth of information can be extracted from these profiles using equipment such as a camera beam profiler, as various properties of the beam can be calculated in addition to accurately capturing the intensity profile itself. Therefore, methods based on the analysis of far-field projections may provide the most practical information for analysis of LMV sapphire fiber since the limitations of these methods are well-known and the obtained data is reliable. A method for analyzing the decreasing modal volume of sapphire optical fiber as a function of diameter that is consistent when modal

volume is high as well as low has been designed over the course of this research and is described in detail in Section 3.2.1.

2.2 Numerical Aperture Measurement

The numerical aperture is an important factor in the theoretical predictions of modal volume presented in Sections 2.1.1 and 2.1.2. The theoretically-calculated numerical aperture does not always agree with the measured *effective* numerical aperture, however. The true refractive index of a material is represented by a real and imaginary part quantifying the phase velocity n and extinction coefficient κ^{62} (Eq. 21).

$$\hat{n} = n + i\kappa \quad \text{Eq. 21}$$

While the theoretical calculations for NA of weakly-guiding waveguides (i.e. those with a very small difference in refractive index between core and cladding) are typically accurate, meaningless values are produced in systems with a large index disparity such as air-clad sapphire. Specifically, an NA of ~ 1.4 is predicted for air-clad sapphire over the visible wavelength range, but NA values greater than 1 are impossible; numerical aperture represents the sine of the maximum vergence angle of accepted light in a waveguide, and the inverse sine of values greater than 1 are mathematically undefined.

As the theoretical equation used to calculate NA (Eq. 1) does not account for attenuation and other factors and therefore produces predictions that are meaningless for air-clad sapphire, measurement of NA for LMV sapphire samples is vital for accurate prediction of optical properties. Theoretical/effective NA disparities are especially common for LMV fibers with a small ($>10\mu\text{m}$) core diameter as well as fibers with a non-circular cross

section (such as the rounded-hexagonal cross section displayed by sapphire optical fiber)^{11,63,64}.

The numerical aperture is defined as the sine of the maximum angle of acceptance for an optical waveguide, or, alternatively, the sine of half the maximum angle of divergence of beam exiting a waveguide that has been overfilled (i.e. all modes have been excited through injection of light via a beam with larger spot size from a medium of higher NA than the waveguide under testing⁶⁵).

There are several methods and standards regarding the measurement of numerical aperture, all with the basic objective of identifying this angle of vergence. Some methods calculate NA by injecting light into the tested waveguide at a range of angles and measuring the transmission intensity exiting the fiber, which will decrease as the injection angle is increased compared with the intensity observed at a direct injection angle of 0°. Once the transmission intensity drops to a certain value, which can vary by standard but is usually set at around half that of the 0° launch angle, the NA may be determined based on the angle of injection at that cutoff intensity¹¹. Other methods follow a similar technique, but vary the NA of the input medium instead of the injection angle⁶⁴. However, these methods assume all transmission reductions are purely the result of input NA when other absorption or surface scattering affects may be significant and also injection-angle dependent.

Differences in fiber length can also affect measured transmission intensities which cannot easily be standardized across samples using these techniques.

Other methods involve overfilling the waveguide with injected light and then measuring the divergence angle of the exiting beam. This is done by either scanning a single-point

photodetector linearly or rotationally across/around the endface of the tested waveguide and compiling the resulting x- or y-direction intensity profile to extrapolate a beam width⁶⁶ or by directly measuring the beam width using a CCD beam profiler at some distance D_1 from the waveguide's endface and repeating the measurement again at another distance D_2 . The known difference D_1-D_2 and corresponding difference in measured beam width at each distance results in a measured angle of divergence from which the effective NA may be calculated⁶⁷; this method is most accurate for measurement of single-mode waveguides demonstrating a Gaussian intensity profile. Both methods define the beam width cutoff at some lower intensity relative to the intensity observed at the center of the beam, such as a 5% (4σ) intensity value. The last method is illustrated in Figure 9.

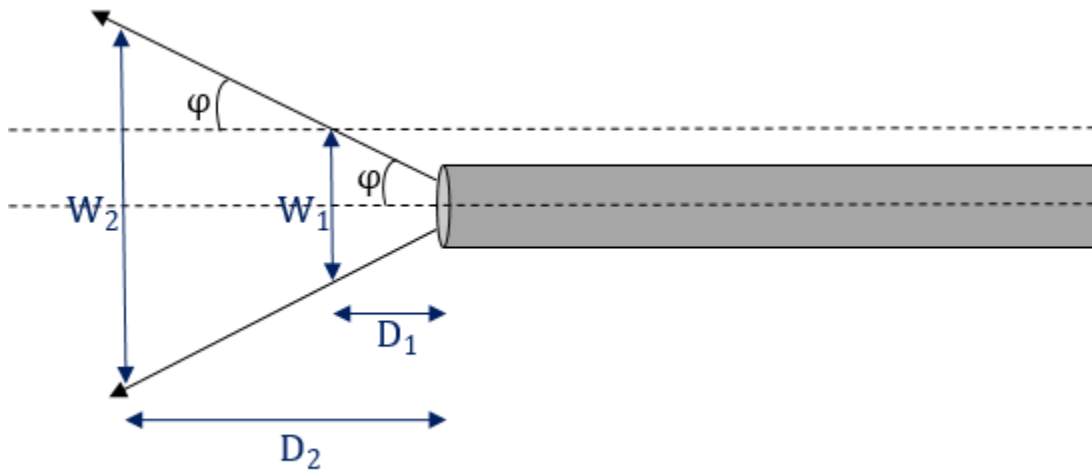


Figure 9: Numerical aperture of an overfilled waveguide can be determined through measurement of output beam widths W_1 and W_2 at distances D_1 and D_2 , yielding a vergence angle ϕ .

Both types of techniques are accepted for NA measurement, but due to the non-circular cross-section and small core size of LMV sapphire fibers, the latter variety was deemed most accurate for this research.

2.3 Core Confinement

In the field of fiber optic communications, strong confinement of power to the core of the optical fiber is preferred to greatly reduce the amount of loss experienced over large distances. In sensing schemes, however, it can be advantageous to increase the interaction between transmitted light and the surrounding medium over short distances to increase detection sensitivity.

When the diameter of an unclad fiber core is near or less than the wavelength of the light it is transmitting, a substantial amount of guided power will exist outside of the fiber itself, allowing some guided light to interact with its surroundings. This *evanescent field* occurs outside of the core of the optical fiber, and is so-called because light typically cannot propagate sustainably and therefore diminishes along the length of the fiber. An evanescent field exists beyond the core of most optical fibers, but the power within it relative to that which is in the core is usually miniscule. With proper construction (such as through the introduction of pores in the cladding⁴³, creating irregular cross-sectional geometries⁶⁸, or reducing the diameter as in a SDF²³), a larger amount of relative power is transmittable outside the core and is guided; this property can be used to create highly sensitive detectors for gas/chemicals, temperature, refractive index, and other applications^{8,14,15,17,20,22-25,68-70}.

A sapphire SDF would have increased sensitivity for evanescent field-based sensing than other designs (such as the D-shaped fiber^{68,71}) because the field exists outside of the fiber core with radial symmetry. Furthermore, a tapered profile will have increased sensing capabilities if it is properly designed^{14,15}.

It is therefore helpful to determine the amount of power that is confined to the core of the fiber (and inversely, the amount of power in the evanescent field). This can be done through a series of derivations resulting in the energy flux density-indicating Poynting vectors (more thoroughly described by Tong, et al³⁸). The Poynting vectors can then be used to calculate the relative power propagating inside and outside the core, resulting in the fraction of core confinement⁵⁴.

2.3.1 Poynting Vector Derivation

We can get a head-start on the derivation of the Poynting vector equations by branching off from the work already completed in Section 2.1.1 of this text, as we will need to calculate the aforementioned propagation constant β for the fundamental mode (the only mode supported by a sapphire SDF). We recall that the number of modes was calculated previously by solving for the intersections of the LHS and RHS of the characteristic equation as plotted vs. X as $X \rightarrow V$ (Eq. 16).

For each solution (i.e. intersection) of the characteristic equation, there is a unique value with respect to X . This solution essentially *is* the propagation constant, and therefore can be extracted by continuing our previous calculations. For example, let's consider the characteristic equation solution for the fundamental mode ($l = 0$) for air-clad sapphire with a radius $a = 200nm$ and transmission wavelength $\lambda = 1500nm$, as plotted in Figure 10.

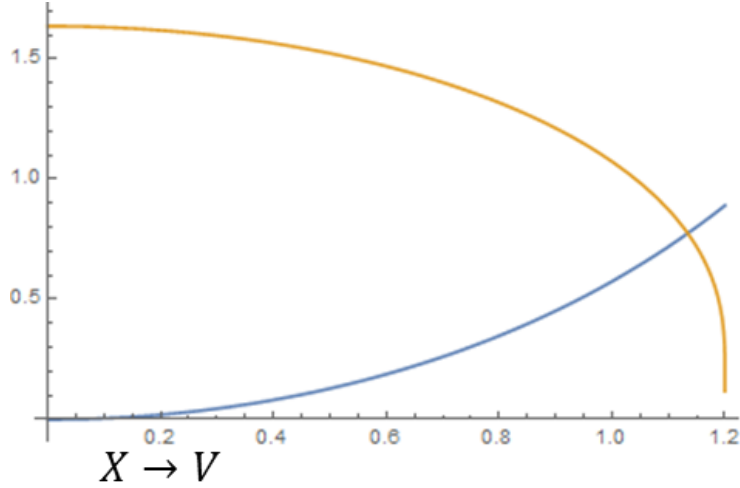


Figure 10: Characteristic equation solution for the fundamental mode for $a = 200nm$ and $\lambda = 1500nm$. Axes are unitless.

The value for the unitless X at the intersection of LHS and RHS is determined to be 1.134 in this case. We can back-calculate the value for k_T , and subsequently β , using Eq. 22 which is essentially Eq. 4 solved for β .

$$\beta = \sqrt{(n_1^2 * k^2 - k_T^2)} \quad \text{Eq. 22}$$

This results in a unitless β -value of 0.004625 in context of our example for the fundamental mode of propagation; since the SDF only supports one mode, this is the only propagation constant we will be required to calculate to discern core confinement fraction.

Next, we derive the Poynting vectors. Eq. 23 through Eq. 28 are listed here as reported by Tong, et al⁵⁴. The eigenvalue equation for the fundamental mode as derived from the Helmholtz equation will be

$$\left\{ \frac{J'_v(U)}{UJ_v(U)} + \frac{K'_v(W)}{WK_v(W)} \right\} \left\{ \frac{J'_v(U)}{UJ_v(U)} + \frac{n_2^2 K'_v(W)}{n_1^2 WK_v(W)} \right\} = \left(\frac{v\beta}{kn_1} \right)^2 \left(\frac{V}{UW} \right)^4 \quad \text{Eq. 23}$$

Where $U = \frac{D(k_0^2 n_1^2 - \beta^2)^{\frac{1}{2}}}{2}$, $W = \frac{D(\beta^2 - k_0^2 n_1^2)^{\frac{1}{2}}}{2}$, and V is as previously described in Eq. 20.

The Poynting vectors are divided into separate equations for core and cladding and describe the magnitude and flux of power in a given direction. These are defined below in Eq. 24 and Eq. 25, where S_{z1} defines the vector within the core ($0 < r < a$) and S_{z2} describes the vector in the cladding ($a < r < \infty$).

$$S_{z1} = \frac{1}{2} \left(\frac{\epsilon_0}{\mu_0} \right)^{\frac{1}{2}} \frac{kn_1^2}{\beta J_1^2(U)} \left[a_1 a_3 J_0^2(UR) + a_2 a_4 J_2^2(UR) + \frac{1 - F_1 F_2}{2} J_0(UR) J_2(UR) \cos(2\phi) \right] \quad \text{Eq. 24}$$

$$S_{z2} = \frac{1}{2} \left(\frac{\epsilon_0}{\mu_0} \right)^{\frac{1}{2}} \frac{kn_1^2}{\beta K_1^2(W)} \frac{U^2}{W^2} \left[a_1 a_5 K_0^2(WR) + a_2 a_6 K_2^2(WR) - \frac{1 - 2\Delta - F_1 F_2}{2} K_0(WR) K_2(WR) \cos(2\phi) \right] \quad \text{Eq. 25}$$

The following relations are assumed:

$$\begin{aligned} a_1 &= \frac{F_2 - 1}{2}; \quad a_3 = \frac{F_1 - 1}{2}, \quad a_5 = \frac{F_1 - 1 + 2\Delta}{2}, \quad a_2 = \frac{F_2 + 1}{2}, \quad a_4 = \frac{F_1 + 1}{2}, \quad a_6 = \frac{F_1 + 1 - 2\Delta}{2}, \\ F_1 &= \left(\frac{UW}{V} \right)^2 [b_1 + (1 - 2\Delta)b_2], \quad F_2 = \left(\frac{V}{UW} \right)^2 \frac{1}{b_1 + b_2}, \\ b_1 &= \frac{1}{2U} \left\{ \frac{J_0(U)}{J_1(U)} - \frac{J_2(U)}{J_1(U)} \right\}, \quad b_2 = -\frac{1}{2W} \left\{ \frac{K_0(W)}{K_1(W)} + \frac{K_2(W)}{K_1(W)} \right\}. \end{aligned} \quad \text{Eq. 26a-j}$$

2.3.2 Core Confinement Calculations

With the Poynting vectors S_{z1} and S_{z2} defined, we can find the fractional power, η , within the core by integrating the Poynting vectors across their respective ranges of r with respect to r and ϕ , and calculating the ratio between power within the core and total power transmitted.

$$\eta = \frac{\int_0^a S_{z1} dA}{\int_0^a S_{z1} dA + \int_a^\infty S_{z2} dA} \quad \text{Eq. 27}$$

Where $dA = a^2 R \cdot dR \cdot d\phi = r \cdot dr \cdot d\phi$.

This ratio can then be used to determine the fraction of power confined to the core.

Conveniently, this ratio can be plotted vs. core radius for a specified transmission wavelength; examples for $\lambda = 520nm$ and $\lambda = 1500nm$ in air-clad sapphire are below in Figure 11.

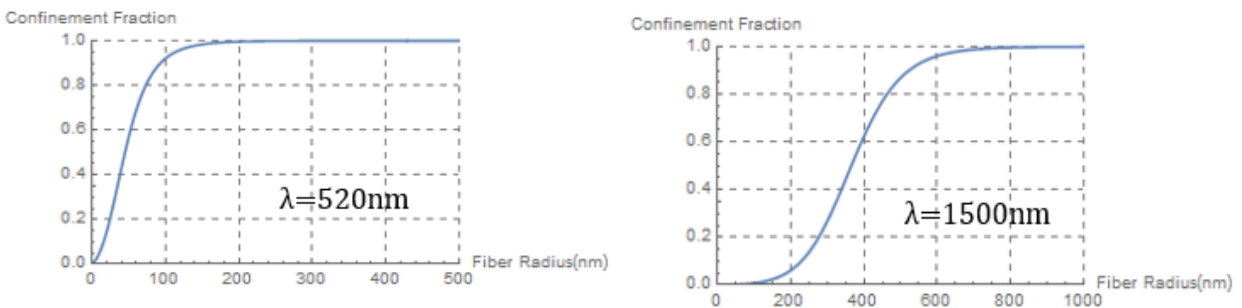


Figure 11: Fraction of power confined to core vs. core radius for $\lambda = 520nm$ (left) and $\lambda = 1500nm$ (right).

The effect of fiber radius on core confinement fraction is easily seen for a given wavelength using these calculations. Intuitively, longer wavelengths propagate with more power outside the core of a subwavelength fiber compared with shorter wavelengths; for a SCSF in air with a radius of 250nm, nearly all of the power is predicted to be confined to the core at $\lambda = 520nm$, whereas near-total confinement of the fundamental mode does not theoretically occur until the sapphire fiber radius reaches nearly 800nm if the operating wavelength is increased to $\lambda = 1500nm$. Calculation of the expected core confinement allows one to engineer the power of evanescent field sensors by creating a fiber with a specific cross-sectional diameter.

2.4 Wet-Acid Etching Chemistry

The only known method for reliably and consistently reducing the diameter of a single-crystal sapphire optical fiber below the 50-70 μm limit of bulk fabrication techniques is wet-acid etching using a mixture of sulfuric and phosphoric acids at elevated temperature⁷².

2.4.1 Historical Overview: Wet Etching of Sapphire Components

Mixtures of sulfuric and phosphoric acids have been used in the surface preparation of various ceramics for decades⁷³⁻⁷⁹. The most common end-use of acid-etched sapphire historically has been as a substrate for film growth for semiconductors and metals in the development of microelectronics. In these cases, c-plane sapphire substrates (i.e. the 0001 crystallographic axis is perpendicular to length and width of the substrate) are preferred since the sapphire c-plane best accommodates the crystal structure of the films being grown⁷⁵⁻⁷⁹. Wet-acid etching is used to ideally create an atomically smooth surface after mechanical polishing.

While numerous studies have been conducted to better understand the chemistry and effects of the acid-etch process on c-plane (0001) sapphire, some disparities in published findings exist (contradictory findings are acknowledged by recent authors^{73,76,77} versus foundational research^{75,78} without much explanation as to the cause of the disparities), and there seems to be no discussion of the etch rate of the $11\bar{2}0$ (a-plane) orientation, which is the plane perpendicular to the optic axis in a standard c-plane sapphire optical fiber and therefore the surface that is etched to reduce its diameter. The distinction between the orientation of interest for traditional sapphire wafers and sapphire optical fibers, the latter

being of interest in this work, is more clearly illustrated by Figure 12.

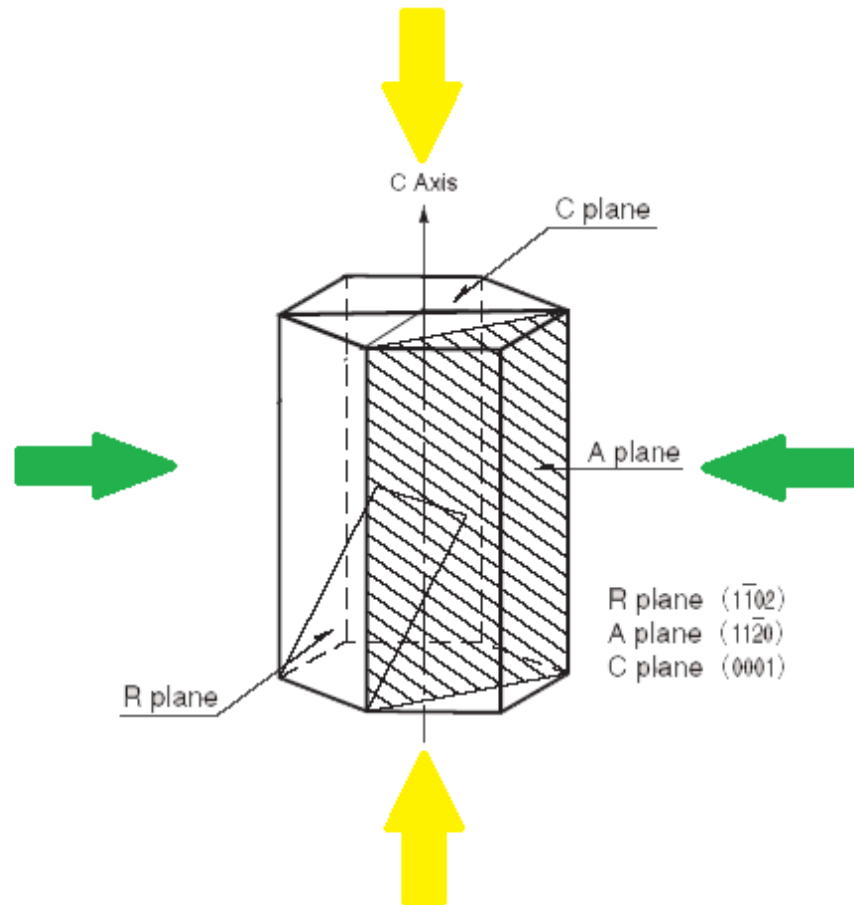
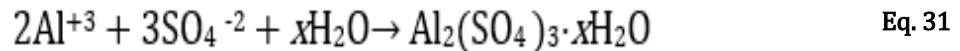
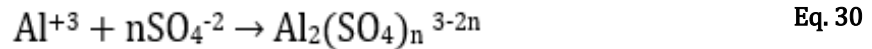
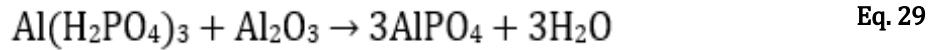


Figure 12: Relevant crystallographic orientations of sapphire. Yellow arrows indicate direction of etching for surface preparation of traditional sapphire wafers; green arrows represent direction of etching for reducing the diameter of a sapphire optical fiber in this research. Adapted from ⁸⁰.

As sapphire is not an isotropic material, one may expect the well-studied etch rate of sapphire's c-plane to differ from the etch rate of the a-plane to some degree. Since the reduction of SCSF diameter through wet-acid etching depends exclusively on the etching behavior of the a-plane orientation, this research benefits greatly from conclusive experimentation determining the chemical effects and behaviors of sulfuric and phosphoric acid mixtures on sapphire's a-plane orientation.

The basic etching reactions for the phosphoric acid portion (Eq. 28 and Eq. 29) and sulfuric acid portion (Eq. 30 and Eq. 31) have been documented as^{76,81-83}:



At the temperatures at which etching occurs (>300°C), however, both sulfuric and phosphoric acids exhibit chemical changes. First, as reported by Dwikusuma⁷⁶, both acids will dehydrate at temperatures greater than 215°C to become diacids.



This transformation may have a significant effect on the etching rate, as acidity is also increased (i. e. $pK_1=1.0$ vs. $pK_2=2.1$ for phosphoric acid; the change is less drastic for sulfuric acid).

Further dehydration of pyrophosphoric acid (the diacid form) can result in the formation of a few different varieties of polyphosphoric or metaphosphoric acid, the basic form being:



Where x is the number of phosphoric units in the molecule.

Continued dehydration will finally yield anhydrous phosphorus pentoxide, with the transformation direct from the diacid occurring as⁸⁴:



Eq. 35

The presence of sulfuric acid has been proposed to inhibit transformation of diphosphoric acid to polyphosphoric acid⁷⁵. However, this behavior has not yet been conclusively proven.

2.4.2 Etch Deposits

While using the 3:1 acid mixture to prepare PVD substrates, many researchers have noted the propensity of insoluble etch products to form and re-deposit on the sapphire surface^{81,82,85}. These etch deposits are insoluble in the etching solution and therefore halt etching progress, forming an intermittent mask that degrades the optical quality of the sapphire fiber. If the deposits are allowed to remain adhered to the fiber they will cause surface scattering of any propagating light. If they are removed either mechanically or chemically the fiber surface itself will be rendered uneven due to the masking effect of the deposits as etching continues after deposition, causing similar scattering issues. The propensity of this issue prevented use of this wet-acid etching method in many optical applications until it was remedied throughout the experimental development described in Section 3.1.2.

Initial trials in this work also noted aluminum sulfate deposits on the sapphire fiber surface as shown in Figure 13. Monoclinic in crystal structure, these insoluble aluminum sulfate deposits form distinctive rectangular crystals that inhibit and eventually halt etching at the locations to which they are adhered. Energy dispersive x-ray spectroscopy (EDS) was conducted during scanning electron microscopy (SEM) of a sapphire fiber with these deposits present, visible in Figure 14. The exclusive presence of the constituents of

aluminum sulfate (aluminum, oxygen, and sulfur) combined with the clear rectangular monoclinic crystal morphology strongly support the conclusion that these deposits are indeed aluminum sulfate.

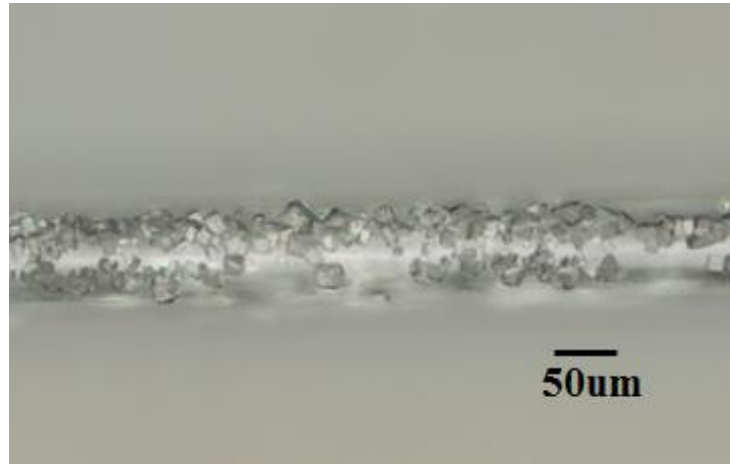


Figure 13: Insoluble etch products formed on the surface of a sapphire fiber in the location of the air-acid interface.

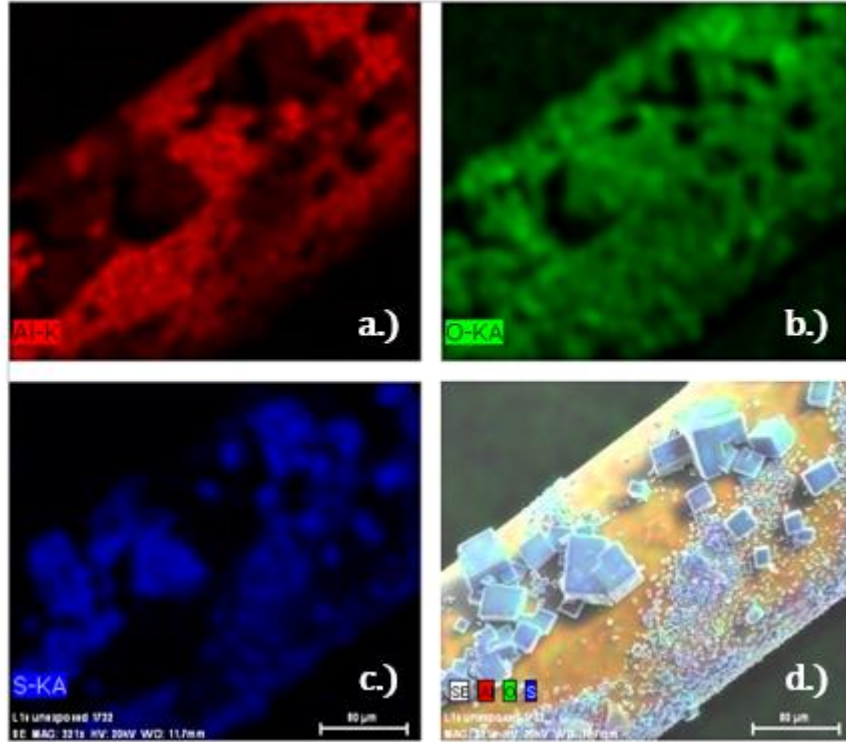


Figure 14: Energy-Dispersive X-ray Spectroscopy (EDS) confirms the exclusive presence of a.) aluminum, b.) oxygen, and c.) sulfur in the crystalline deposits formed during etching. Composite image layered upon SEM image in d.).

3 EXPERIMENTAL PROCEDURES

A reliable, tailorable, and scalable production method has been developed, ultimately culminating in the first reported sapphire SDF⁷². The following pages contain a full description of the procedural development for sapphire fiber diameter reduction and subsequent analyses. The refinements and improvements made throughout testing were instrumental in successful fabrication of testable devices, and in-depth analysis of the etch process chemistry lends greater understanding to the etching process itself.

3.1 Sapphire Optical Fiber Etching Procedure

3.1.1 Etch Equipment Evolution

Feasibility studies were carried out by simply heating the etch solution in a covered glass beaker on commercially-procured hotplates. However, these commercial hotplates showed great variability in temperature control and surface temperature as well as the inability to reach the desired temperatures for efficient etching. Additionally, several ceramic hotplate surfaces cracked after incidental exposure to small acid drips; it would have been unsustainable to continue to replace these expensive items. Finally, with a unidirectional heat profile requiring a flat surface (such as a beaker bottom), the scope of the work was limited and data was inconsistent.

In response to these issues, custom heating equipment was produced. In addition to providing increased versatility, temperature control, and durability, the cost of producing dozens of these custom hotplates was less than the cost of one single commercial hotplate.

Easily-machinable refractory brick formed the base; resistive heating wire was woven throughout as needed for each specific application, and small amounts of ceramic paste and

alumina fiber insulation were used to secure the fiber and ensure even heat distribution. A Variac variable voltage transformer was connected to the resistive heating wire to allow precise temperature control (as monitored by a standard glass-shielded type-K thermocouple immersed in the solution).

Several different types of custom hotplate were created. First, a hotplate supporting standard in-beaker experiments was made, as detailed in the following images.

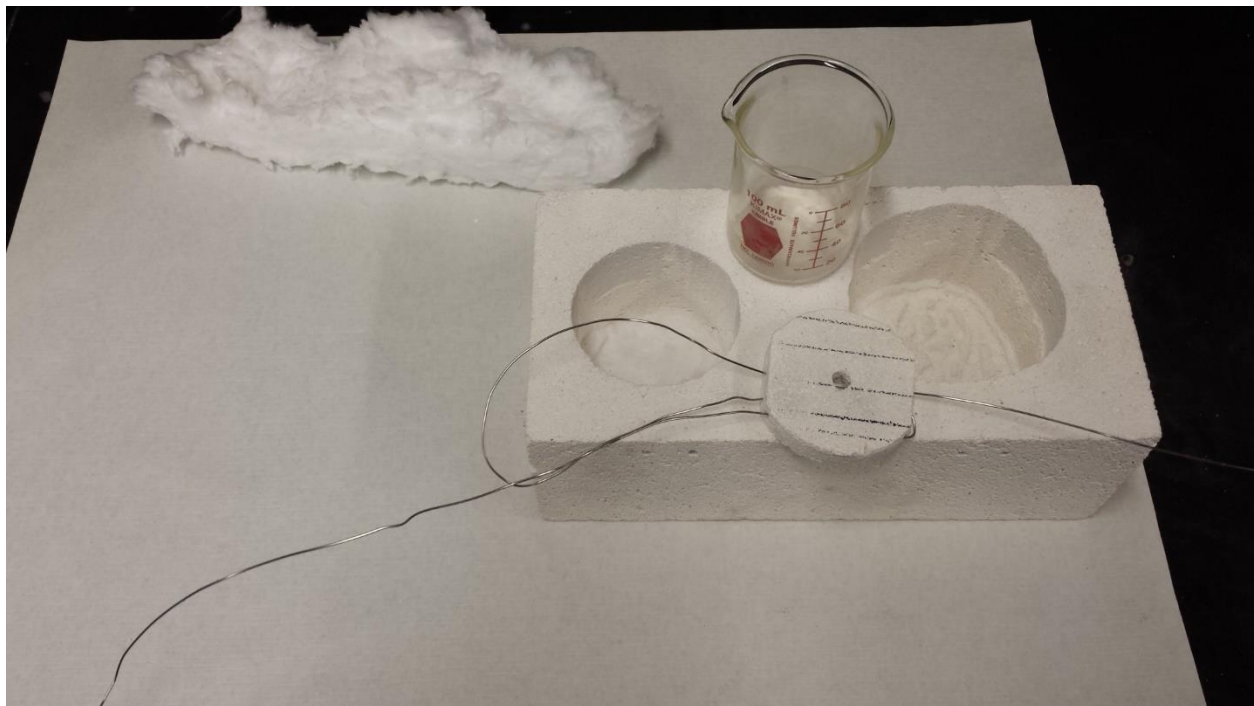


Figure 15: Refractory brick is hollowed out to support a beaker.



Figure 16: Resistive heating wire is wound through the bottom plate.



Figure 17: The heating plate is inserted with wire coiling to exit.

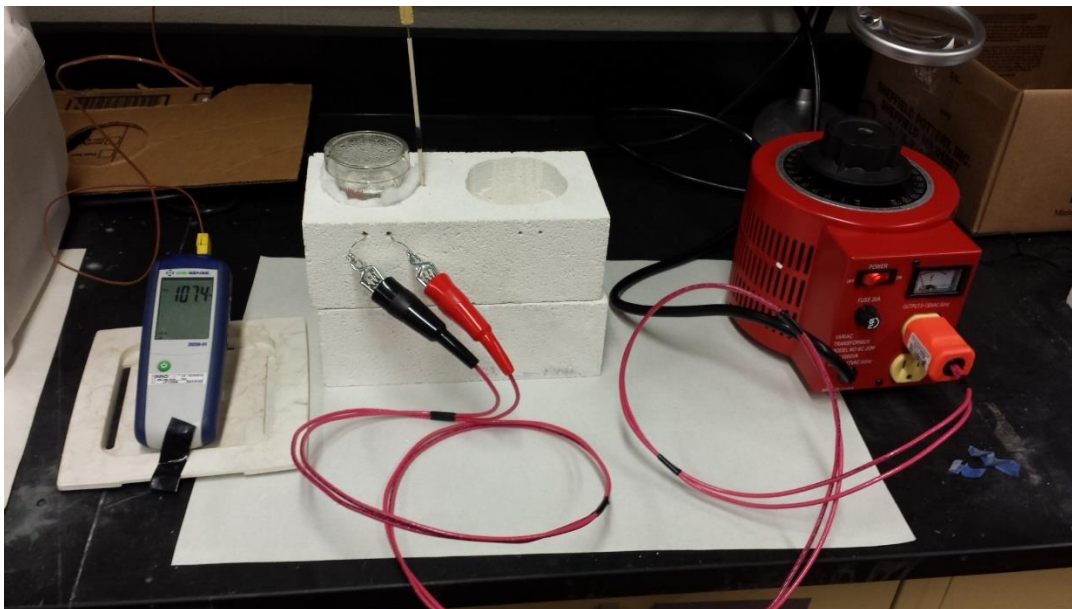


Figure 18: Completed setup as it boils water in an initial test.

These hotplates would heat quickly, consistently, and efficiently. Many initial experiments were carried out using about 60mL of the 3:1 acid solution in a 100mL beaker; using only 17 volts, the solution was fully heated to boiling ($>340^{\circ}\text{C}$) in less than 30 minutes.

Other custom systems were also created for a variety of purposes. In Figure 19, a U-shaped tube formed the primary containment vessel for the purpose of allowing real-time fiber monitoring during etching, as the fiber could be fed through the tube and connected on either side. In Figure 20, a wider hotplate base was created to accommodate a larger vessel such as a relatively high-capacity Erlenmeyer flask.

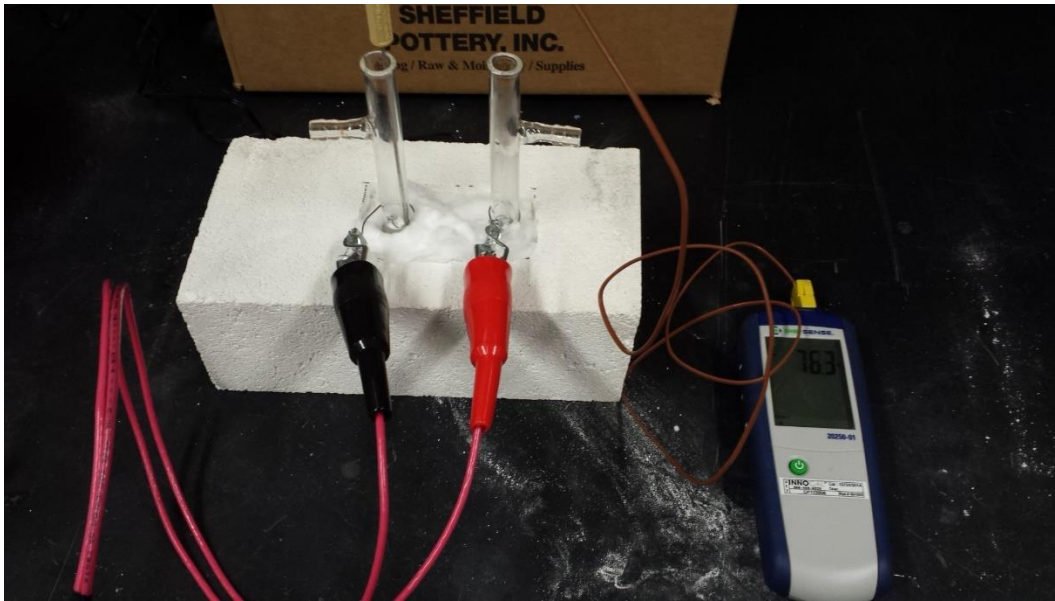


Figure 19: Completed U-shaped setup heating water.

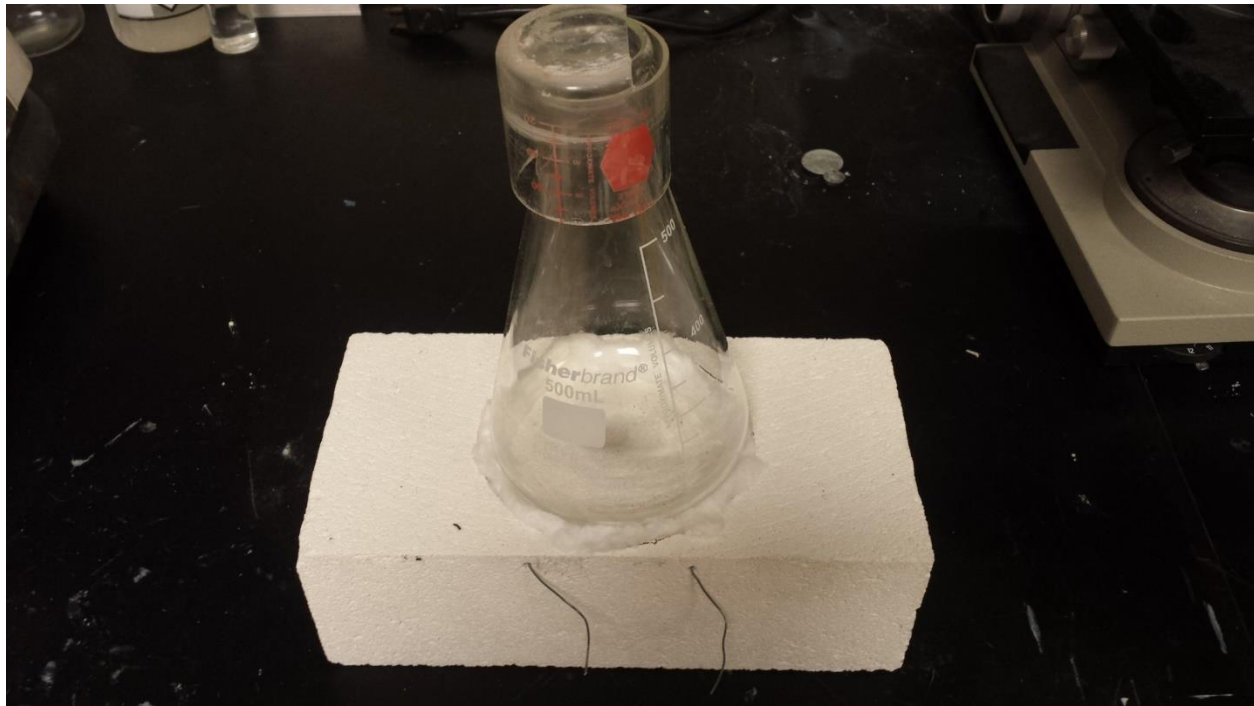


Figure 20: Larger hotplate-style equipment accommodates large Erlenmeyer flask.

Additional systems were created throughout the duration of the research using similar components and techniques, tailored to the desired processing outcome.

3.1.2 Method for Producing Low-Modal Volume Sapphire Optical Fiber

Custom etching equipment was built to accommodate the analytical needs of produced LMV sapphire optical fiber. Some potential sources for difficulty were anticipated and designed accordingly, while others initiated adaptation as issues were identified.

The most efficient manner of measuring modal volume as a function of diameter was determined to be to attach the sapphire fiber to an optical connector before etching, allowing analysis to occur between etching sessions as fiber diameter was reduced. However, this required protection of the connector, which was most practically achieved by ensuring the connector was out and away from the etching solution.

This setup also most closely replicated the practical deployment of a reduced mode sapphire optical fiber in its intended high-temperature and corrosive environments; in practice, the reduced mode sapphire fiber would need to extend beyond the extreme environment so that it could be connected to silica fiber or directly to signal production and interpretation equipment. Therefore, analyzing the modal volume of a sapphire fiber that was connected at its original diameter and was etched further along its length demonstrated a reasonable end-use application design.

Since the inclusion of a connector requires the fiber to exit the etching solution, shielding along the fiber in the region of the air-acid interface was also necessary to prevent adhesion of signal-robbing deposits during etching (Figure 21), the effect of which becomes very obvious during testing (Figure 22).

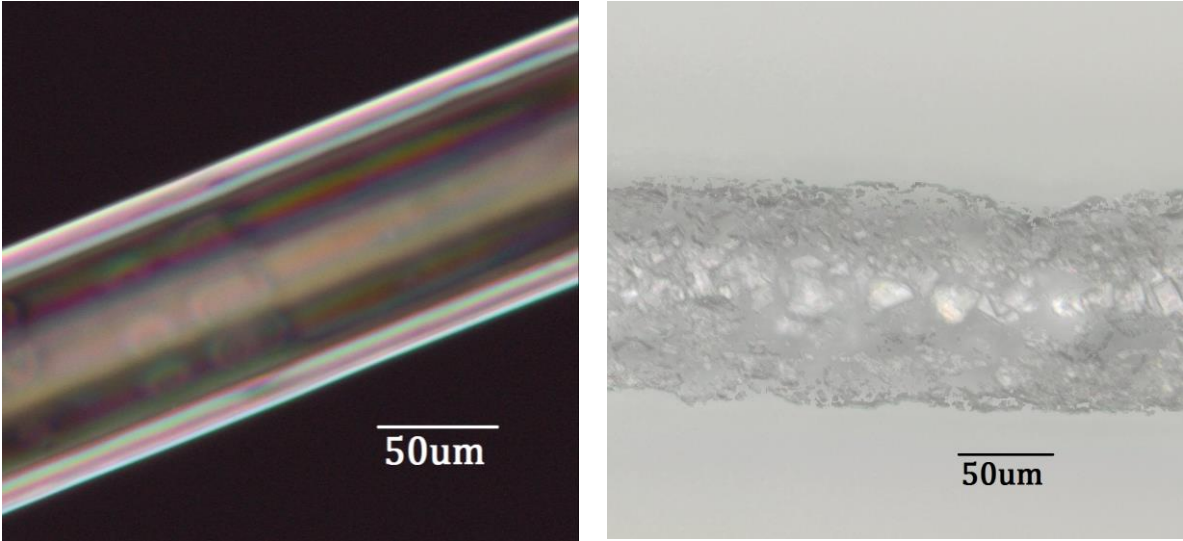


Figure 21: Prolific deposits adhered to the sapphire fiber at the air-acid interface (right) but were absent at segments fully immersed in the etching solution (left).

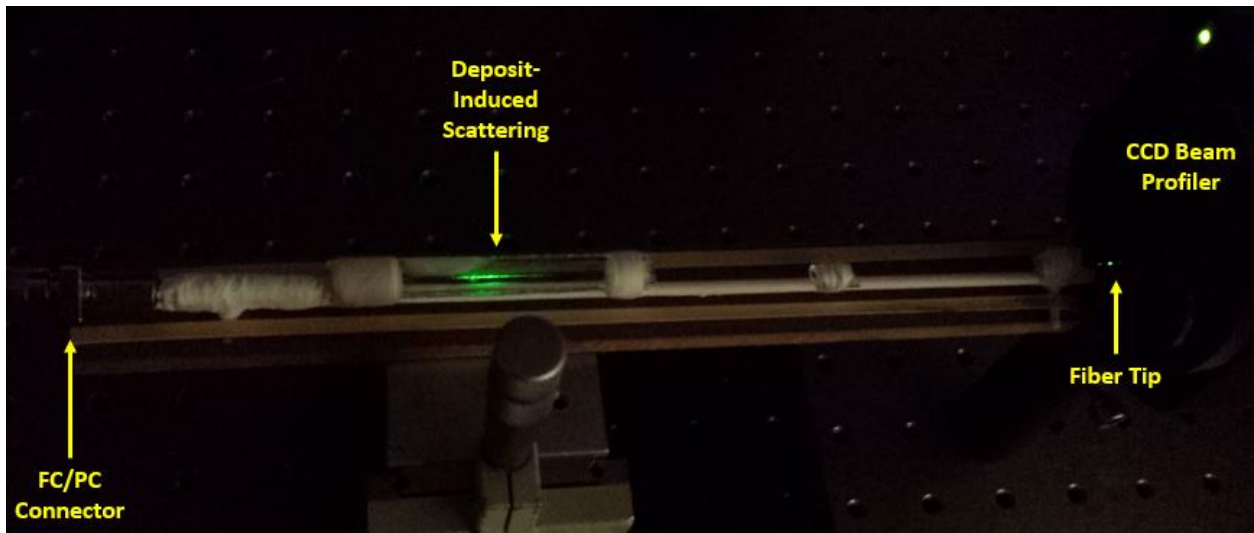


Figure 22: Irremovable deposits accumulating at the air-acid interface during etching caused severe surface scattering during testing using a 532nm green laser.

Ultimately, the best shielding material was deemed to be borosilicate glass, as it has a much slower etch rate in the 3:1 $H_2SO_4:H_3PO_4$ solution than sapphire and its coefficient of thermal expansion is closer to that of sapphire than fused silica (which does not etch at all in this solution). Initial work with fused silica induced catastrophic failure at the sapphire-

silica interface due to CTE mismatch experienced at elevated etching temperatures, with fracture typically occurring around a measured solution temperature of 300°C.

The CTE of fused silica⁸⁶ is on the order of $5 \times 10^{-7}/^{\circ}\text{C}$, while that of sapphire⁸⁷ is $7\text{-}8 \times 10^{-4}/^{\circ}\text{C}$ depending on the crystallographic orientation (as reported around the etching temperature of $\sim 340^{\circ}\text{C}$). The borosilicate glass used in this shielding has a manufacturer-reported⁸⁸ CTE of $3.25 \times 10^{-6}/^{\circ}\text{C}$, which is an order of magnitude closer to sapphire than fused silica; this has proven to be sufficient to reduce the occurrence of CTE-mismatch-induced failure at the temperatures experienced during etching.

Borosilicate tubes with an inner diameter of 150 μm and outer diameter of 3mm were obtained from Vitrocom. Sapphire fibers with a nominal diameter of 125 μm were obtained from Micromaterials and were inserted into the borosilicate tubes by hand to the desired length. It was quickly determined that the difference in sapphire diameter versus borosilicate tube ID, which only measures 25 μm , was sufficient for etch solution to wick into the tube to etch the sapphire fiber and leave signal-robbing deposits (Figure 23), so the tubes then needed to be collapsed onto the sapphire fiber to form a seal and prevent this occurrence.

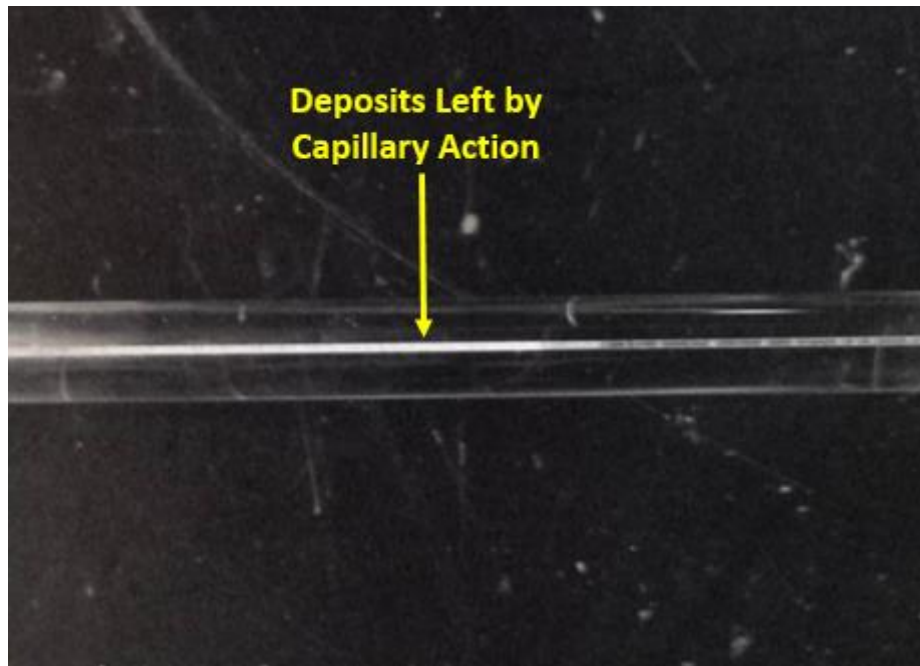


Figure 23: Etch deposits wicked into the borosilicate shielding tube and contaminated the fiber if it was not sealed properly.

A hydrogen-oxygen torch was used to gently heat and collapse the borosilicate tube around the sapphire fiber while rotating on a glass lathe and with the interior under vacuum pressure (Figure 24). As the borosilicate glass can form a cladding of sorts that could potentially skew modal analysis results and any issues regarding CTE mismatch also needed to be minimized, only the few millimeters of length required to seal and protect the fiber was collapsed, leaving the remainder that extended up to the connector open. Hydrofluoric acid was then used to remove the shielding tube below the seal to expose the 10cm length of sapphire fiber to be etched, with approximately 15cm of fiber enclosed in the protective borosilicate glass tube and attached to a 140 μ m ID FC/PC optical fiber connector.

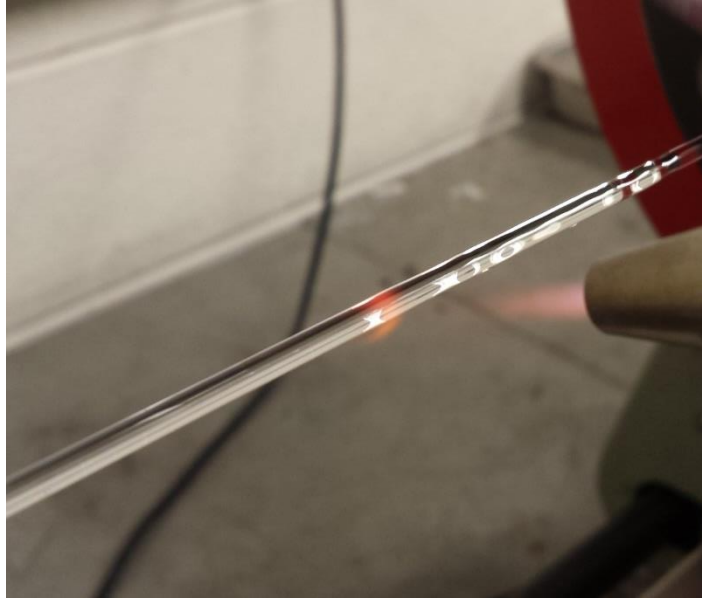


Figure 24: A hydrogen-oxygen torch on a rotating glass lathe was used to gently collapse the borosilicate tube around sapphire optical fiber to form a protective seal.

Once the fiber was protected with its glass capillary tube a 140 μm ID FC/PC connector was permanently attached to one end using epoxy. Connectors with a ferrule diameter of 140 μm were selected over the 127 μm connectors typically used for 125 μm diameter fiber due to the slight but prolific diameter inconsistencies discovered in the commercially-obtained sapphire fiber with nominal diameter of 125 μm ; frequently, 127 μm connectors simply would not fit over the 125 μm sapphire fiber. Since the fiber was easily centered in the ferrule (a natural effect of the serendipitous matching of the borosilicate tube OD and connector coupler ID), using a connector with a 140 μm ID ferrule did not cause any discernible issues. After insertion, the connector was polished to a final diamond grit of 0.1 μm , rendering any polishing scratches optically transparent at the tested wavelengths (Figure 25).

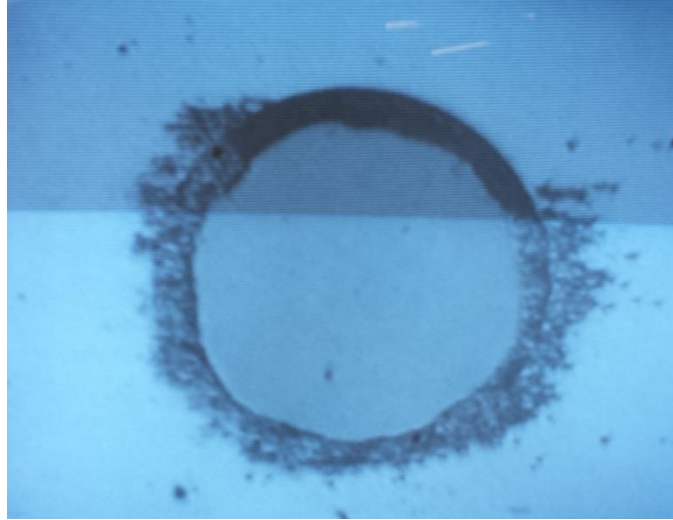


Figure 25: The 125 μm sapphire fiber was easily centered within a 140 μm ID ferrule and then polished to a final lapping film grit of 0.1 μm . The two-tone appearance of the image is an artifact of the CRT monitor.

In order to protect the reduced-diameter sapphire fiber device from accidental breakage during etching, testing, and handling, a separate rounded-triangular-cross-sectioned borosilicate glass tube was used to enclose the device from the base of the connector to near the tip of the etched region, allowing the tip to protrude slightly off the end of the tube. The region of the protective tube covering the sapphire fiber region to be etched was removed on one face using a diamond tile saw to allow free access of etching solution to the fiber as well as enable diameter measurements after etching sessions using optical microscopy. The roughly triangular shape of the protective tube prevented the assembly from rolling around during transport or testing, while the design of the cutout allowed access to the fiber for etching and measurement while still supporting the increasingly flexible fiber. This protective tube is visible in Figure 26 without the sapphire fiber device yet inserted. A short opening was also made near the top of the protector to allow evaporating gas to escape and prevent capillary wicking of the acid solution from reaching base of the connector during etching.

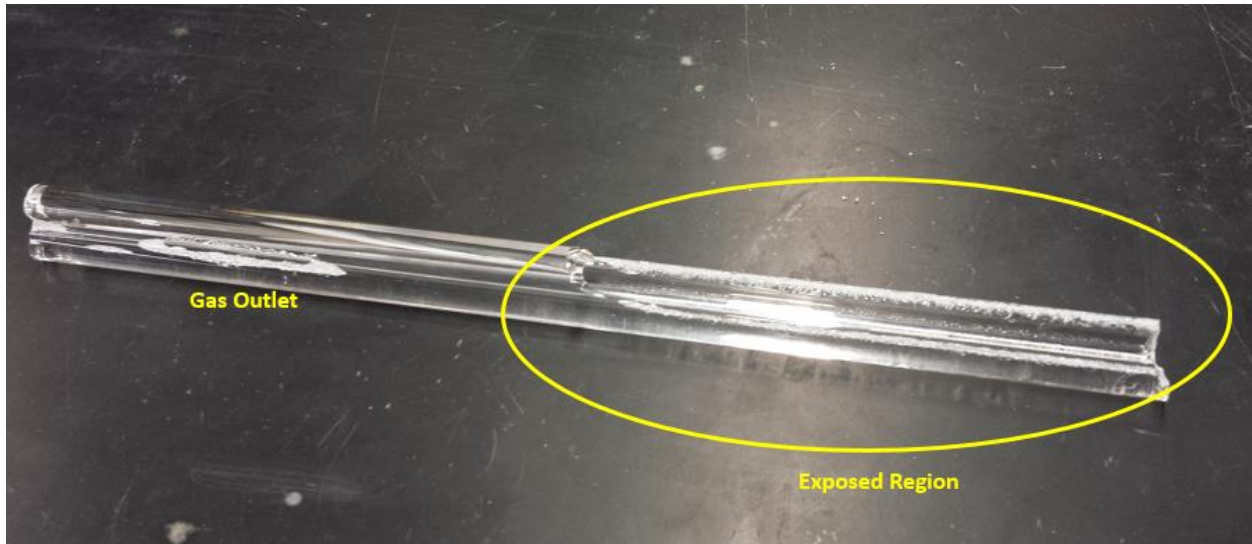


Figure 26: External tube protects the sapphire fiber device from accidental breakage while allowing access to the etching fiber region.

The borosilicate-shielded, FC/PC-connected sapphire fiber was then inserted into the external protective tube, where it remained for the duration of etching and testing (Figure 27).

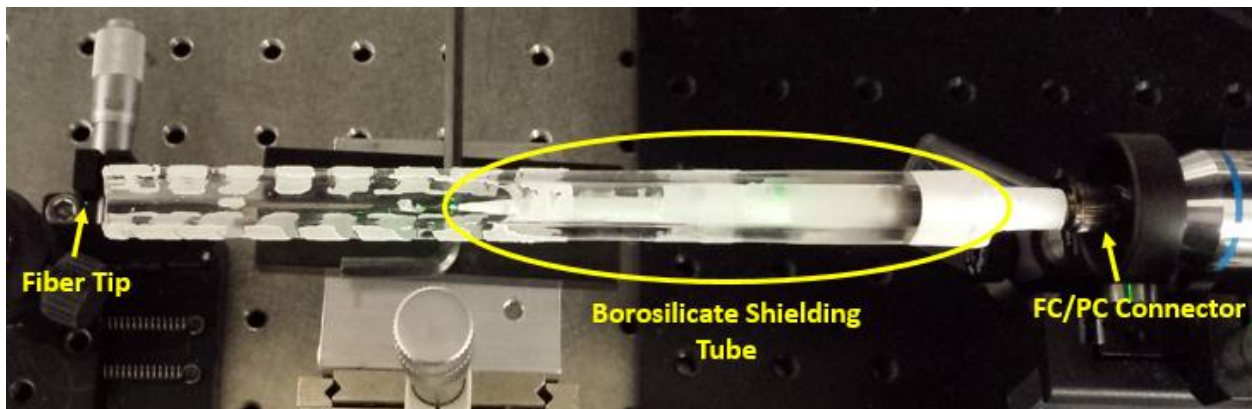


Figure 27: Shielded, protected sapphire fiber during testing after etching.

3.1.3 Etching Equipment for Production of LMV Sapphire Fiber

Next, equipment was constructed to contain and heat the etching solution and reduce the diameter of the LMV sapphire device. From the inside out, the components were constructed as follows:

1. Primary containment vessel

A fused quartz tube with inner diameter of 1.25 inches formed the primary containment vessel. The tube was supplied by Quartz Scientific; the end was collapsed using a hydrogen-oxygen torch and glass lathe (Figure 28).



Figure 28: A fused quartz tube with one end collapsed forms the primary containment vessel.

2. Heating coils

To add thermal mass and increase stability of the heated solution (and corresponding etch rate along the length of the sapphire fiber), porous aluminosilicate rings were fabricated, pictured in Figure 29. Holes were drilled longitudinally in the wall of these rings and resistance heating wire (80% nickel, 20% chromium, 20 gauge) was wound through these holes in the manner illustrated by Figure 30. Securing the resistive heating wire longitudinally rather than winding wire around the outside of the rings in a spiral pattern was found to increase the heating consistency from the top to the bottom of the heating

vessel; otherwise, it would be possible for the etching solution to be slightly hotter near the top of the vessel, causing the fiber to etch more quickly at its base rather than its tip. This would result in the fiber detaching from its shielding region before etching to a diameter sufficient for testing was complete.

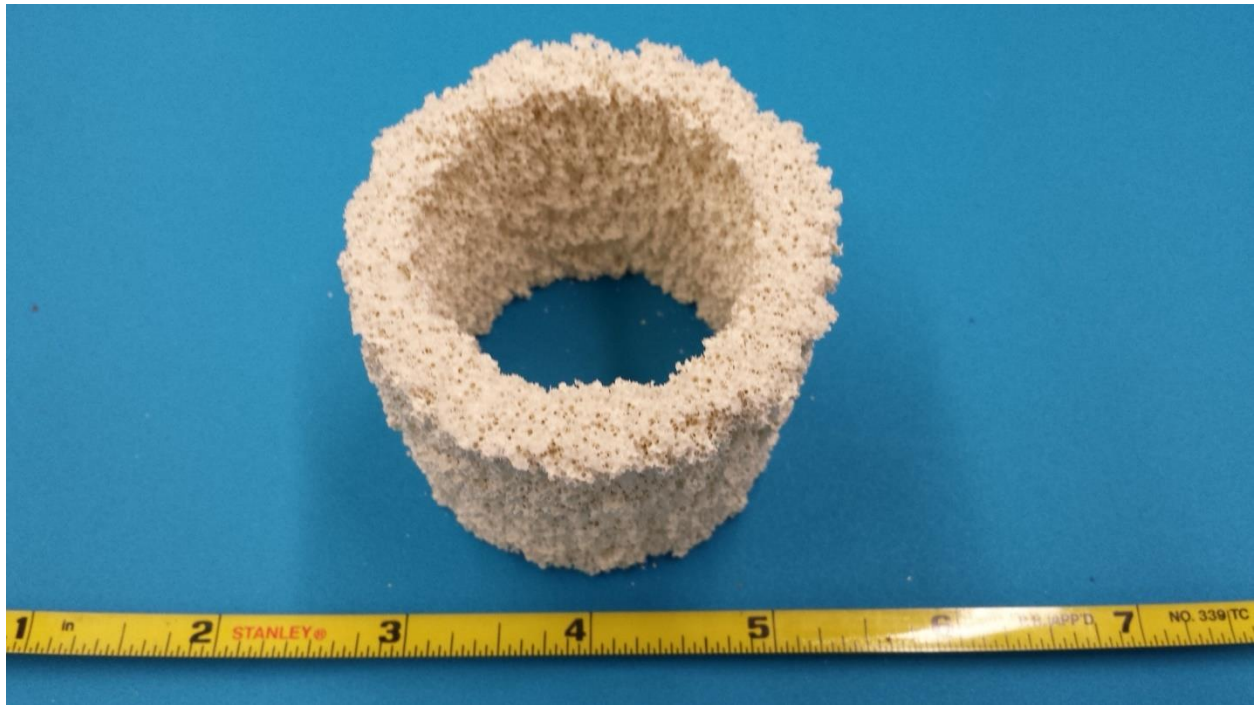


Figure 29: Porous aluminosilicate rings added thermal mass surrounding the quartz tube.

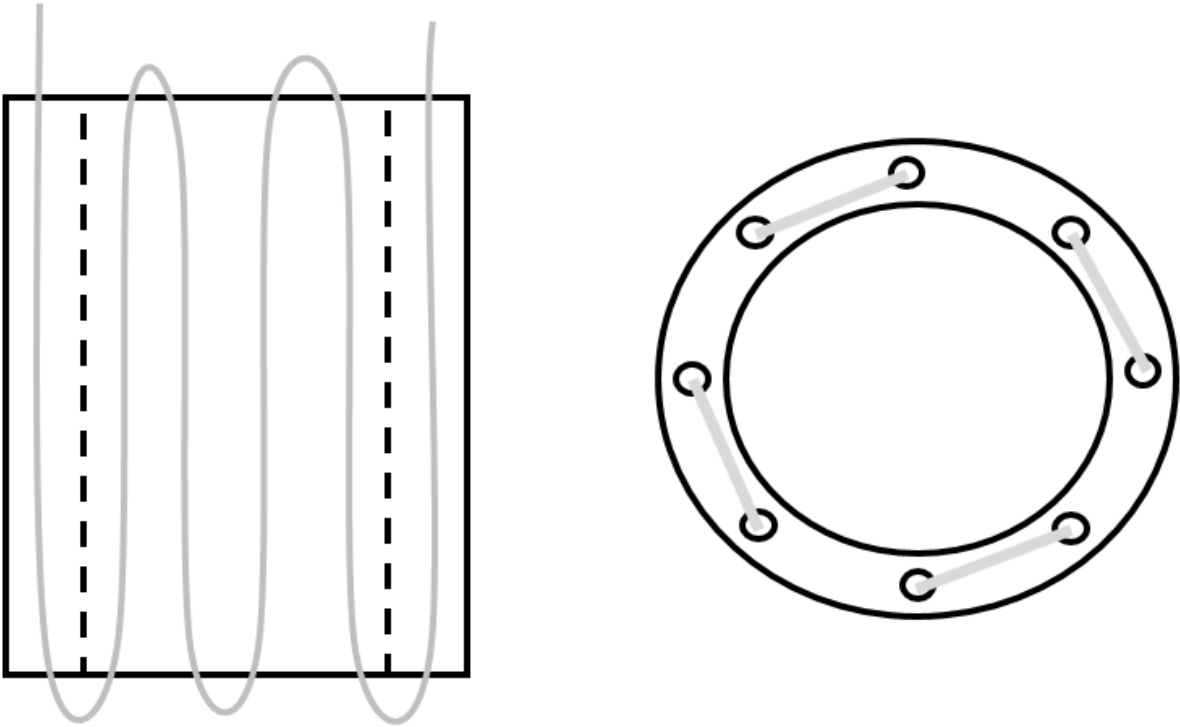


Figure 30: Graphical illustration of the winding of the resistive heating wire (represented in gray) through porous aluminosilicate rings.

3. Insulation

Alumina fiber insulation was then used to enclose the heating rings to preserve generated heat and protect items in contact with the exterior of the system. This was also used to provide increased thermal mass and add mechanical stability to the system as it was fitted inside its enclosure.

4. Enclosure

A section of polycrystalline alumina furnace tube with an inner diameter of 3" was used to finally enclose the etching apparatus. This tube, along with the alumina insulation, provided stability to the interior and allowed the system to be more easily handled and secured. The completed apparatus is pictured in Figure 31.

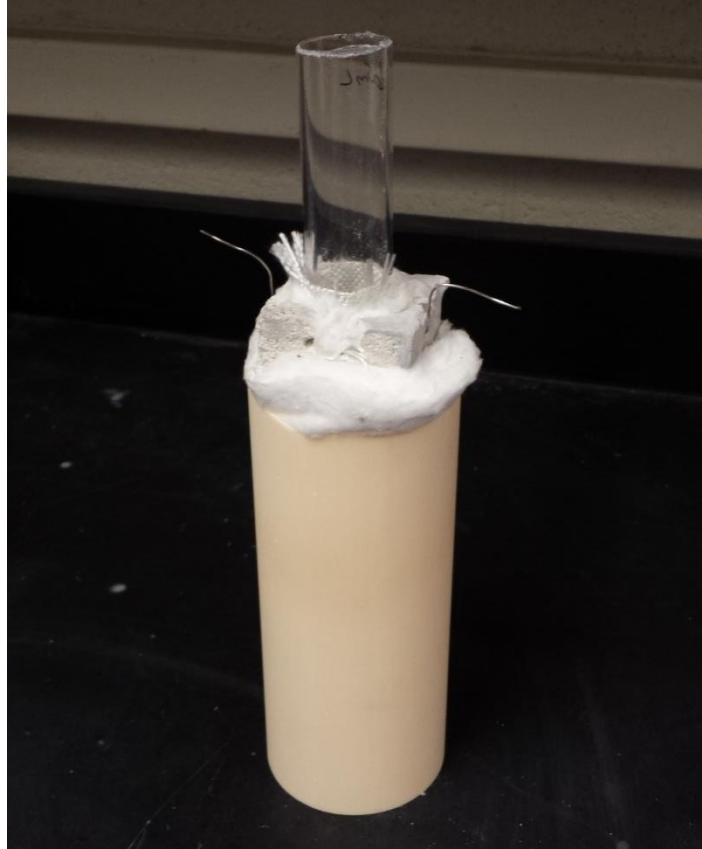


Figure 31: Completed etching apparatus used in production of LMV sapphire samples.

5. Voltage transformer

A Variac voltage transformer (20A, 120V input, 0-130V output) was used to regulate the voltage and corresponding heat generated by the resistance heating wire. Alligator clips attached to wires and a plug were clamped onto the two protruding resistance heating wire ends; as little as 15V was needed to generate and maintain enough heat to bring the etching solution to the boiling point at 343°C.

6. Temperature monitor

As the 3:1 $\text{H}_2\text{SO}_4\text{:H}_3\text{PO}_4$ solution only etches sapphire fiber at a rate of a few microns per hour, many hours were required to reduce the diameter to those at which significant modal volume reduction could be observed. While the etch temperature was limited (and regulated) by the boiling point of the sulfuric acid component, and therefore a consistent

temperature of 343°C could be anticipated, it was helpful to be able to monitor and record the temperature experienced by the etching device throughout the process.

A K-type thermocouple probe was shielded by a closed-end fused quartz tube; the fiber device (such as that pictured previously in Figure 27) was then secured to this tube using Teflon tape, with the fiber tip in close proximity to the thermocouple tip within its glass shielding. The thermocouple was then connected to a Digisense datalogging thermometer (Davis Instruments), which was capable of recording a maximum of 18,000 data points from up to 4 different thermocouples simultaneously. In these experiments, a sampling interval of one measurement per 15 seconds was selected, and the temperature history was recorded throughout every etching session to ensure consistency and identify any temperature-related issues. An example heating profile for a typical etching session is pictured below in Figure 32.

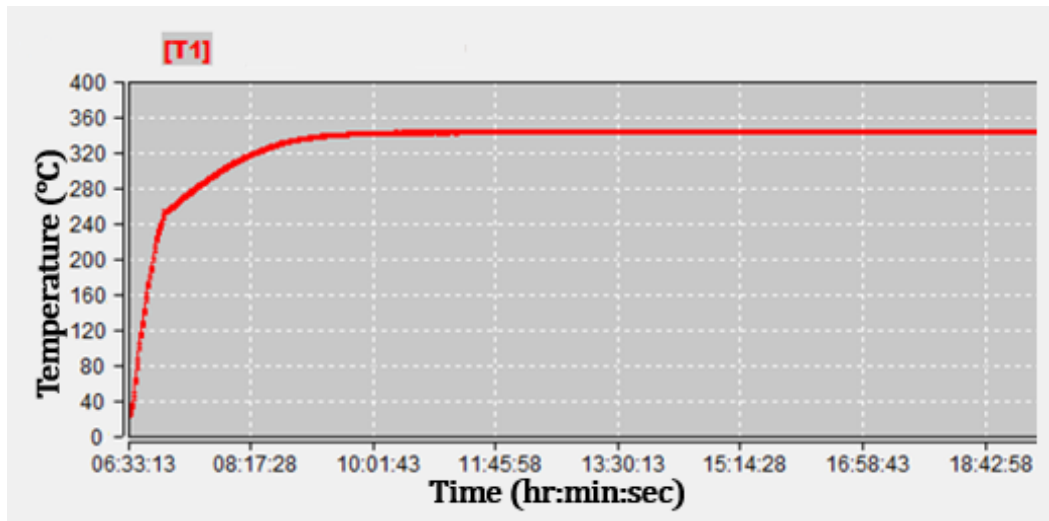


Figure 32: Heating profile of a 16-hour etching session as monitored and recorded by the datalogging thermometer.

After insertion of the device and addition of the 3:1 etching solution, the open end of the quartz tube forming the containment vessel was wrapped with 1.5" wide Teflon tape to

form a near seal around the protruding connector end of the device. A small vent hole was included to prevent pressure buildup and allow for evaporation of water during heating while also forming a condensation surface to retain as much of the evaporating sulfuric acid as possible to extend the maximum duration of etching sessions.

3.1.4 Sample Mounting and Preparation

One easily overlooked aspect of the initial etching experimentation that was the subject of significant early refinement pertains to the manner in which samples were secured within the etching solution. In early etching studies samples were simply placed in the bottom of a borosilicate glass beaker, filled with the 3:1 etching solution, then removed once etching was completed and the solution was cooled. However, this led to several problems, chief (beyond the propensity to literally lose the miniscule fiber) being the issue of deposit formation on the fiber surface that would halt etching or hide the sample and prevent it from being recovered for analysis.

It was discovered early in the experimentation that deposits of a different nature from the aluminum sulfate deposits discussed in Sections 2.4.2 were forming around the sapphire fibers (Figure 33) which would halt etching just as effectively as the aluminum sulfate variety. Fortunately, these deposits could typically be removed with light mechanical pressure (such as rolling the fiber between the fingers), but could not be removed easily by chemical methods; the issue needed to be addressed to prevent problems with the processing of smaller fibers or those with more delicate geometries.

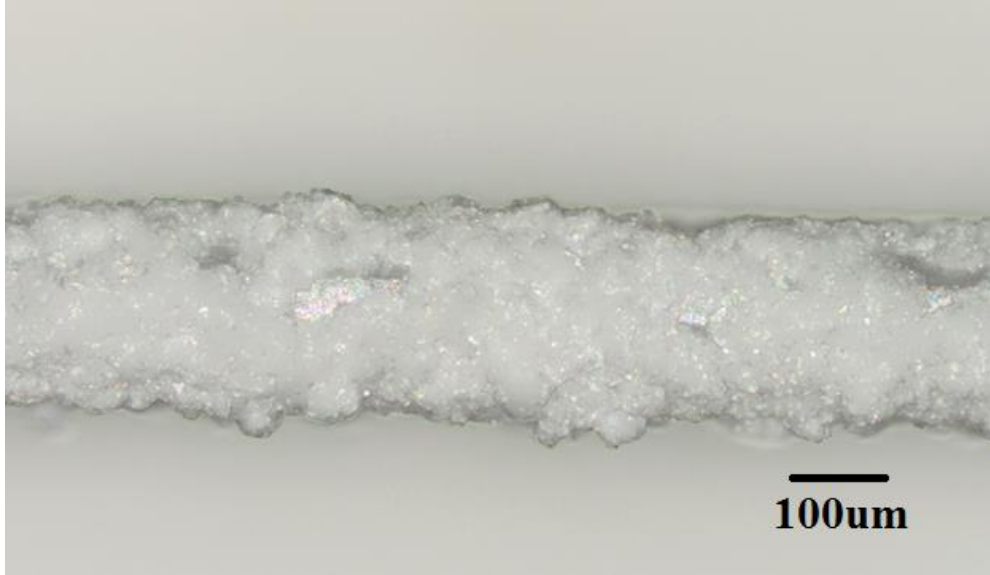


Figure 33: Etch deposits completely covering a sapphire fiber after 6 hours at 310°C.

To determine the source of these deposits, energy-dispersive X-ray spectroscopy was invoked. EDS found high levels of silicon, oxygen, and phosphorous in a sample of the deposits (spectra visible in Figure 34). Aluminum and sulfur were present, but in relatively small amounts, indicating that the deposits were not primarily aluminum sulfate (as was already surmised by the lack of distinctive crystalline structure characteristic of aluminum sulfate).

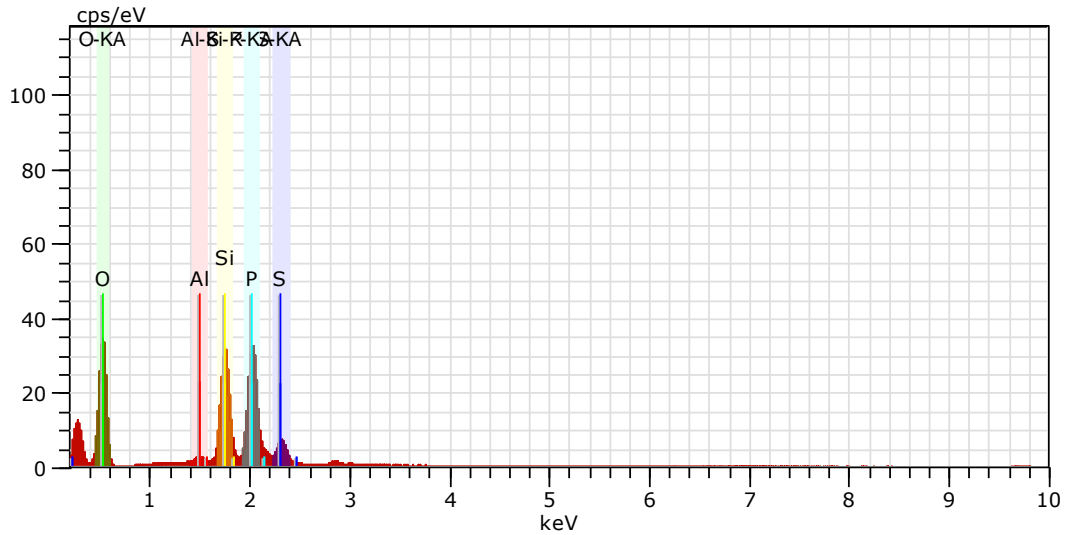


Figure 34: EDS of beaker deposits indicates high silicon, phosphorus, and oxygen content.

These results were curious at first; silica is known to be resistant to etching in the 3:1 solution, as was backed up by experimentation, where a pure fused silica fiber was placed in the same etch solution as a sapphire fiber (both 200 μ m in diameter initially) for 7 hours at 340°C. Upon removal, the diameter of the silica fiber was unchanged, while the sapphire fiber diameter was reduced as anticipated by nearly 30 μ m (Figure 35).

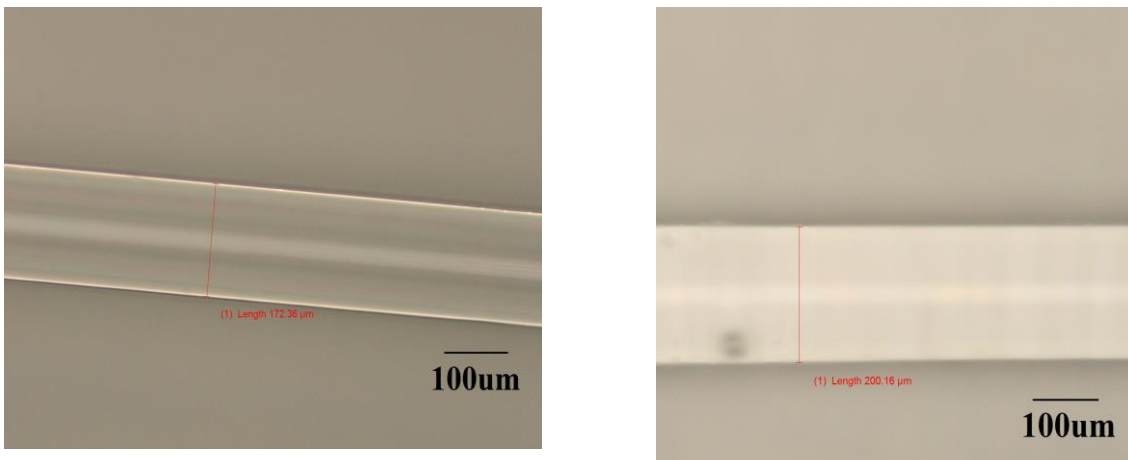


Figure 35: Silica fiber (right) does not etch after 7 hours at 340°C; sapphire etches as expected (left).

While fused silica demonstrated measured resilience to the etching solution, it seemed the borosilicate glass used in standard laboratory beakers were not so invulnerable. Fused silica vessels replaced standard lab-grade borosilicate beakers for the remainder of the experimentation and deposit formation of this type vanished immediately; apparently while fused silica is in fact unetchable using the 3:1 solution, the additives in borosilicate glass allowed significant etching to occur. Switching to pure fused silica quickly remedied the problem.

To reduce the likelihood of losing a sample as well as to keep the sample off the bottom of the beaker (where etch deposits were likely to settle), fibers were mounted to glass substrates using PTFE (Teflon) tape. While the stated maximum service temperature of polytetrafluoroethylene is only 260°C, it was found to perform remarkably well in the etch solution at temperatures beyond 340°C (it would finally begin to break down approaching 400°C in phosphoric acid). Fiber samples were typically mounted to fused silica rods or tubes using PTFE tape to secure the fiber so that it was fully immersed in the etching solution. This also allowed for the creation of custom mounting geometries to suit various needs (such as selectively etching areas of a fiber); examples of early mounting devices are pictured in Figure 36.

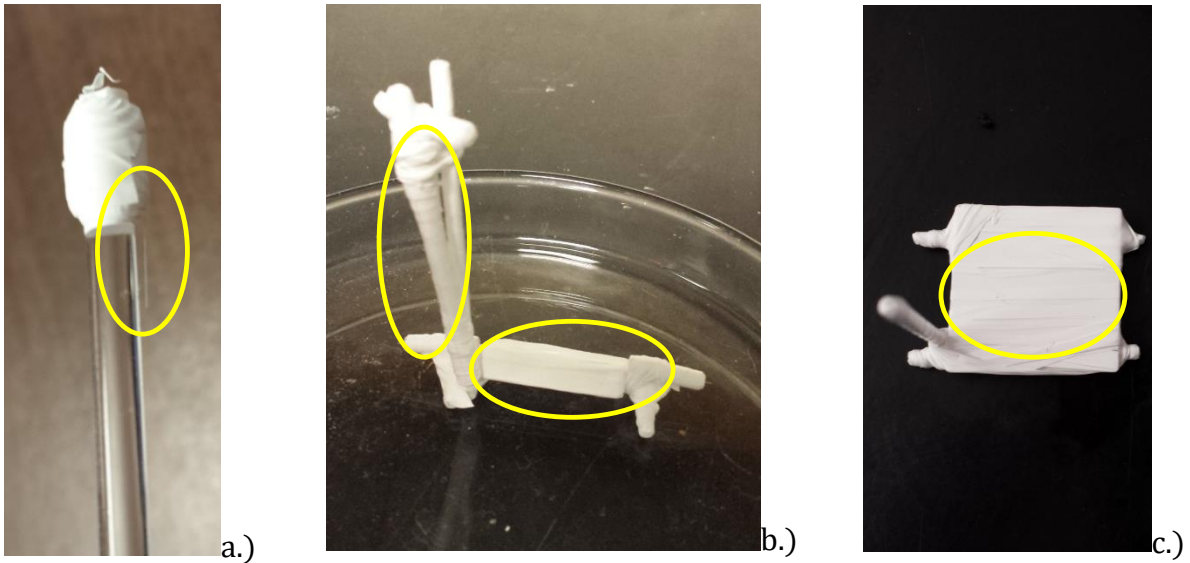


Figure 36: Teflon was used to securely mount fiber samples for initial etching studies. Fiber locations are circled.

3.2 Optical Analysis Methods

3.2.1 Far-Field Projection Modal Volume Measurement Method

Far-field projections represent the radial intensity distribution of light travelling through an optical fiber. Without any added system modifications, these intensity profiles are composed of the combined interactions, interferences, and superpositions of all supported modes that have been excited by the light source (the specific modes that have been excited among all that are theoretically supported by the fiber are affected by input conditions such as wavelength and insertion angle)⁴⁷. Far-field patterns can be observed by simply placing an object such as a piece of paper some distance away from the fiber tip for visual observation but are more conveniently captured and analyzed using a CCD camera designed for this purpose.

Not all of the supported modes will be excited by a single wavelength source, and therefore corresponding far-field patterns cannot provide the entirety of the modal information

relevant to the fiber. Nevertheless, observance of the far-field profile does represent accurate information about the manner in which light is propagating at those specific conditions (i.e. wavelength, injection angle, and the physical state of the fiber such as bends, claddings, or surface deposits). The characteristics of the individual modes present in a far-field projection cannot be deconvoluted in a single measurement, but that single measurement captures an accurate representation of the overall radial intensity pattern present within the fiber in the current conditions, which is of great practical relevance and importance.

One method of qualitatively observing modal volume reduction as a function of decreasing diameter within a sapphire optical fiber was developed during this research using only a CCD camera beam profiler, an objective lens, and lasers of three different wavelengths. Far-field intensity patterns were observed for the three laser wavelengths and changes in the properties of the far-field intensity patterns were observed and compared to provide qualitative modal volume reduction information.

The far-field projections of highly multimodal fibers represent the interference and superposition of many modes, resulting in a radial intensity pattern with a speckled appearance; this speckle pattern is the projected radial intensity pattern of all propagating modes at the given input and fiber conditions.

Qualitatively, the overall concentration of intensity peaks (speckles) was proposed to decrease with decreasing fiber diameter while the relative size of individual intensity peaks increased. This is attributable to decreasing modal volume; the occurrence of these intermittent intensity peaks in a multimode fiber is attributable to the constructive and

destructive interference of modes of the same phase. As modal volume decreases, there are therefore fewer modes present to interfere with one another and cause the speckle patterns visible in far-field projections. Eventually, modal volume could be reduced to a point that such interferences and superpositions would cease and low-order modes with recognizable patterns would become apparent.

Far-field intensity patterns were measured using a Thorlabs BC-106VIS CCD camera beam profiler and BEAM 6.0 software at 5mW laser wavelengths of 532nm, 783nm, and 983nm, which were focused into the sapphire fiber connector end using the objective lens in direct free-space coupling. The objective lens had a listed NA of 0.66; the effective numerical aperture of 300 μ m-diameter sapphire fiber has been measured to be \sim 0.35 at a wavelength of 2.94 μ m¹¹, while the manufacturer of the 125 μ m-diameter sapphire fibers used in this testing claims an approximate effective NA of \sim 0.45 at a wavelength of 633nm⁶⁴; both measurements indicate the effective NA of sapphire at the input diameter of 125 μ m is well below that of the objective lens providing the injected light. Since the focused laser spot size (\sim 500 μ m diameter) was greater than the 125 μ m-diameter sapphire core at the injection endface and the NA of sapphire was lower than the NA of the objective lens, the mode condition of the fiber was considered to be *overfilled*, meaning all supported modes would be excited by the input conditions⁶⁵. In this manner, the observed far-field projections accurately represented the radial intensity profile provided by all modes supported by a particular fiber diameter and input wavelength; this setup is pictured in Figure 37 during testing of a sample.

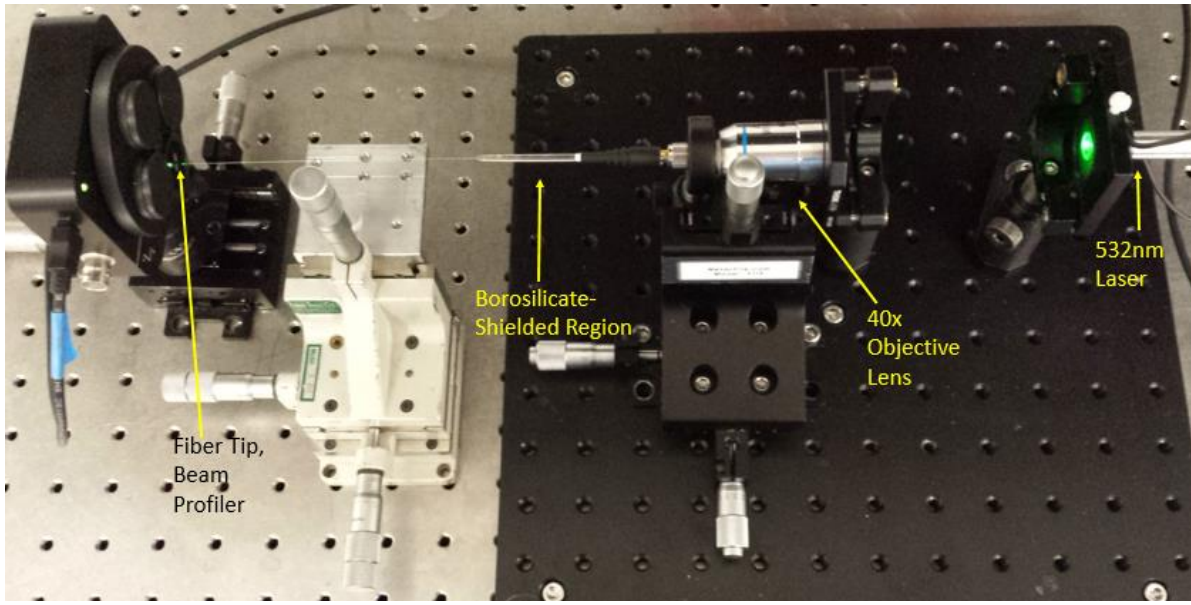


Figure 37: Shielded, connected sapphire optical fiber during testing using a 532nm laser.

The tip of the etched region of the fiber was polished using a final diamond lapping film of 100nm grit after each etching session; this step proved to be a delicate endeavor. While sapphire microfibers are surprisingly resilient to bending, they are rather incapable of holding much weight in tension. As a result, the newly-polished tip of a miniscule sapphire fiber would often be removed along with the phenyl salicylate wax used to secure it during polishing if not executed carefully. Allowing the sapphire microfiber to protrude slightly from the wax rather than being fully embedded seemed to help resolve this issue. A stereoscope was employed to observe polishing (Figure 38) to ensure only the fiber tip was polished and also to prevent the fiber from bending too much during polishing, which would yield a pattern-distorting beveled endface.

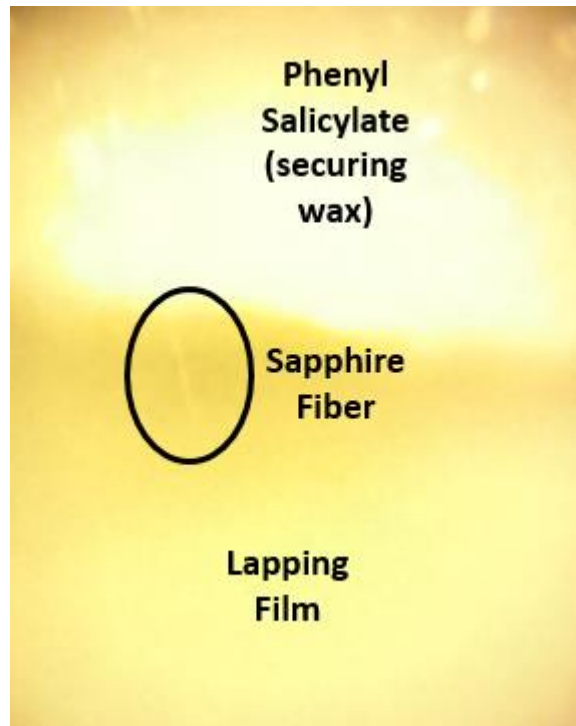


Figure 38: A stereoscope mounted to observe polishing of few-micron-diameter sapphire fiber proved necessary to ensure proper polishing occurred without breaking the miniscule fiber

Polishing after etching was necessary because the r-plane of the sapphire fiber etches more quickly than the c-plane in the 3:1 $\text{H}_2\text{SO}_4:\text{H}_3\text{PO}_4$ solution, causing faceting to occur on the endface of the fiber (Figure 39).

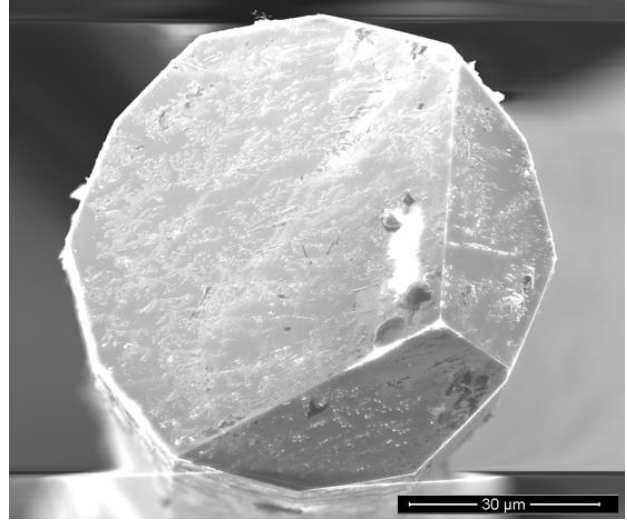
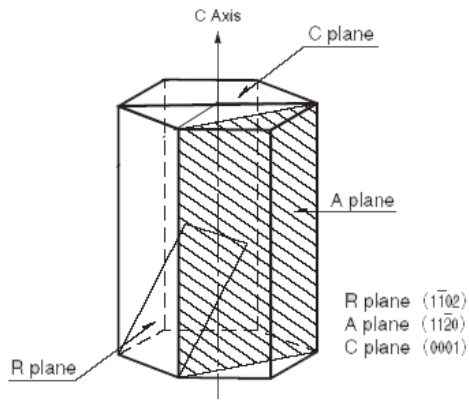


Figure 39. Preferential etching of the r-plane (left) causes faceting on the fiber endface (right), which must be polished to prevent distortion of far-field patterns.

While useful sensing schemes could possibly be designed around the angled tip caused by this faceting, in modal analysis it only causes light to scatter rather than form discernible far-field patterns for modal volume interpretation, as demonstrated by Figure 40.

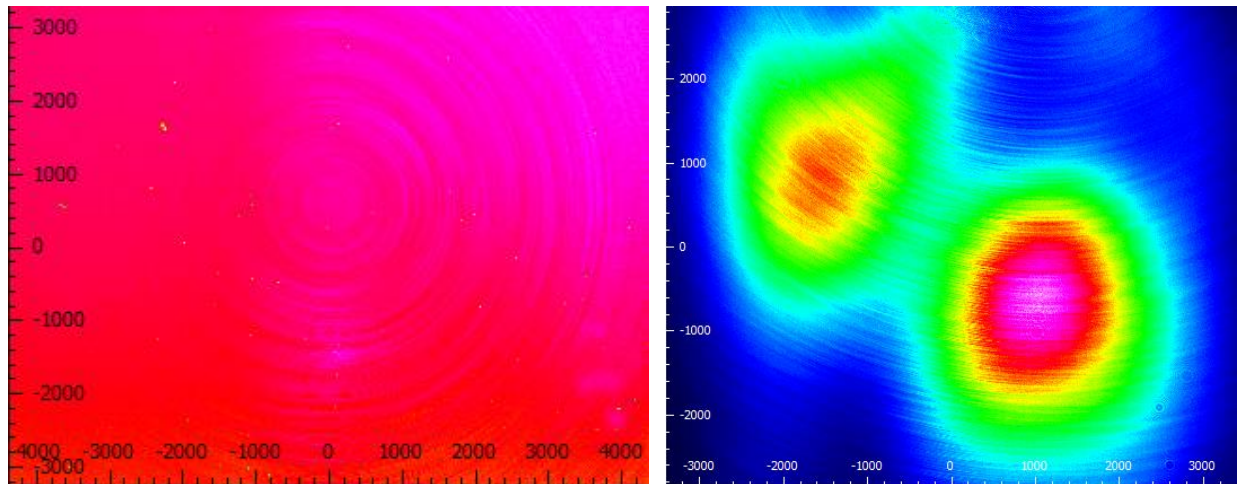


Figure 40: Far-field pattern of a 6.5 μm -diameter sapphire fiber before polishing (left) and after polishing (right) using a 532nm laser.

3.2.2 Numerical Aperture Measurement

The method used to evaluate LMV sapphire fibers in this work was designed in accordance with that used to evaluate many commercial optical fibers⁶⁷, which took advantage of the

equipment and software already used in the modal analysis procedure described in Section 3.2.1. The theory behind this method was previously described in Section 2.2; a description of the execution of this method is provided below.

Fiber samples to be tested were overfilled in direct free-space coupling using the same general setup pictured above in Figure 37. The CCD beam profiler was mounted onto a dual-axis micrometer stage with adjustable linear increments of 0.01mm. The 2D far-field projection emanating from the tip of the tested fiber was measured and the beam width was calculated using Thorlabs Beam 6.0 software. The beam width was determined using a 4σ cutoff intensity, i.e. where the beam intensity drops to 5% that of the highest measured intensity; for a Gaussian beam profile, the highest intensity is encountered in the center of the beam. The beam profiler was then moved exactly 1mm (error less than 1%) away from the tip of the fiber and the beam width was once again measured. The angle of vergence was then calculated by the software, the sine of which becomes the measured effective numerical aperture. Five measurements were made for each sample to provide statistical relevance.

3.2.3 Modal Dispersion and Laser Pulse Broadening Measurement

It was previously mentioned that modal dispersion has a direct impact on the resolution of distributed sensing techniques (Section 0). This is caused by the varied radial intensity profiles of different modes; higher-order modes tend to propagate with a higher percentage of light near the core-cladding boundary which results in a lower group velocity than modes that have more power concentrated in the core. As a result, a single laser pulse that excites multiple modes will begin to spread along the length of its propagation path as the slower higher-order modes lag behind the faster lower-order modes. This *pulse*

broadening reduces the number of data points that can be discerned along the length of a distributed fiber optic sensor, resulting in the aforementioned decrease in resolution.

Laser pulse broadening (and corresponding modal dispersion) was measured by injecting 532nm laser light into a 1m length of the tested fiber and measuring the duration of the output laser pulse using a Thorlabs SV2-FC high-speed photodetector connected to an Agilent Infinilium DSO90254A Oscilloscope. The measured voltage output versus pulse duration after traversing a 1 meter length of fiber produced an approximately Gaussian peak whose full-width half-max (FWHM) could be calculated to yield a pulse duration for comparison against other fibers measuring 1m in length. From this data the reduction in laser pulse broadening of a LMV sapphire fiber versus a commercial sapphire fiber can be calculated directly, and the corresponding impact on resolution of a distributed sensing system can also be determined.

The internally-triggered nominal pulse duration of the laser used in these studies was 700ps. Therefore, the FWHM of the original laser pulse was subtracted from the measured FWHM of the measured fiber output pulses so that dispersion differences could be accurately ascertained. To ensure statistical relevance, 64 pulses were measured and averaged for each data set, and 7 data sets were collected and averaged for each tested fiber. From this data, the difference between measured pulse durations was catalogued and impacts on sensing resolution were determined in relative terms.

Raman distributed temperature sensing is one such technique whose resolution increases with decreasing modal dispersion. The effect of modal dispersion reduction on Raman distributed sensing resolution is defined by Eq. 36 (adapted from³⁸):

$$\Delta L = \frac{ct}{2n} + 2L \left(\frac{1}{\sqrt{1 - \left(\frac{NA}{n}\right)^2}} - 1 \right) \quad \text{Eq. 36}$$

Where ΔL is the spatial resolution, c is the speed of light in a vacuum, t is the laser pulse duration, n is the refractive index of the core, L is the fiber length, and NA is numerical aperture.

The increase in spatial resolution for a Raman distributed temperature sensing system can therefore be directly calculated from the measured pulse duration difference between sapphire optical fiber of standard diameter and that of a LMV sapphire fiber through use of the variable t in the first term. Measured differences in the effective numerical aperture of SCSF of various diameters can also be used to predict improvements to spatial resolution through the second term's dependence on NA.

4 RESULTS AND DISCUSSION

4.1 Etch Reaction Chemistry

The etching of sapphire and other ceramics using sulfuric and phosphoric acids and their mixtures has been reported in some detail previously, the state of which was detailed in Section 2.4. As experimentation in this research progressed, however, satisfactory answers to some observed phenomena could not be explained by the published body of knowledge. As a result, deeper analysis was conducted on the behavior of sulfuric and phosphoric acids at elevated temperatures and their interactions with sapphire surfaces.

4.1.1 Chemical Analysis of Etching Solution

The temperatures at which sulfuric and phosphoric acids dehydrate to their diacid forms (or further dehydrate in the case of phosphoric acid to phosphorus pentoxide) have been approximately determined in the literature. Published works referenced in Section 2.4 have not included data supporting the stated transformation temperature or referenced other sources, so it was helpful to more conclusively analyze the 98% sulfuric acid and 85% phosphoric acid (remainder water) used in these etching reactions.

Since these transformations involve and require the loss of water molecules at each step, thermogravimetric analysis (TGA) was deemed useful in determining the onset temperatures of diacid and polymerization conversions. Dual Scanning Calorimetry (DSC) would also provide useful information, especially in determining the occurrence of condensation polymerization of phosphoric acid, but only specialized DSC instruments are capable of processing caustic acids without fear of damage to sensitive internal parts, to which access was not possible at the time this work was conducted.

The chemical changes expected to occur as a function of dehydration can be predicted to lend clarity to TGA results. In analysis of the 98% sulfuric acid, a 2% water weight loss would be anticipated initially, followed by dehydration into its diacid form at some discernible temperature. Sulfuric acid boils at 337°C (sea level), and there are no further anticipated transformations before its boiling point.

The transformation from $2\text{H}_2\text{SO}_4 \rightarrow \text{H}_2\text{S}_2\text{O}_7 (+\text{H}_2\text{O})$ involves a change in molecular weight from 196.17 g/mol to 178.16 g/mol, for a total difference of 18.01 g/mol or 9.2%.

Therefore, after an initial 2% water weight loss, an additional 9.2% weight loss is anticipated as temperature increases to indicate diacid conversion. Beyond this conversion, the sulfuric acid will begin to vaporize appreciably below its listed boiling point.

As-received phosphoric acid contains ~15% water as a stability and viscosity modifier.

Thus, a 15% weight decrease is expected initially before further water weight is lost in its conversion to diacid form. The transformation from $2\text{H}_3\text{PO}_4 \rightarrow \text{H}_4\text{P}_2\text{O}_7 (+\text{H}_2\text{O})$ causes molecular weight to change from 195.99 g/mol to 177.98 g/mol, for a difference of 18.01 g/mol or 9.2%, similar to the diacid conversion of sulfuric acid (since both are simply losing a water molecule). The continued dehydration through various polyphosphoric acid forms to phosphorus pentoxide ($\text{H}_4\text{P}_2\text{O}_7 \rightarrow \text{P}_2\text{O}_5 + 2\text{H}_2\text{O}$) results in a final unit molecular weight of 141.94 g/mol, or a total weight loss of about 27.6% through its final conversion (after the initial 15% water weight loss). Any further weight loss would be induced by sublimation of the remaining phosphorus pentoxide.

TGA results are included below for as-received 98% sulfuric acid (Figure 41) and 85% phosphoric acid (Figure 42). One drop of acid was placed on a platinum pan for analysis,

and samples were heated at a rate of 20°C/min, which is moderately faster than the heating rate used in etch processing reactions in this work (which typically ramped at an average rate of ~3-5°C/min).

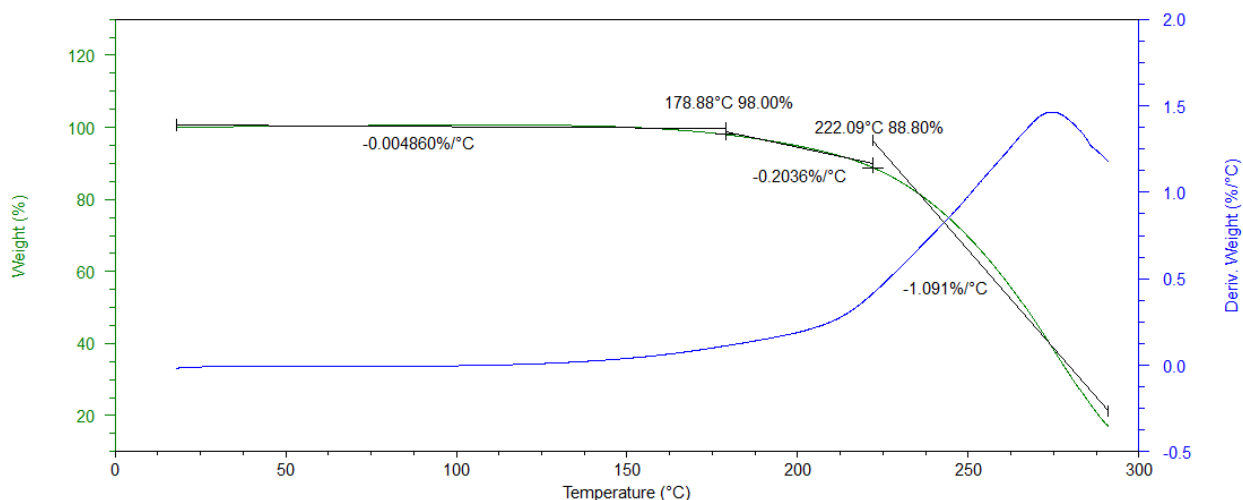


Figure 41: TGA of 98% sulfuric acid up to 300°C. Left axis and the green line represent the total % weight change with temperature, and the right axis and blue line represent the derivative of the % weight change per °C. Points of discussion are labeled, with temperature/weight% above and slope below.

The theoretically calculated transition points for sulfuric acid seem to occur as anticipated. At the heating rate of 20°C/min the initial 2% added water is relinquished near 180°C, when a clear change in slope heralds the initiation of diacid formation. Once diacid transformation is complete after a predicted total weight loss of 11.2% (2% for added water loss plus 9.2% for diacid conversion) there is a drastic change in weight loss rate caused by evaporation of the sulfuric acid. Sulfuric acid begins to evaporate appreciably before its boiling point of 337°C; once the diacid transformation is complete and all water is lost, there is nothing left to inhibit rapid evaporation.

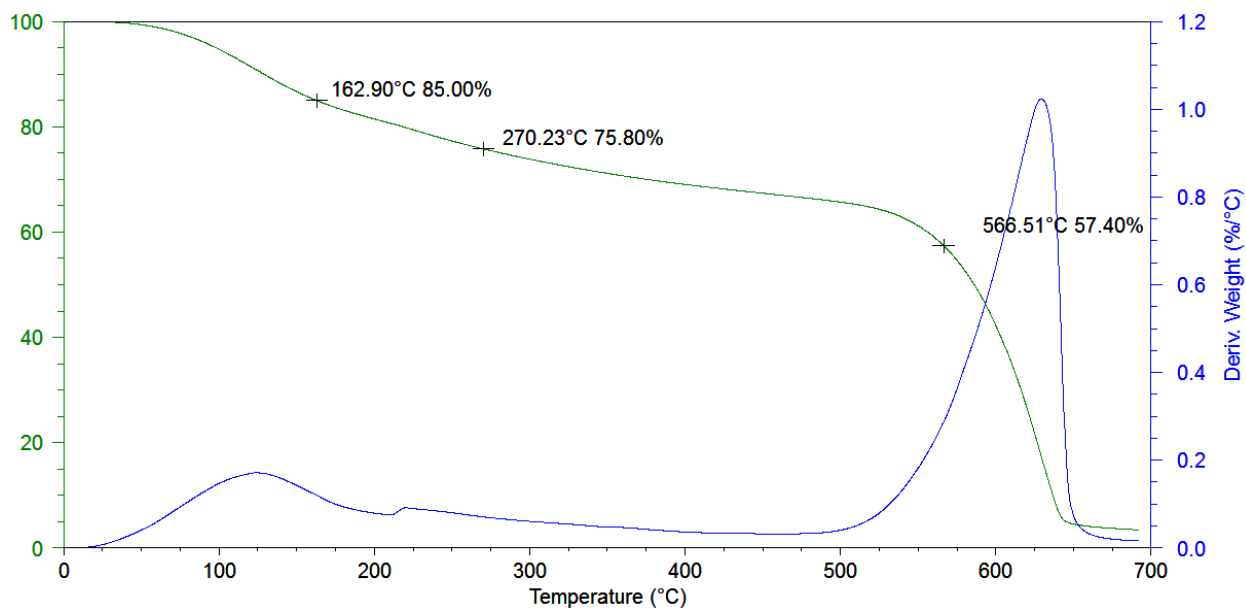


Figure 42: TGA of 85% phosphoric acid up to 700°C. Left axis and the green line represent the total % weight change with temperature, and the right axis and blue line represent the derivative of the % weight change per °C. Points of discussion are labeled.

The TGA of phosphoric acid supports the hypothesized transformations, though the transition points are not very distinguished since diphosphoric acid (the diacid morphology) forms an equilibrium solution of phosphoric acid, diphosphoric acid, and polyphosphoric acid when molten⁸⁹, and there are multiple varieties of polyphosphoric acid that may be formed⁹⁰. Additionally, the heating rate of 20°C/min may be too rapid to accurately isolate the transition temperatures of phosphoric acid, and at these temperatures the compounds present are expected to display some amount of volatility.

Regardless, a significant peak in the rate of weight loss curve (blue) signals the anticipated 15% water weight loss. An additional, smaller peak is noticeable around 220°C (more easily discernible with the y-axis rescaled in Figure 43) revealing the further dehydration of the phosphoric acid to its diacid form. Dehydration continues until diacid formation should be complete as an additional 9.2% weight is lost, and then dehydration continues at

a smooth rate; the lack of a distinct change in dehydration rate is likely attributable to the aforementioned complexity of the composition (regarding various amounts and varieties of diphosphoric and polyphosphoric acid). Phosphoric acid has a relatively low vapor pressure even at elevated temperatures (less than 5mmHg at 180°C⁹¹), so little of the observed weight loss is likely attributable to vaporization in this temperature range.

Eventually, however, it becomes clear that all water has been removed from the chemical structure, leaving only anhydrous phosphorus pentoxide at the remaining weight of 57.4%, as predicted. Since phosphorus pentoxide normally sublimates at 360°C⁹² and there is no longer any water supporting the presence of more stable structures, the remainder rapidly sublimates.

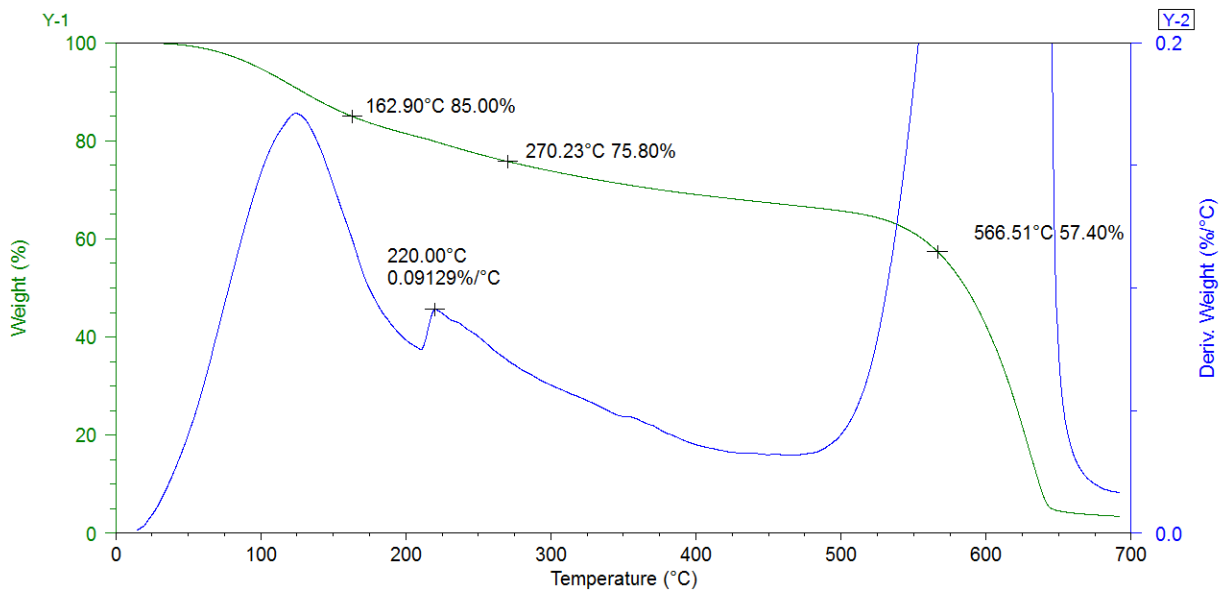


Figure 43: Rescaled TGA of 85% phosphoric acid up to 700°C reveals the temperature of diacid formation at a heating rate of 20°C/min.

The predicted transformations (supported by TGA measurements) add complexity to etching experiments using phosphoric acid alone. While sulfuric acid rather simply dehydrates to diacid form and then rapidly evaporates, phosphoric acid transitions to

diacid form as well as numerous potential varieties of polyphosphoric and metaphosphoric acids (likely simultaneously in some sort of equilibrium⁹⁰) before ultimately forming anhydrous phosphorus pentoxide once fully dehydrated.

As the formation of sulfuric acid's diacid form occurs well below the temperatures used for etching sapphire, there is only one etch rate and corresponding activation energy that may be measured: that of the disulfuric acid. Etch rates and activation energies calculated for phosphoric acid, however, represent the cumulative effects of a variety of different chemical structures which vary not specifically with temperature or time but rather due to state of dehydration and equilibrium with other stable morphologies. Therefore, parameters such as heating rate, dwell temperature, and total dwell time could cause significant variation in measured etching rates at a nominal etching temperature (since they in turn can cause significant variation in the compositional ratio of the di/poly/metaphosphoric acid, which each have their own distinct etching rate and activation energy).

To prove this point, two etching sessions were carried out using fresh as-received 85% phosphoric acid at a nominal temperature of 320°C. In one experiment the sapphire fiber to be etched and measured was inserted into the solution as soon as it reached 320°C (as was typically done in all reported etching experiments); in the other experiment, the solution was allowed to remain at 320°C for 5 hours before insertion of the sapphire fiber sample. The first solution, which was a clear liquid of fairly low viscosity, induced significant etching of the sapphire fiber. The second solution, which became a clear liquid of much higher viscosity, induced far less etching during the same 3-hour period (Figure 44).

Immediate immersion of sapphire fiber in phosphoric acid once the desired temperature of 320°C was reached resulted in 7-8µm diameter reduction after 3 hours of exposure while allowing the solution to remain at 320°C for 5 hours before sample immersion resulted in only 1-1.5µm of diameter reduction over the same etching duration.

The most logical explanation for this behavior is that the temperature of 320°C is sufficient to cause diacid formation and further dehydration into various polyphosphoric acids (as is also supported by TGA measurements reported above), but the evacuation of water from the lidded beaker to allow conversion of diphosphoric acid to polyphosphoric acid requires several hours to complete. Therefore, a larger ratio of the more etch-active diphosphoric acid is present in the solution that has a shorter heating history than the solution that has allowed further dehydration into a greater ratio of polyphosphoric acids, which would be less active (or not at all active) in etching of sapphire since more of its active sites are tied up in the polymer chain.

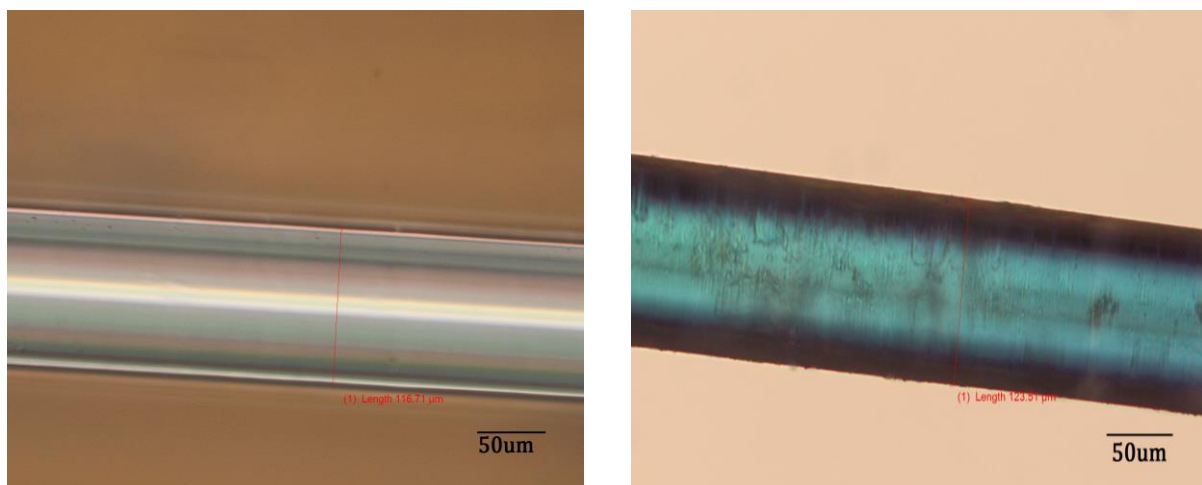


Figure 44: The etching rate of sapphire fiber by phosphoric acid at 320°C is much greater if the phosphoric acid solution is fresh (left) compared with phosphoric acid that has been heated for several hours (right). Differences in coloration are due to use of polarizing filter during optical microscopy of the birefringent sapphire fiber to help discern fiber edges.

Furthermore, heating phosphoric acid to temperatures of 375-395°C was observed to be sufficient to produce significant formation of phosphorous pentoxide over time, resulting in a slurry-like mixture of polyphosphoric acid and phosphorous pentoxide (Figure 45).

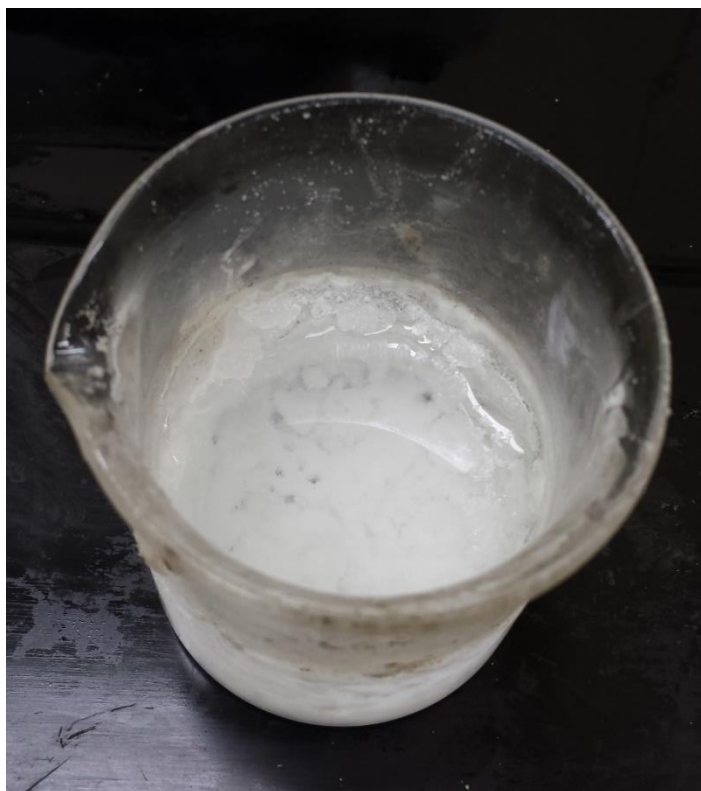
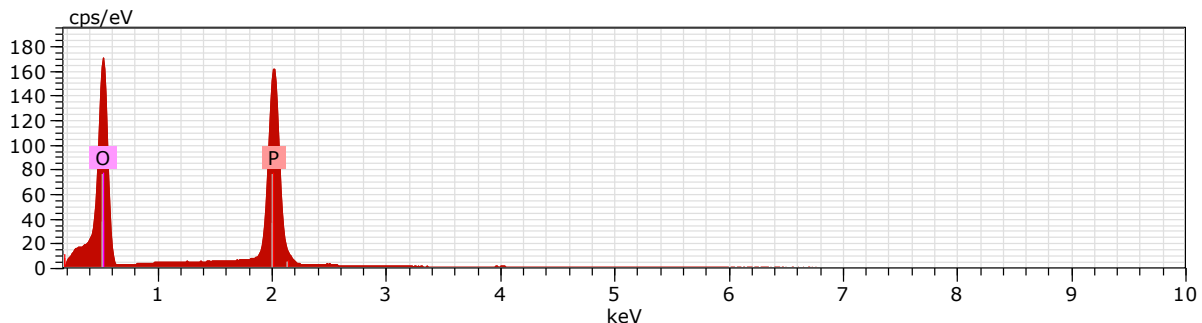


Figure 45: Heating of phosphoric acid to temperatures above 350°C for extended periods of time initiates dehydration of polyphosphoric acid to phosphorous pentoxide

The white powder isolated from these reactions was extremely hygroscopic, which is characteristic of phosphorous pentoxide. To further verify that P_2O_5 was indeed forming (rather than a reaction product of phosphoric acid and the silica beaker such as that reported in Section 3.1.1), EDS was conducted on a sample of the powder.



El	AN	Series	unn. C [wt.%]	norm. C [wt.%]	Atom. C [at.%]	Error (1 Sigma) [wt.%]
O	8	K-series	32.22	68.26	80.63	3.44
P	15	K-series	14.98	31.74	19.37	0.59
Total:			47.21	100.00	100.00	

Figure 46: EDS supports the assumption that the composition of the white powder formed after extended heating of phosphoric acid is indeed phosphorous pentoxide.

EDS did not detect any elements other than oxygen and phosphorus; therefore, the white powders formed during heating of phosphoric acid are not products of any reaction with the beaker. Furthermore, the detected ratios of phosphorus and oxygen approximately line up with the anticipated weight and atomic ratios of P_2O_5 (28 at% of phosphorus to 72 at% oxygen is anticipated and 20 at% P to 80 at% O is measured). Additional compounds present with higher oxygen ratios (most likely $H_2P_2O_7$) could be responsible for the increased oxygen ratio in the EDS measurements.

The intricate transitions of phosphoric acid add complexity to the analysis of etching rates for phosphoric acid, as will be discussed in detail in the following section.

4.1.2 Initial Measured Etch Rates of Sapphire Optical Fiber

The c-axis sapphire optical fiber used in all experimentation, whose a-axis is etched for diameter reduction, will etch appreciably in pure sulfuric acid at temperatures exceeding 300°C, but at a lower rate than that observed using the 3:1 mixture of H₂SO₄:H₃PO₄. Phosphoric acid enables more rapid etching than sulfuric acid in the 300-340°C range, but mixing the two at a 3:1 molar ratio of H₂SO₄:H₃PO₄ yields etch rates that are greater still. Etch rates for each solution across a range of temperatures are reported in greater detail in Section 4.1.3; initial measurements that guided early experimental work are displayed in Figure 47. The etch rate (as measured by optical fiber diameter reduction) using sulfuric acid, phosphoric acid, or the 3:1 mixture was measured where the temperature in each was maintained at 320±2°C. The etch rate for the 3:1 mixture was observed to be greater than 10x as fast as sulfuric acid alone and significantly greater than phosphoric acid at this temperature.

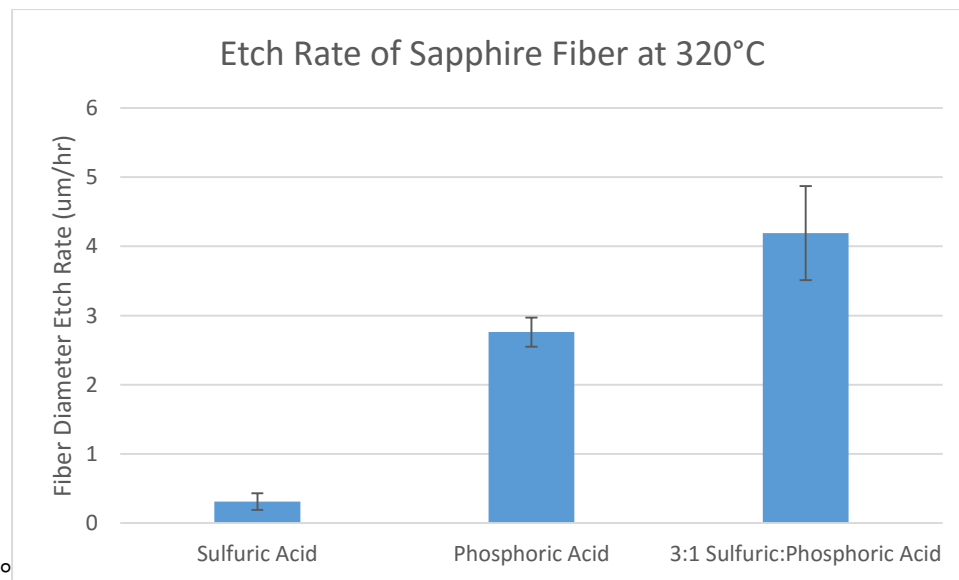


Figure 47: Sapphire optical fiber diameter etch rate is much faster for 3:1 H₂SO₄:H₃PO₄ than sulfuric acid or phosphoric acid alone at 320°C.

Optical microscopy was used to analyze fiber surfaces and measure diameter before and after etching using an Olympus BX51 microscope with StreamMotion software. Multiple measurements were taken across the length of an etched fiber to ensure consistency, and multiple fibers were etched in separate experiments under the same conditions to increase the statistical reliability of the data and reduce error.

Initial experiments concluded that etching would not occur in any appreciable manner using the 3:1 $\text{H}_2\text{SO}_4:\text{H}_3\text{PO}_4$ mixture below temperatures of 280-300°C. In Figure 48, for example, a 200 μm -diameter sapphire fiber that was submersed in the 3:1 etch solution at 270°C for 5.5 hours showed no change in diameter. Therefore, extensive study was conducted on the etch rates of sapphire optical fibers over the temperature range of 300-340°C, at which point the sulfuric acid boils, placing an upper limit on etch temperature. The etching rates of sapphire fiber at temperatures of 300-340°C was measured at 10°C intervals using sapphire fiber with an initial diameter of 200 μm . After etching, diameter measurements were taken at 3-5 locations along the fiber, and experiments were repeated at least three times at each temperature to increase statistical relevance and calculate a standard deviation for the measured etch rates reported in Figure 49.

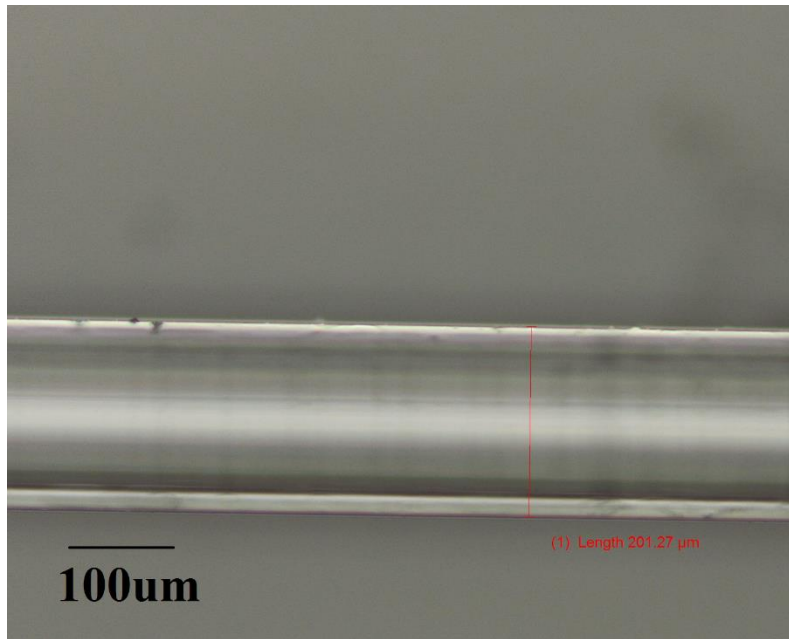


Figure 48: 200µm diameter sapphire fiber remained unchanged after 5.5 hours exposure to etch solution at 270°C.

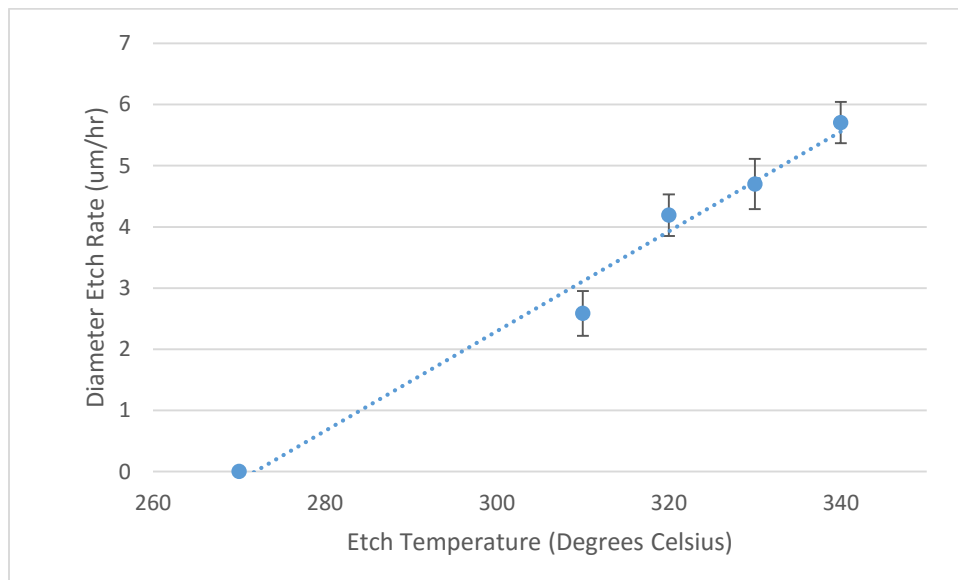


Figure 49: The etch rate of sapphire optical fiber in 3:1 molar $H_2SO_4:H_3PO_4$ increases as temperature increases. As can be anticipated, etch rate increases as etch temperature increases to the boiling point of the sulfuric acid component, with a maximum diameter reduction rate of around 5.7 µm/hr possible at the maximum etching temperature of ~343°C.

In Figure 50, the diameter of a sapphire optical fiber with an initial diameter of $50\mu\text{m}$ was reduced to submicron diameter over the course of three etching sessions, each at 343°C . The diameter of the fiber was measured between etching sessions and the diameter reduction rate was found to be linear.

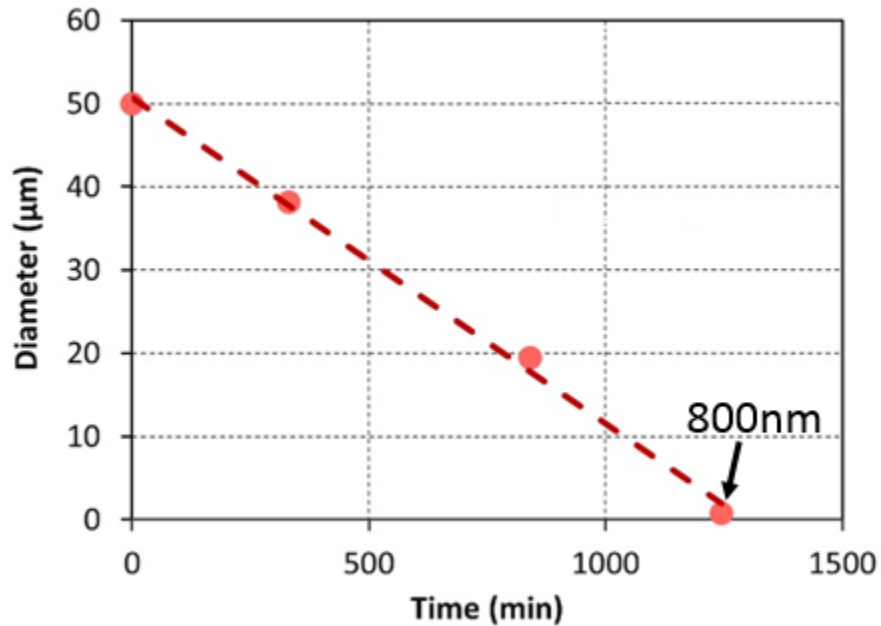


Figure 50: Diameter of a sapphire fiber is reduced linearly during etching. Error bars are present but not visible in the chart, as measured variation along this single sample was very small.

4.1.3 Etching Rates

The etching rates of sulfuric acid, phosphoric acid, and their 3:1 mixture upon c-plane sapphire surfaces have been determined and reported by Dwikusama et al⁷⁶ and are copied below in Table 2. A recent study on etching of patterned sapphire substrates using sulfuric and phosphoric acid also notes etching rates extrapolated from etching depth and width⁹³, but the crystallographic orientation of the tested sapphire wafers is never identified. The authors also suggest that additional geometrical considerations (the SiO_2 masks deposited by the authors leave exposed, etchable sapphire regions measuring only a few microns

across and were irregular in shape) prevent this data from relating directly to rates of etching bulk sapphire.

Table 2: Etching rates of relevant acids of c-plane sapphire reported by Dwikusama⁷⁶ at 320°C

Solution Composition	Etch Rate ($\mu\text{m/hr}$)
98% H_2SO_4	~ 3.0
85% H_3PO_4	0.1
3:1 $\text{H}_2\text{SO}_4:\text{H}_3\text{PO}_4$ (by volume)	~ 1.5

The authors concluded that phosphoric acid would begin etching at lower temperatures and that sulfuric acid would begin contributing at higher temperatures and to a greater extent due to its higher acidity, explaining the higher observed etch rate of c-plane sapphire using sulfuric acid over phosphoric acid (Figure 51). The 3:1 mixture reasonably records an intermediate etch rate.

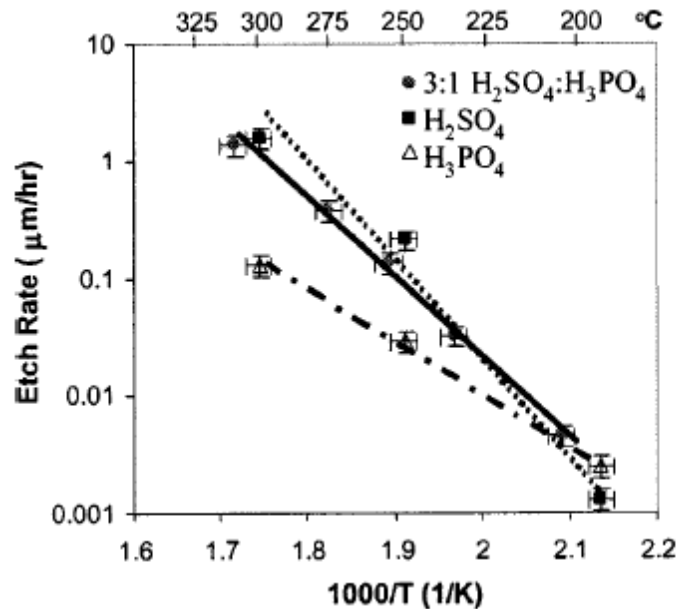


Figure 51: Published etch rates of c-plane sapphire as a function of reciprocal temperature⁷⁶. Reprinted with permission from the Electrochemical Society.

However, similar experiments carried out in the etching of a-plane surfaces of sapphire optical fibers demonstrate different behavior. Specifically, in addition to a-plane sapphire generally etching more rapidly than c-plane sapphire, the etch rate of c-plane sapphire at temperatures of 300-320°C was reported⁷⁶ to be most rapid using sulfuric acid. Phosphoric acid recorded a miniscule etch rate, and the 3:1 H₂SO₄:H₃PO₄ solution produced an intermediate etch rate of c-plane sapphire, but very different behavior was initially observed in etching of a-plane sapphire optical fiber surfaces.

The etching rates of a-plane sapphire have been experimentally determined for the first time in the current work using sulfuric and phosphoric acids as well as a 3:1 molar ratio of the two. Most samples were immersed in each etching solution for 3 hours with the exception of those exposed to sulfuric acid at 330°C and 337°C, as the proximity to its boiling point induced rapid fuming and required exposure to be reduced to 1 hour to prevent complete evaporation.

The results of these measurements are seen in Figure 52. Of the evaluated etchants, sulfuric acid induced the lowest etch rate on a-plane sapphire when used alone, contrasting the reported etch rates of c-plane sapphire by sulfuric and phosphoric acids. Interestingly, the 3:1 H₂SO₄:H₃PO₄ (molar) mixture actually induced a greater etch rate than either phosphoric acid or sulfuric acid alone.

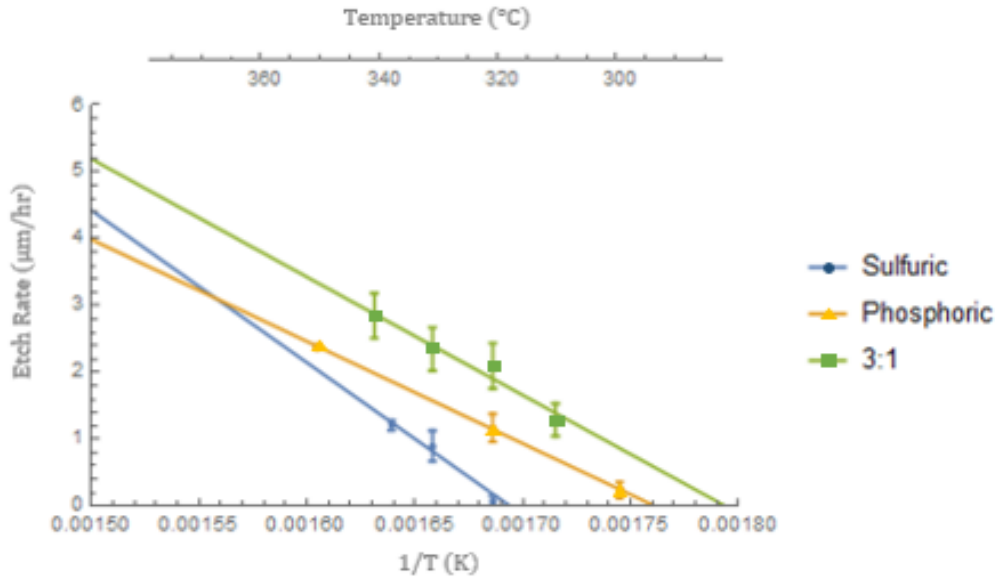


Figure 52: The measured etch rates of a-plane sapphire varied according to etchant composition.

The boiling point of sulfuric acid limits its maximum etching temperature to 337°C at atmospheric pressure. The mixture of sulfuric and phosphoric acid displays slight azeotropic behavior, pushing the boiling point of the sulfuric acid component (and therefore the maximum etching temperature of the solution at standard pressure) to approximately 343°C.

Phosphoric acid will not boil in this temperature range but can further dehydrate as temperatures exceed 343°C to form di/poly/metaphosphoric acid and then phosphorous pentoxide (as just described in Section 4.1.1). As the temperature limit of etching via phosphoric acid alone is significantly higher than that imposed by the 337°C boiling point of sulfuric acid, etching rates of the a-plane sapphire can be increased significantly at elevated temperature, with rates of more than 11µm/hour observed using phosphoric acid at 395°C compared to the maximum attainable rate of 2.85µm/hour using the 3:1 H₂SO₄:H₃PO₄ mixture at its boiling point. Etch rates may reach well beyond 20µm/hour if

phosphoric acid is heated above 405°C, as the entirety of a sapphire fiber with a starting radius of 62.5μm was etched away in 3 hours in one experiment.

However, while the etch rate increases using phosphoric acid at elevated temperature, the propensity of surface defects such as pitting also seem to increase, such as that seen in Figure 53. The reason for this is not clear; it has been suggested⁷⁶ that the cause for such pitting is that phosphoric acid preferentially attacks crystallographic defect sites.

Regardless of the mechanism causing pitting using pure phosphoric acid, fibers without discernible defect in surface quality are produced through etching with the 3:1 mixture of sulfuric and phosphoric acids at temperatures around 340°C (Figure 54).

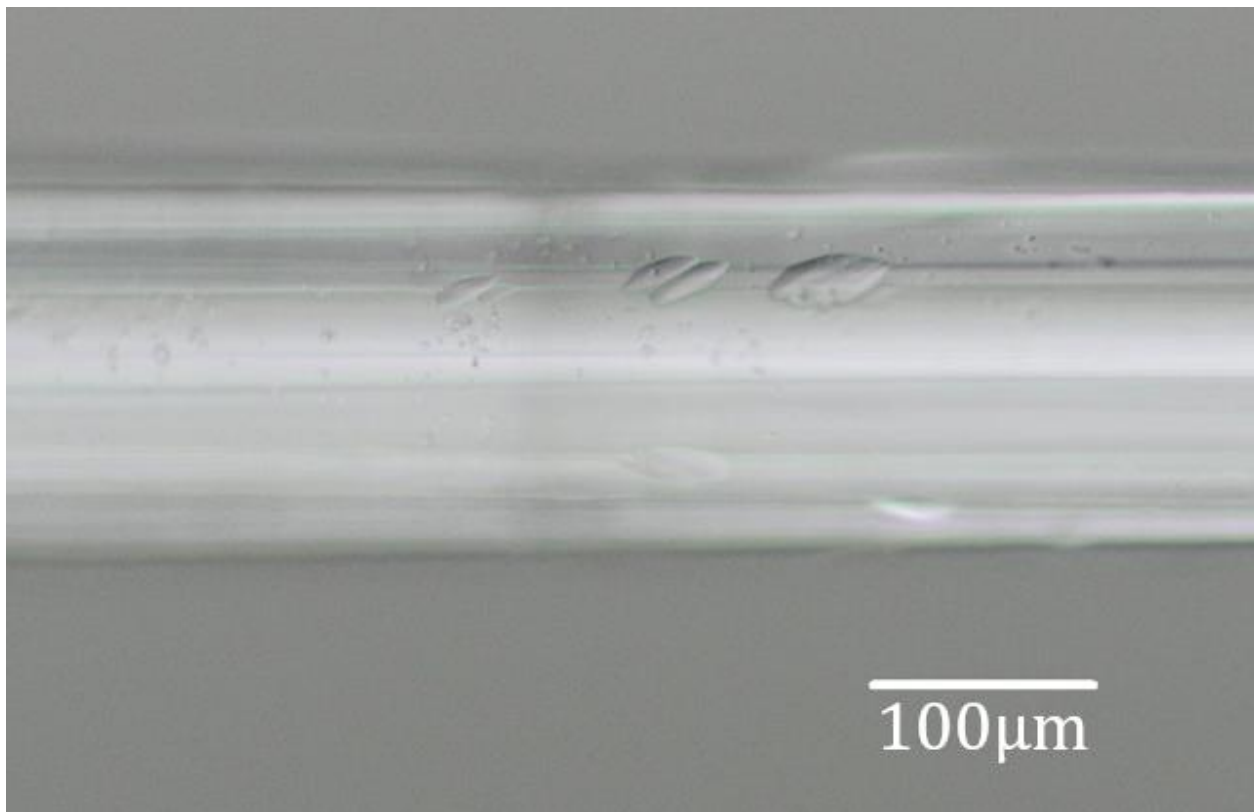


Figure 53: Significant occurrence of pitting and other surface defects were observed when using pure phosphoric acid as an etchant of a-plane sapphire at elevated temperatures (temperature during etching of pictured sapphire fiber was 365°C).

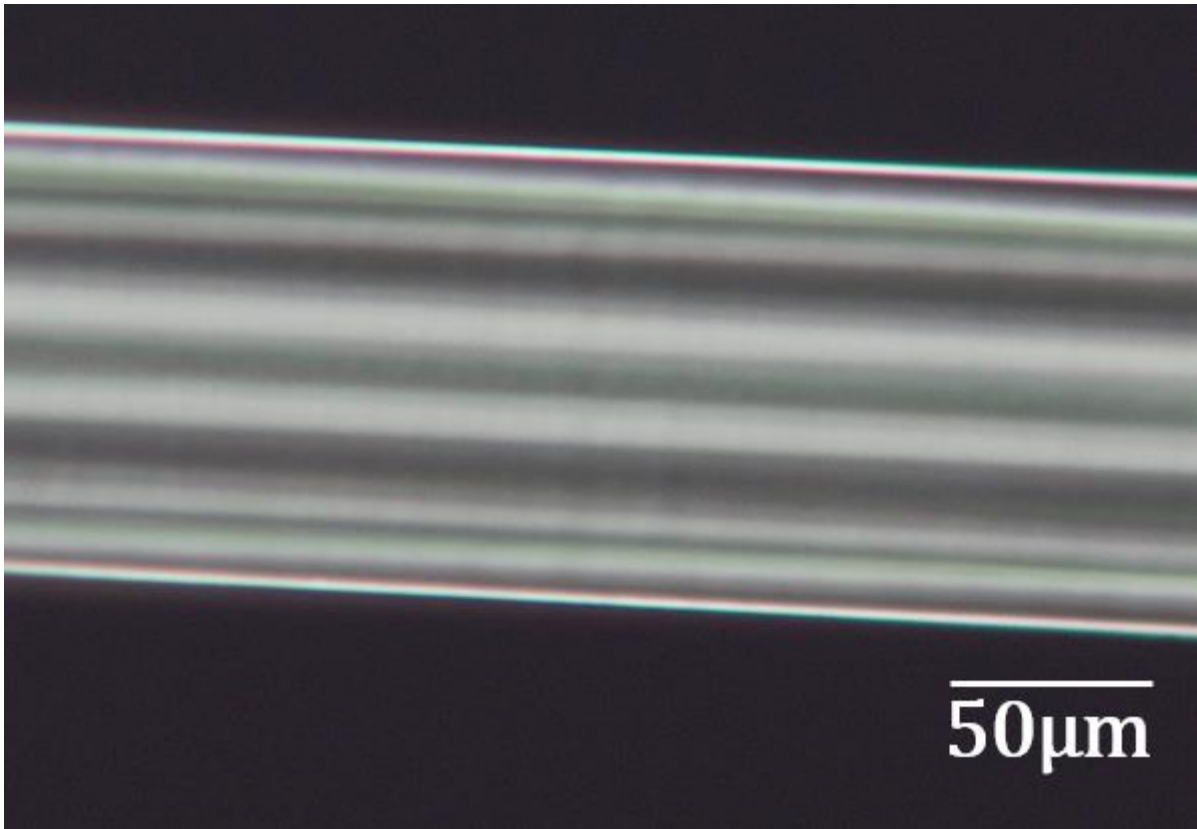


Figure 54: No discernible surface defects are observable when a 3:1 ratio of sulfuric and phosphoric acids are used to etch sapphire fiber at around 340°C.

4.1.4 Differences in c-plane and a-plane Etching Behavior

The complex composition present through the dehydration of phosphoric acid at etching temperatures initially leaves some interesting questions whose answers may help explain the observed etching behavior. First, the etch rate of a-plane sapphire by phosphoric acid itself follows a strong linear fit at measured temperatures ranging from 300°C-350°C.

However, very large deviation from the linear fit occurred during etching at temperatures of 375°C, 385°C, and 395°C (Figure 55). As with previous etch rate measurements, experiments were repeated at least three times at each temperature and diameter measurements were taken at 3-5 points along each etched fiber to produce the measured rates and standard deviation.

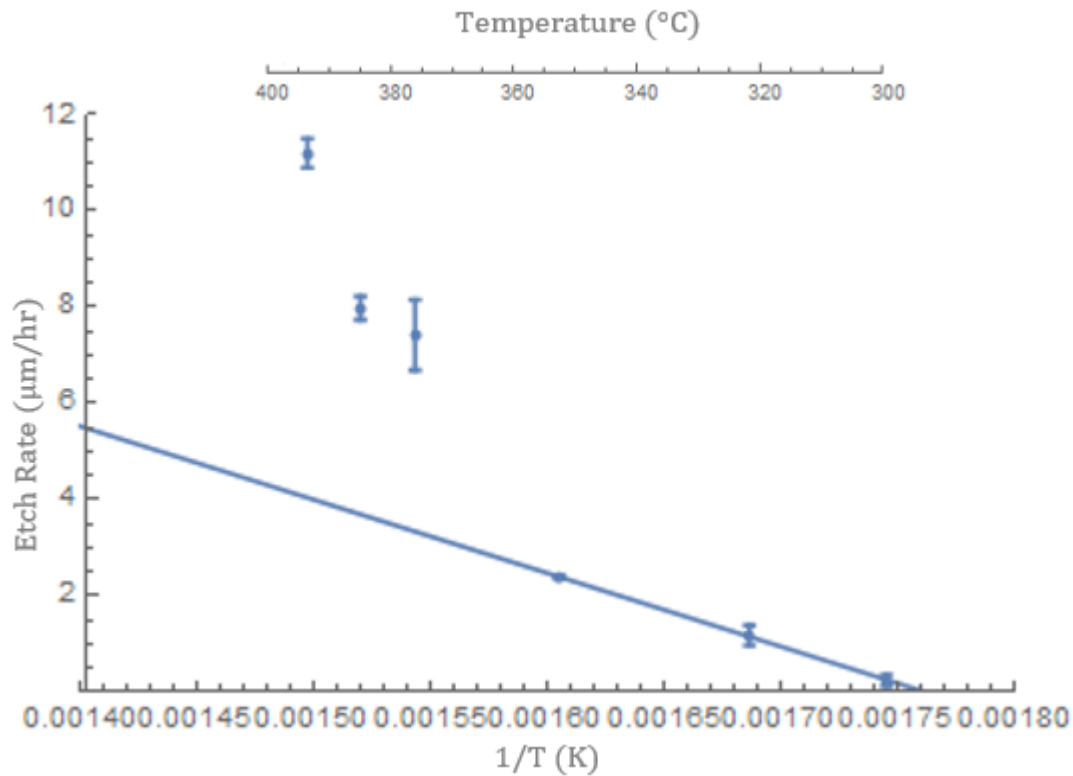


Figure 55: Etch rate of a-plane sapphire by phosphoric acid versus temperature follows the expected linear fit through 350°C. Measured etch rates at 375°C, 385°C, and 395°C strongly deviate from linear behavior.

Not only do etch rate data at higher temperatures deviate from the linear fit of the lower temperatures, but the high-temperature data itself seems to follow an exponential rather than linear curve fit. There are multiple potential causes of this behavior, but one likely explanation lies in the complex compositional ratio of the di/poly/metaphosphoric acid with phosphorus pentoxide, which was visibly forming at these temperatures to give the mixture an opaque white slurry appearance (originally pictured in Figure 45).

The etch rate of sapphire by pure anhydrous phosphorus pentoxide (P_2O_5) was not determined in this study. However, phosphorus pentoxide is known to be a highly caustic substance and it was certainly present in greater ratios at increasing temperatures and

correlating dehydration states. It may be reasoned that the observed non-linear fit of the etch rate data at these high temperatures was attributable to the increasing ratio of phosphorus pentoxide compared to di/poly/metaphosphoric acid and that perhaps P_2O_5 etches a-plane sapphire at a greater rate than diphosphoric acid.

Secondly, that the 3:1 $H_2SO_4:H_3PO_4$ mixture should exhibit a significantly greater etch rate than either of its constituents alone was initially unexpected, especially since published data regarding the etch rates of c-plane sapphire demonstrated an intermediate etching rate for the mixture. The answer may again lie in the compositional complexity of the dehydrating phosphoric acid.

One published source⁷⁵ speculated that differences in the visual appearance and viscosity of the 3:1 $H_2SO_4:H_3PO_4$ mixture versus pure H_3PO_4 after heating to the same temperature could be caused by sulfuric acid interfering in some way with diphosphoric acid's continued dehydration to polyphosphoric acid, though the mechanism by which this occurs was not discussed. If true, this may also explain the enhanced etch rate of a-plane sapphire by the 3:1 mixture over pure sulfuric or phosphoric acids. It was previously noted that lengthy heating of phosphoric acid at 320°C before etching drastically reduced its etch rate, presumably due to greater dehydration over time to form a higher ratio of poly/metaphosphoric acid, which is not expected to be as active in attacking the sapphire surface as its more acidic diacid form. The presence of sulfuric acid may molecularly interfere with the polymerization of diphosphoric acid or simply contribute more water to the system (as it is also dehydrating to diacid form), lengthening the amount of time where

greater ratios of diphosphoric acid are present versus polyphosphoric acid and therefore increasing the total etch rate over pure phosphoric acid at the same temperature and time.

This behavior would not have been noticeable in previously-published etching studies on c-plane sapphire since sapphire of this crystallographic orientation demonstrated a miniscule rate of etching by pure phosphoric acid compared with that of sulfuric acid.

Therefore, any additional contribution made by an increased presence of diphosphoric acid during etching would not have nearly the effect on c-plane surfaces as a-plane surfaces.

Finally, the overall etch rates of a-plane sapphire using phosphoric acid and the 3:1 mixture determined in this work are significantly greater than those reported for c-plane sapphire using two of the three etchants. Linear etch rates of a-plane sapphire using the 3:1 mixture doubled to more than $2\mu\text{m}/\text{hour}$ compared with its c-plane counterpart at the same temperature ($\sim 1\mu\text{m}/\text{hr}$). Phosphoric acid's etch rate of a-plane sapphire was measured to be a whole order of magnitude greater than that of c-plane ($1.17\mu\text{m}/\text{hr}$ versus $\sim 0.1\mu\text{m}/\text{hr}$).

There may be an explanation for this observation. Sapphire's c-plane orientation is the most atomically dense of all sapphire orientations and is formed of interchanging O-Al-Al-O-Al-O layers that present no crystallographic weaknesses (such as strained or stretched atomic bond lengths). Its perpendicular planes, however, contain interchanging O-O-Al-O-Al-O-O—O-Al-O-Al-O layers, and the bonds between the extended O—O layers are weakened at this strained bond length⁸⁷. This weakness may explain the faster a-plane etch rates; during acidic attack on sapphire the H^+ ions are reported to attack the oxygen in bridging moieties⁷⁶. In sapphire's c-plane oxygen is always bound between aluminum atoms (Al-O-Al), so it would follow logic that a greater opportunity for H^+ attack could exist

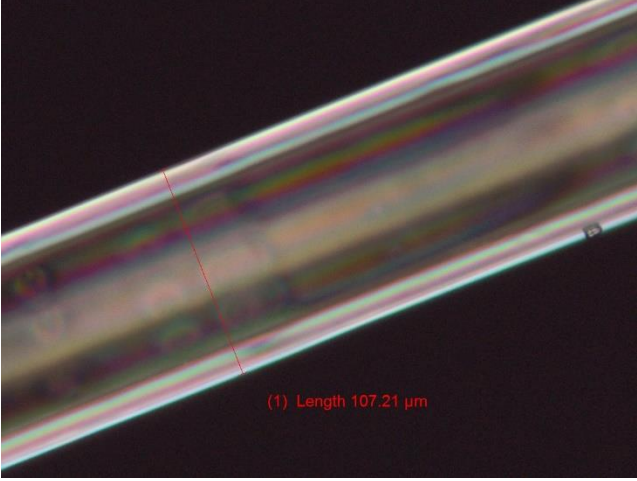
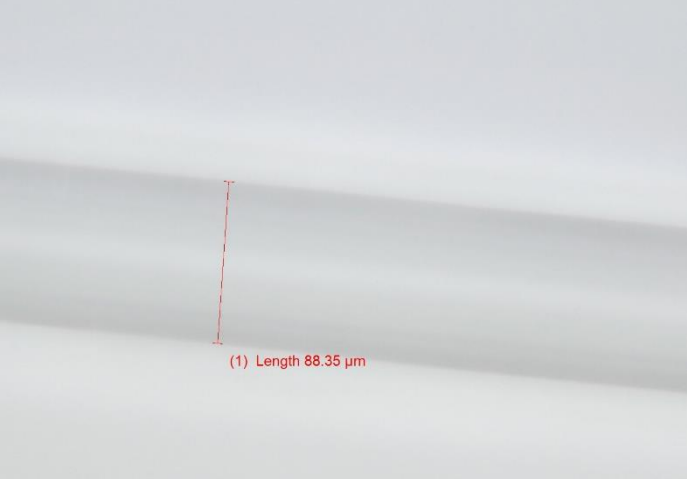
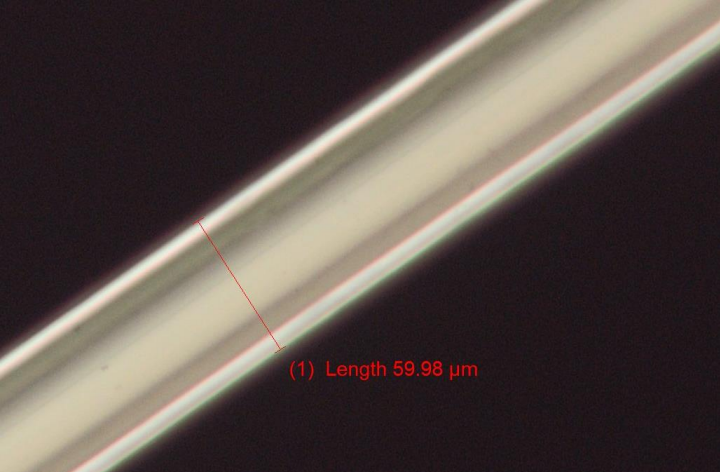
where the strained O—O bonds are exposed. If phosphoric acid does indeed target crystallographic defect sites as reported⁷⁶ at a much greater rate than sulfuric acid, this would explain why the a-plane etches more quickly than the c-plane using phosphoric acid and mixtures containing phosphoric acid.

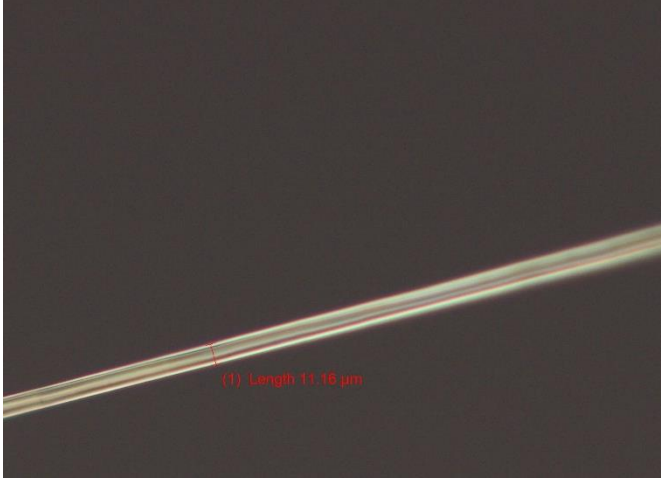
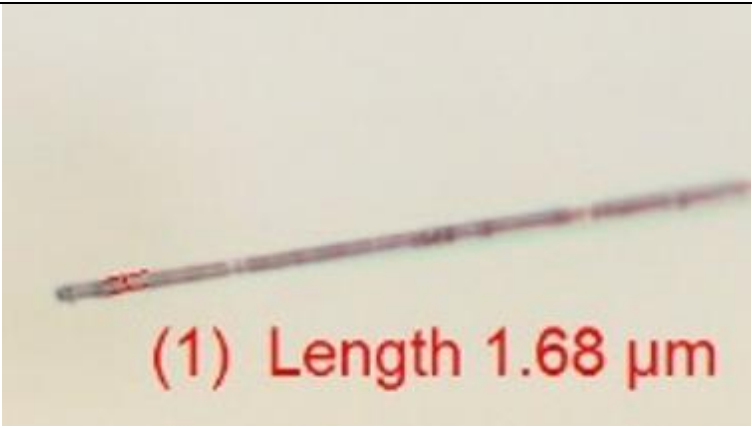
Regardless, the primary cause of differences between a-plane and c-plane etching behavior using sulfuric and phosphoric acid solutions seems to be primarily attributed to their reaction with phosphoric acid. This behavior has been explained in this research through the observance of greater etch rates of a-plane sapphire using phosphoric acid than c-plane sapphire, the deconvolution of the varied morphologies present in phosphoric acid at etching temperatures over time, and the inherent crystallographic differences in c-plane and a-plane sapphire that would make a-plane orientations especially vulnerable to attack by phosphoric acid as noted by other sources^{76,93}.

4.1.5 Etched Fiber Diameter Consistency and Surface Cleanliness

In Table 3 a sampling of achieved fiber diameters are presented to demonstrate the control and cleanliness of the process. No etching deposits have been observed on reduced-diameter fiber samples since the implementation of borosilicate shielding at the air-acid interface.

Table 3: Etching of sapphire fiber to a desired diameter can be conducted cleanly and predictably using the developed etching equipment. As the 1.7 μm fiber was imaged at maximum magnification (1000x), the image at the bottom of the table is digitally enlarged for greater visibility.

Measured Diameter	Fiber Image	
107 μm		 <p>(1) Length 107.21 μm</p>
88 μm		 <p>(1) Length 88.35 μm</p>
60 μm		 <p>(1) Length 59.98 μm</p>

11 μm	 <p>(1) Length 11.16 μm</p>
1.7 μm	 <p>(1) Length 1.68 μm</p>

While fiber surfaces remain clean and diameter reduction was consistent across experiments, a slight amount of tapering (Figure 56) occurs from base to tip using the apparatus in which LMV fibers were created; an etch rate differential of about 0.2 $\mu\text{m/hr}$ was consistently observed. This is likely attributed to the slightly higher temperature of the etch solution at the bottom of the vessel where resistance heating coils are most dense, inducing a $\sim 1\text{-}2^{\circ}\text{C}$ measured difference from top to bottom of the solution over a span of $\sim 20\text{cm}$.

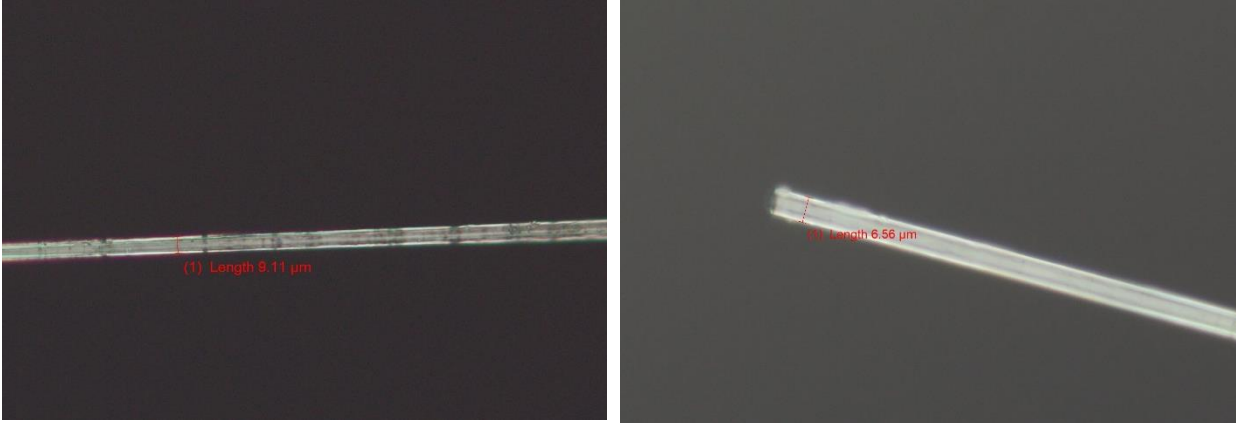


Figure 56: One sapphire fiber sample whose mode characteristics were measured tapered from 9.1 μm at its base (left) to 6.5 μm at its polished tip (right) over the course of its 10cm length. The two images are of different magnifications.

The process also demonstrated excellent repeatability across etching sessions. Three sapphire fibers with an initial diameter of 125 μm and length of 1m were etched using the same equipment and conditions in separate experiments. Fresh 3:1 H₂SO₄:H₃PO₄ solution was used in each experiment, and each session lasted 24 hours. The diameter of each etched fiber was then measured at both ends (located at the top and bottom of the etching vessel) and is reported in Table 4 below.

Table 4: Three 1-meter length sapphire fibers etched separately under the same conditions and duration measured very similar in final diameter from one end to the other.

Sample	Top Diameter (μm)	Bottom Diameter (μm)
A	82.0	73.1
B	80.9	73.4
C	79.6	74.4
Average	80.8	73.6
Standard Deviation	1.2	0.7

The recorded heating profile was consistent across each experiment, as might be anticipated based on the close similarities in final diameter. The temperature of each etching solution is plotted below in Figure 57.

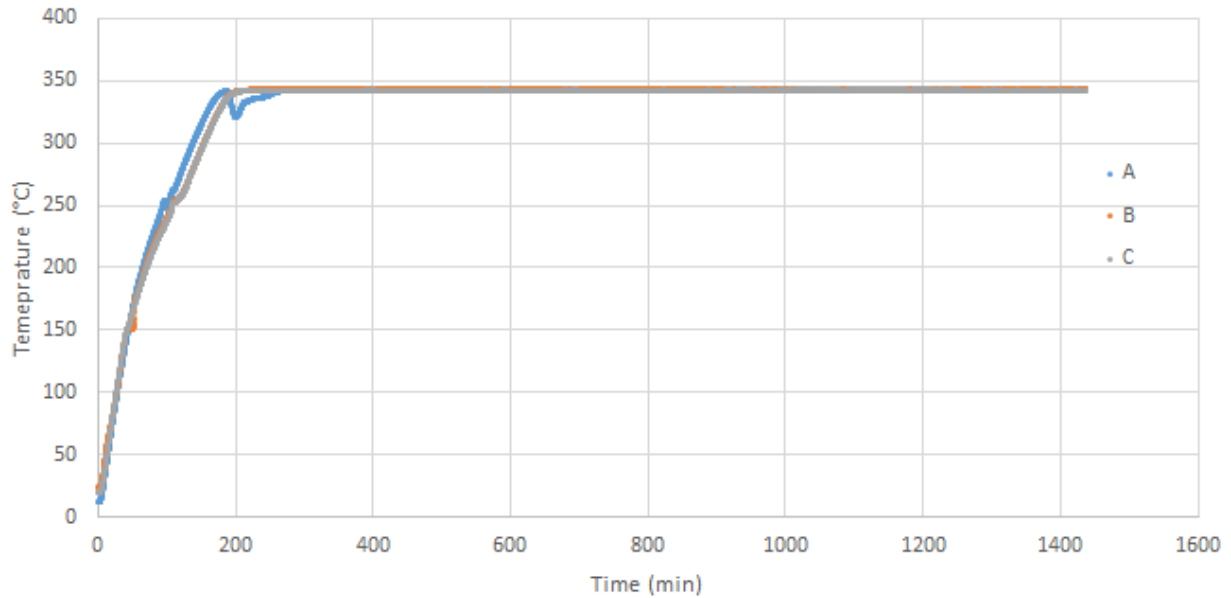


Figure 57: The heating profile was consistent between processing of three separate 1-meter long sapphire fibers.

4.2 Reduced Diameter Single-Crystal Sapphire Optical Fibers

4.2.1 Submicron Diameter Sapphire Fiber

The wet-acid etching method characterized in Section 4.1 produced the first known submicron diameter sapphire fiber, which had a final minimum diameter of just under 800nm. Scanning electron microscopy (SEM) was used to view the fiber with its smallest point visible in Figure 58.

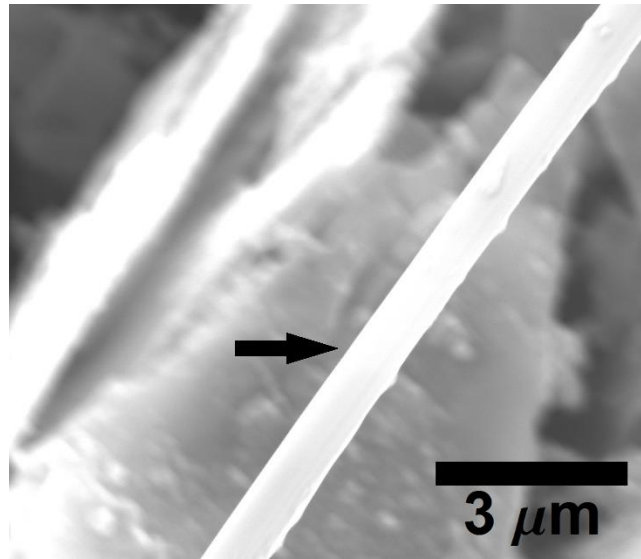


Figure 58: A 50 μm diameter sapphire fiber was etched to a final minimum diameter of less than 800nm.

The total length of this first submicron diameter sapphire fiber was around 400 μm .

4.2.2 Tapered Sapphire Optical Fiber

Tapered sapphire optical fibers were also produced by introducing a temperature gradient across its length. In this manner, a 50 μm diameter sapphire fiber was etched at a continuously variable rate from bottom to top, resulting in a fiber that is 25 μm in diameter in its top-most exposed area and less than 100nm at the tip over a total length of 1.1cm.

Tapering is controlled by inducing a temperature gradient between the top and bottom of the etching vessel in which the sapphire fiber is vertically oriented. A gradient of around 10 $^{\circ}\text{C}$ was measured in the creation of the tapered fiber pictured in Figure 60 and Figure 61, measured by staggering two thermocouples in the same glass shielding tube immersed in the etching vessel (measured output in Figure 59).

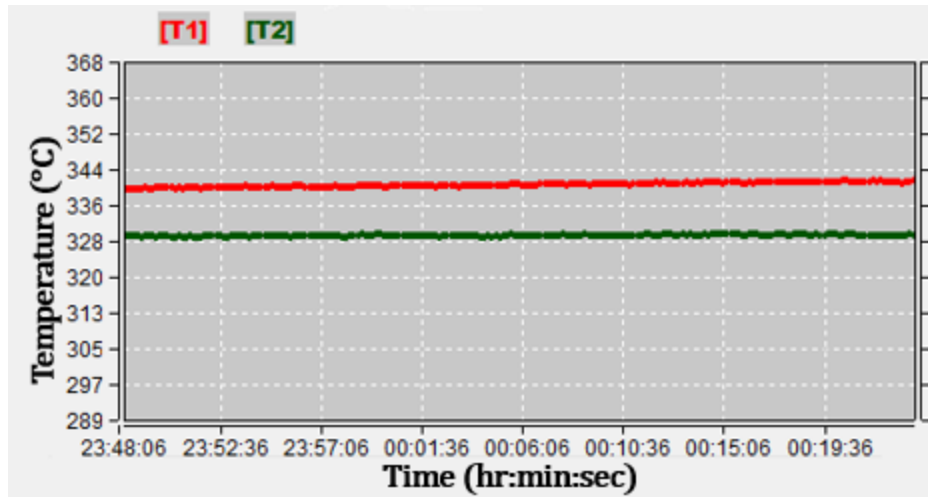


Figure 59: A temperature gradient of around 10°C is induced in the formation of tapered sapphire fibers. T1, red, represents the data recorded by the thermocouple tip located closer to the bottom of the vessel, while T2, green, was located a few centimeters higher.

The base of the taper is visible in Figure 60, while the tip of the fiber is seen in Figure 61, measured to be around 70nm in diameter.

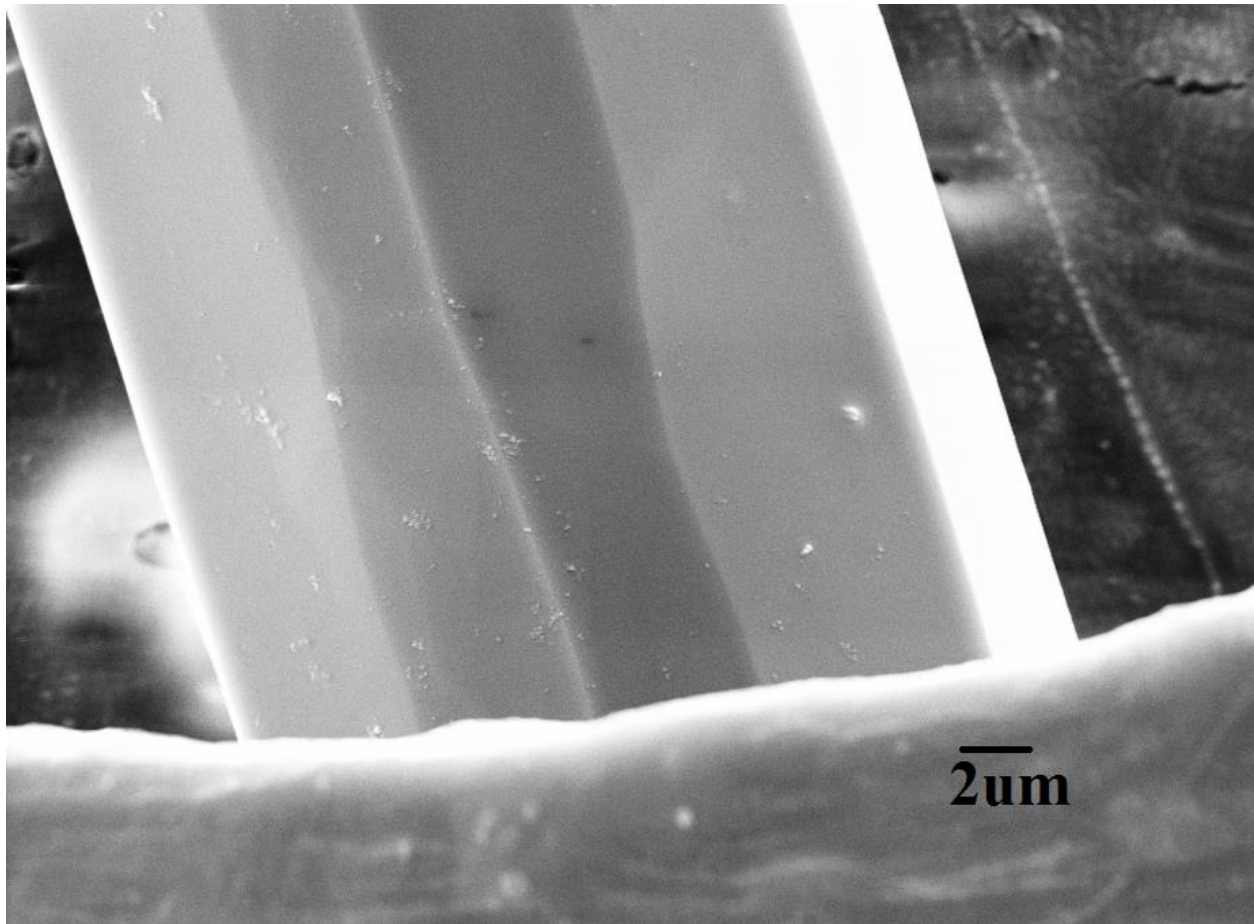


Figure 60: The topmost exposed area of 50µm sapphire fiber was reduced to 25µm through etching.

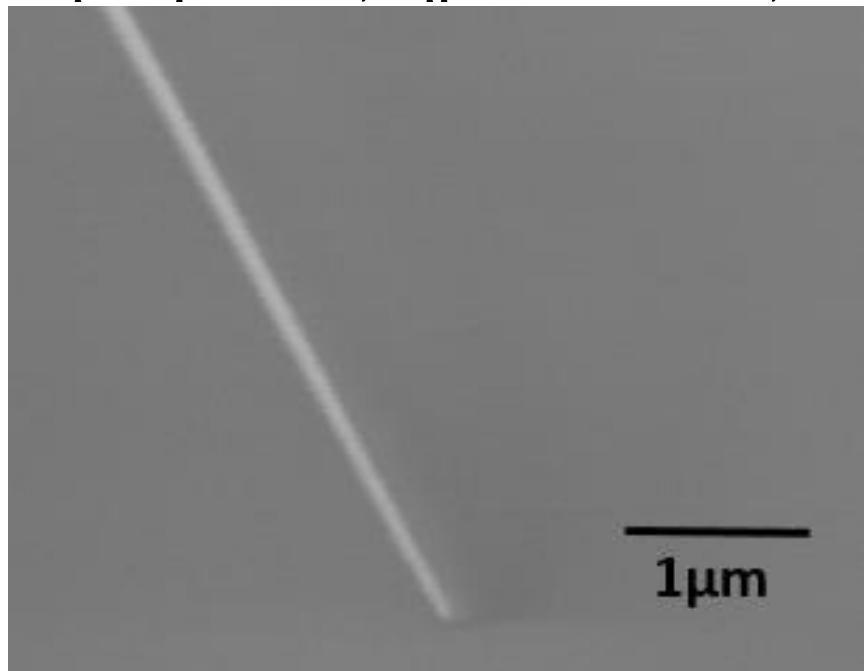


Figure 61: The tip of a tapered sapphire fiber measured around 70nm in diameter.

The surface of these fibers were found to be remarkably smooth and free of deposits or defects, which is vital to proper function as a sensor; only incidental dust is visible on any part of the fiber surfaces. The only non-incidental deposits observed in one sample were globules occurring 5-8 times along the length of the fiber, with three concentrated near the tip of the fiber (Figure 62).

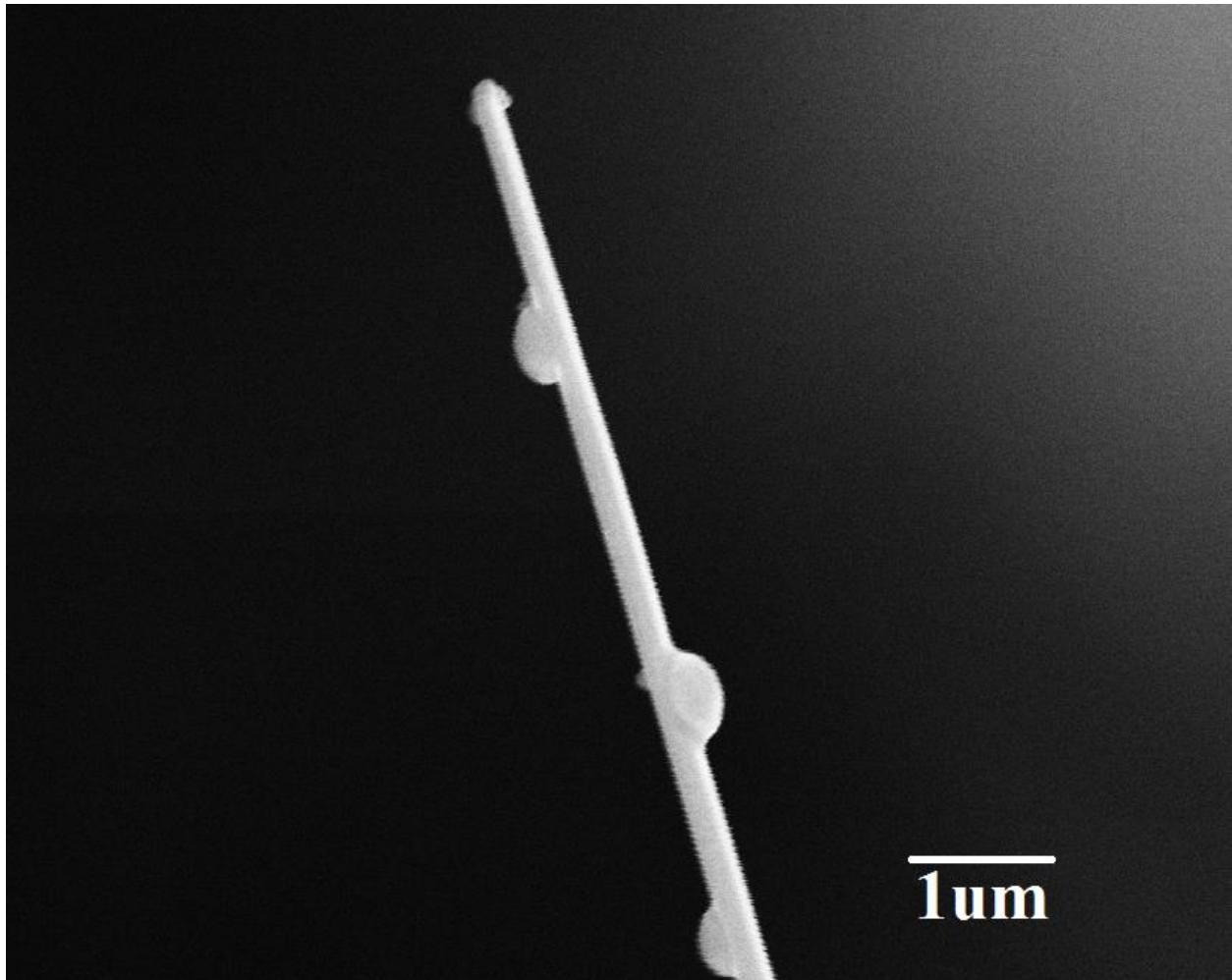


Figure 62: The only deposit or defect visible along the entire length of a submicron-diameter fiber were small globules concentrated near the fiber tip.

EDS was conducted on the globules to determine their composition. One globule in question is shown in Figure 63, measuring a few microns across; the resulting EDS mapping is seen in Figure 64 and Figure 65.

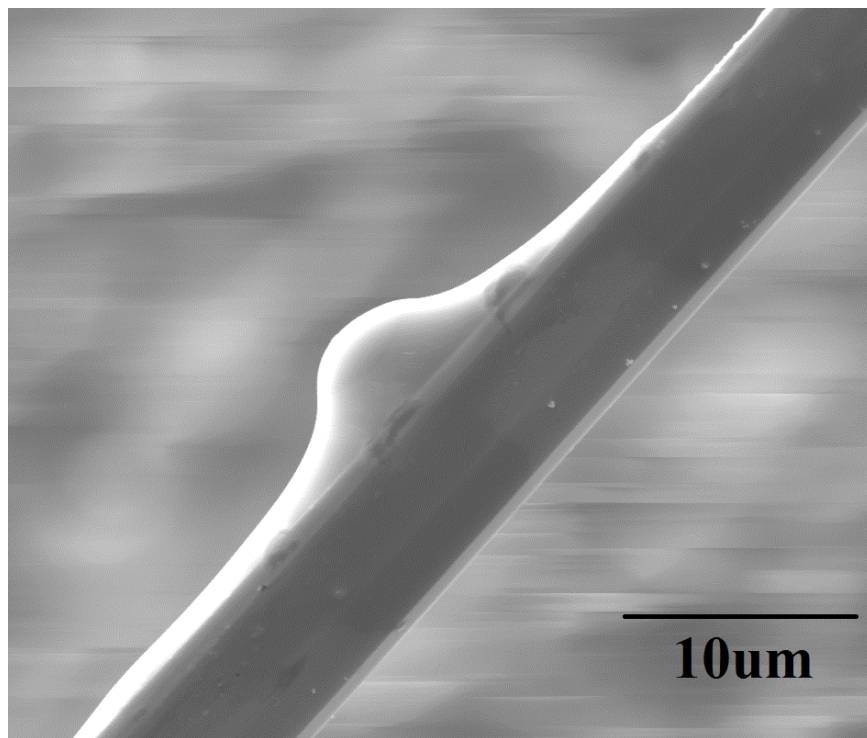


Figure 63: SEM micrograph of globule analyzed using EDS

The only elements detectable in the globule itself were sulfur, phosphorus, and oxygen (aluminum and fluorine were also checked as likely culprits either from the fiber or Teflon) according to the EDS maps in Figure 64 and the spectrum in Figure 66. It can therefore be readily concluded that the globules are simply tiny droplets of the 3:1 $\text{H}_2\text{SO}_4:\text{H}_3\text{PO}_4$ etch solution that survived the rather mild water rinse and are clinging tightly to the fiber under the high vacuum of the SEM chamber.

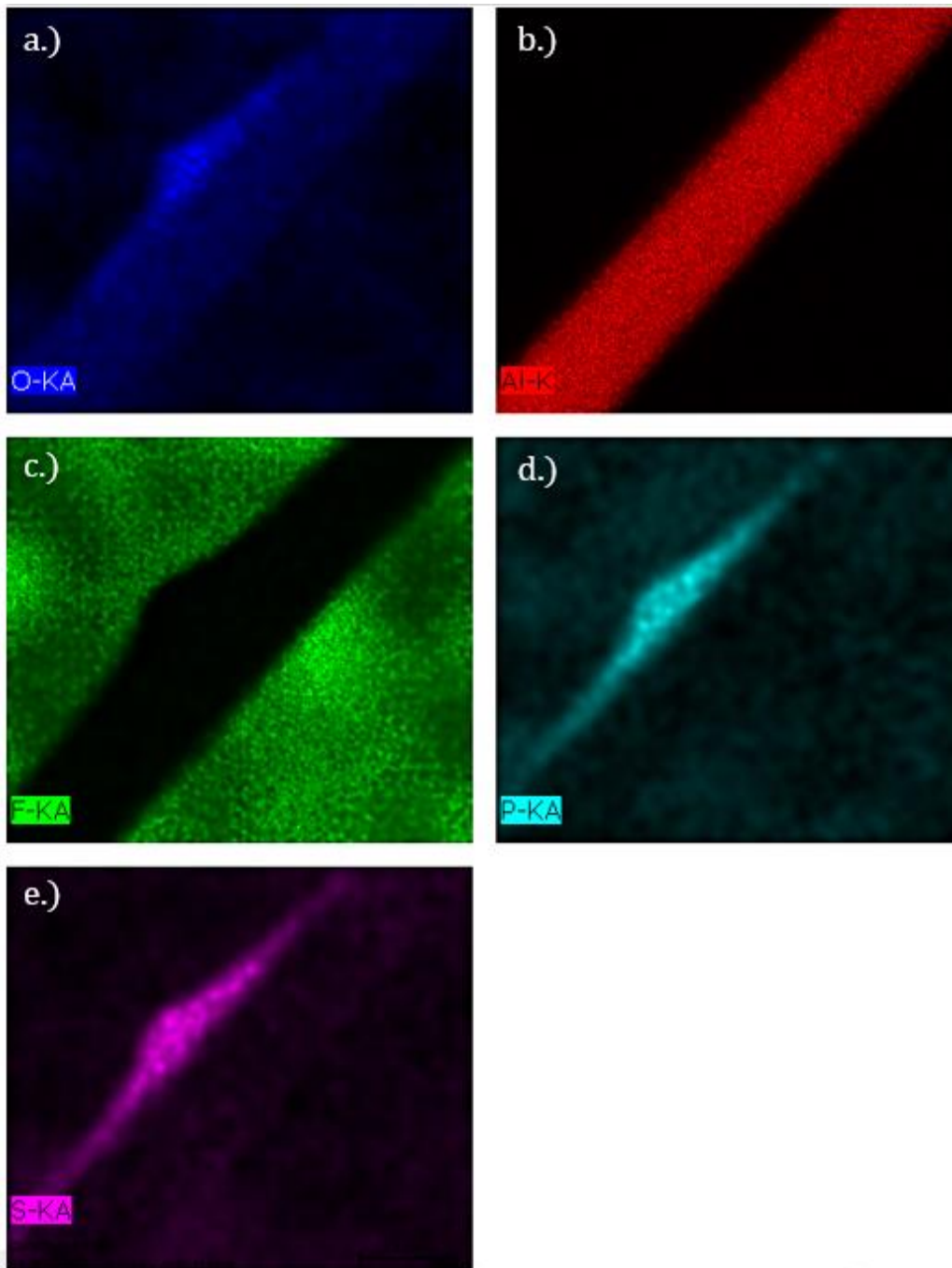


Figure 64: EDS analysis revealed globule to contain a.) oxygen, d.) phosphorous, and e.) sulfur. Other components of potential deposits such as b.) aluminum and c.) fluorine were not detected in the globule.

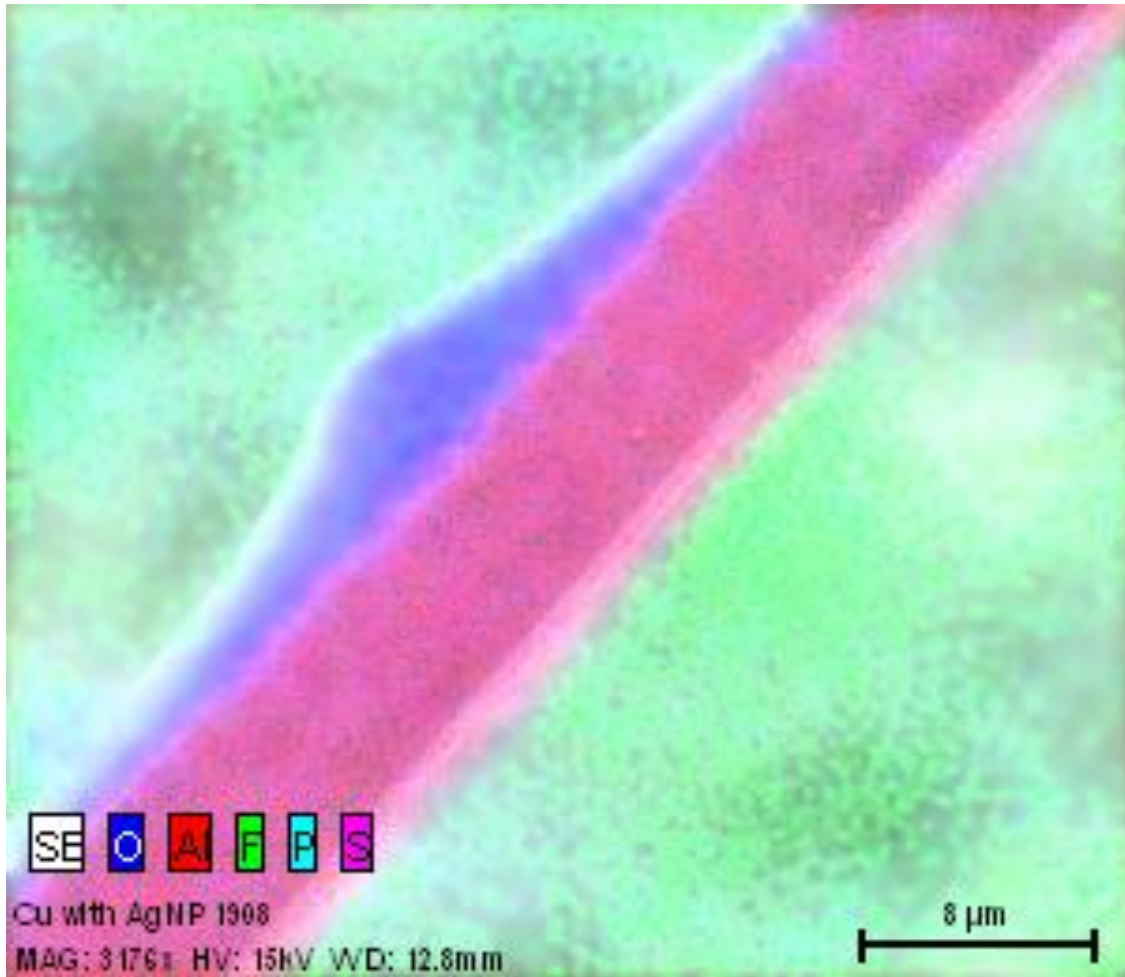


Figure 65: Overlay of EDS analysis highlights the presence of sulfur, phosphorous, and oxygen in the globule adhered to the sapphire fiber.

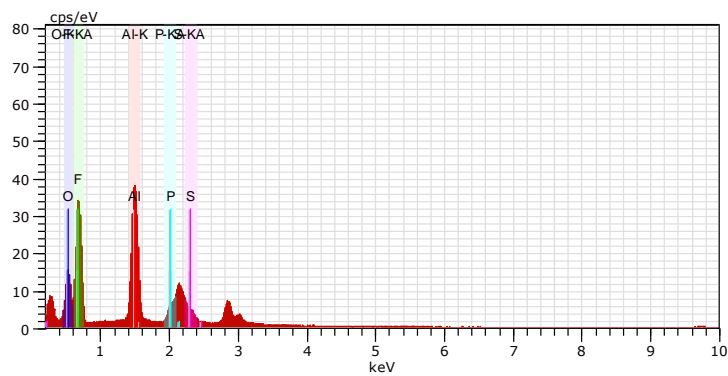


Figure 66: EDS spectrum reveals the only elements present in appreciable quantities are oxygen, fluorine, aluminum, phosphorous, and sulfur. Peaks around 0.3keV, 2.1keV, and 2.8keV are signatures from incidental carbon and the conductive gold/palladium coating.

In Figure 67 a sapphire nanofiber with a tip tapering to a measured diameter of less than 5nm was captured using SEM. The sample was coated with platinum-palladium to reduce charging and increase the apparent smoothness of the coating surface over that of gold-palladium coating (which as used in the sample pictured previously in Figure 61). As the termination of the fiber tip is not precisely visible, it is possible that the fiber tip continues to taper but has become electron transparent (it is suspended cantilever with no background contribution).

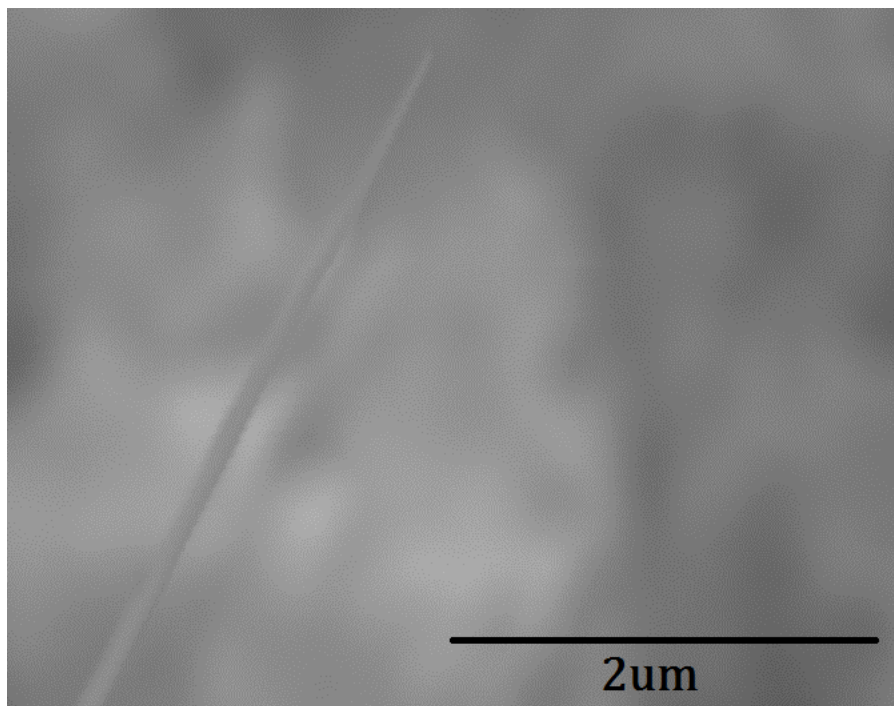


Figure 67. A sapphire nanofiber tapers down to a measured diameter of less than 5nm at its tip

The resiliency of sapphire micro- and nano-fibers is remarkable. The fibers are extremely flexible and able to withstand external manipulation without need for excess caution, as demonstrated by Figure 68, where a sapphire microfiber exhibits a bend radius of less than 10 μ m. A bend of this magnitude would likely cause optical aberrations, but it is useful to note the mechanical resiliency of the fiber for practical purposes, especially in comparison

with silica nanofibers of similar diameter which degrade very quickly simply through interaction with moisture in the air²³.

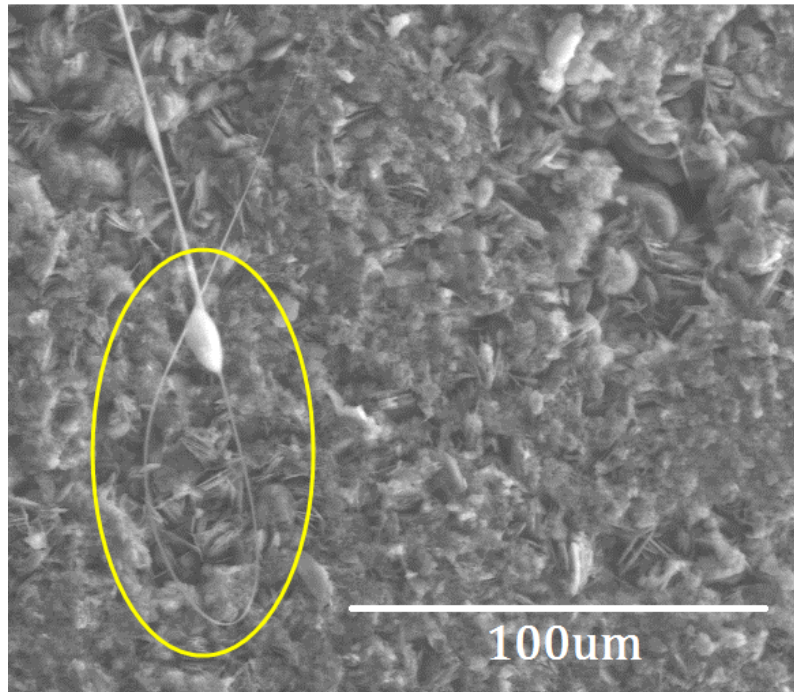


Figure 68. A sapphire microfiber demonstrated a bend radius of less than 10 μ m.

4.3 LMV Sapphire Fiber Analysis

4.3.1 Numerical Aperture of LMV Sapphire Optical Fiber

The effective numerical aperture of the LMV sapphire optical fiber was measured using the method described in Section 3.2.2. The effective NA was determined to be significantly different from the theoretical NA calculated using the refractive indices of core, cladding, and surrounding environment (as could be anticipated since the theoretical NA calculated from refractive indices alone results in a value greater than 1). The numerical aperture was measured using a wavelength of 983nm in overfilled conditions.

Table 5: The measured effective numerical apertures for air-clad sapphire fiber differs greatly from the theoretically-calculated numerical aperture of ~ 1.4 .

Analyzed Fiber	Average Beam Width at $D_1=0\text{mm}$ (μm)	Average Beam Width at $D_2=1\text{mm}$ (μm)	Average Vergence Angle	Average Effective NA	St. Dev.
SMF-28e	3108.61	3335.25	6.49°	0.113	0.029
6.5 μm diameter sapphire	4513.64	4697.16	5.26°	0.090	0.008

The effective refractive index of known SMF-28e was first measured to ensure accuracy of the method; the method used in this testing was very similar to that used to provide the effective NA on the SMF-28e technical datasheet⁶⁷. Corning reports a measured effective NA of 0.14 for its SMF-28e fiber, while the measurements obtained here rendered an average NA of just over 0.11. The error may be attributable to the difference in wavelength used between measurements; Corning's measurement was taken at a wavelength of 1313nm, where SMF-28e is decidedly single-mode, whereas the 983nm wavelength used in this testing is below the designed single-mode cutoff of the SMF-28e fiber. As a result, the observed far-field pattern was not perfectly round (the LP_{11} mode was visible) and Gaussian in its distribution as it would be at higher wavelengths, which likely introduced error.

The 6.25 μm -diameter sapphire fiber demonstrated a more circular far-field projection and Gaussian intensity distribution, so its effective NA measurement of 0.09 may be deemed accurate.

Regardless, the measured effective NA of the air-clad 6.5 μ m-diameter sapphire fiber is drastically less than the value predicted using the theoretical calculations, ~ 1.4 . This observance has an enormous effect on the predicted optical properties of the air-clad 6.5 μ m sapphire optical fiber.

4.3.2 Reduced Laser Pulse Broadening and Modal Dispersion

Reduced laser pulse broadening as a result of reduced modal volume and corresponding modal dispersion was demonstrated for a sapphire fiber whose diameter was reduced from an initial diameter of 125 μ m to an average diameter of $\sim 45\mu$ m with a total length of 1 meter (one end measured a little under 50 μ m, while the other measured a little over 40 μ m). The corresponding improvement of Raman distributed temperature sensing resolution was also calculated from these measurements, all conducted according to the procedure outlined in Section 3.2.3.

The output laser pulse duration of a commercially-obtained 1m-long, 125 μ m-diameter sapphire optical fiber and its reduced-mode 1m-long 45 μ m-diameter counterpart can be determined from Figure 69. The data was normalized to neutralize minor differences in maximum photodetector response across samples so that the peaks could be compared more easily. The measured pulses were also aligned such that their maxima were located at $t=0$ s, also for the purpose of more clearly representing the comparison of pulse duration.

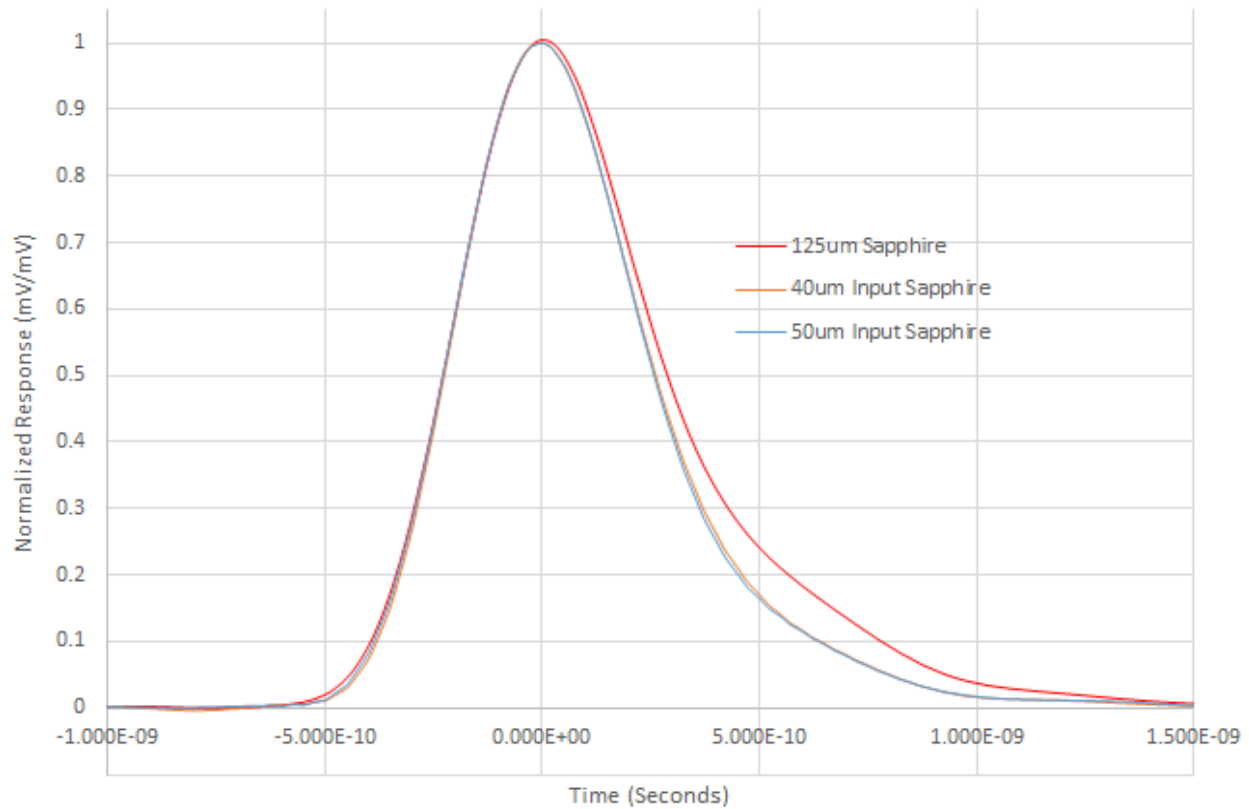


Figure 69: The pulse duration of the reduced-diameter sapphire fiber (~50 μm diameter at one end and ~40 μm at the other) was determined to be less than that of a standard 125 μm sapphire fiber.

The full-width at half-maximum of the Gaussian pulses were measured to yield the duration of each pulse at half its maximum response; the FWHM of the initial laser pulse was subtracted before comparison to eliminate bias from the initial pulse duration. A decrease in pulse duration/modal dispersion of **13.4%** was observed in the laser pulse propagating through the reduced-diameter sapphire fiber versus the standard 125 μm sapphire fiber. Measurements reported in Figure 69 represent the average of 7 data sets collected for each fiber, where each set was itself the average of 64 pulses; the standard deviation of FWHM measurements among data sets was found to be no greater than 2.5 picoseconds (0.5%) for any of the measured fibers.

This pulse duration decrease directly corresponds to an improvement in Raman distributed temperature sensing resolution. An increase in spatial resolution of **13.4%** is calculated based on the pulse duration measurements if a sapphire fiber with a diameter of 40-50 μm is used in lieu of a standard 125 μm sapphire fiber, as determined through the first term of Eq. 38, below. The second term is nullified in these calculations, as this term merely predicts the broadening of the pulse due to the difference in effective NA, which is already accounted for by obtaining actual pulse broadening measurements and inserting them in t of the first term.

$$\Delta L = \frac{ct}{2n} + 2L \left(\frac{1}{\sqrt{1 - \left(\frac{NA}{n}\right)^2}} - 1 \right) \quad \text{Eq. 37}$$

Limitations in equipment capabilities prevented measurement of pulse broadening of SCSF samples that had been reduced to a diameter of 6.5 μm . However, the effect on spatial resolution may be calculated using Eq. 38 and the effective numerical aperture values measured and reported in Table 5.

In these calculations, t in the first term is the FWHM of the original laser pulse, and the second term estimates the increase in pulse duration. Using the manufacturer-provided effective NA of 0.45 for a SCSF with diameter of 125 μm and the measured effective NA of 0.09 for the etched 6.5 μm -diameter SCSF, spatial resolution is predicted to decrease from 7cm to 0.5cm for a SCSF measuring 1 meter in length, representing an improvement of **93%**.

4.3.3 LMV Sapphire Optical Fiber Measurements

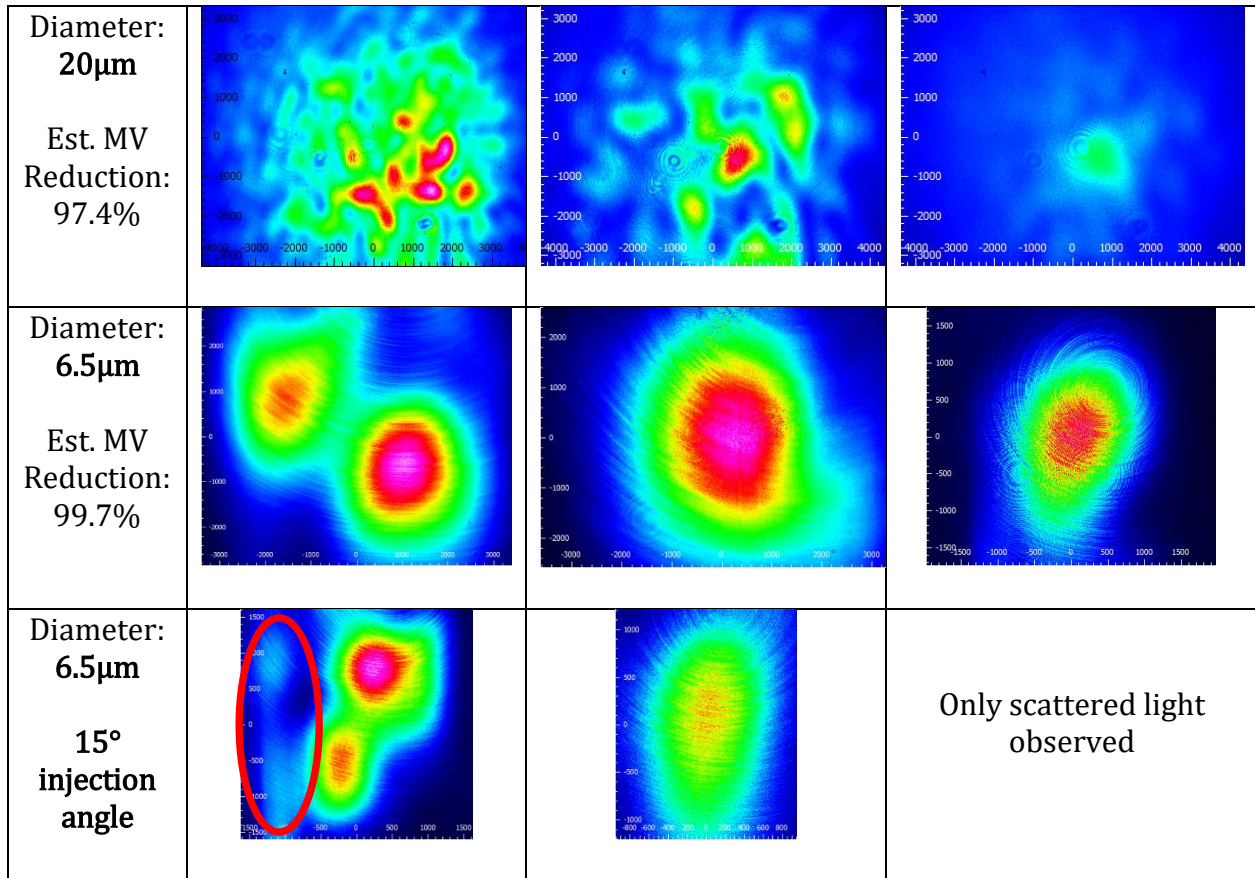
Subsequent to the production of LMV sapphire fiber according to the procedure outlined in Section 3.1.2, modal volume measurements were taken in the manner described in Section 3.2.1.

Low-order LP_{01} and LP_{11} modes in an air-clad single-crystal sapphire optical fiber at typical operation wavelengths were observed for the first time without any type of modal manipulation (such as phase masking or selective mode excitation, which artificially isolate preferred modes for propagation while other modes are still supported by the fiber^{58,59}). The observed modal projections were verified using several input sources and injection angles and were deemed to be stable.

A range of data collected from sapphire fiber samples etched to decreasing diameters is presented in Table 6. As hypothesized, the far-field projections changed in a predictable manner as diameter decreased; the density of individual intensity peaks (“speckles”) decreased with decreasing diameter while the individual peaks broadened corresponding to decreased modal volume and therefore decreased modal interference. The concentric ripple pattern visible in projections from smaller fiber diameters is caused by the interference of scattered light off the front and back surfaces of the glass detector cover, a phenomenon also observed by other researchers⁹⁴.

Table 6: Far-field patterns demonstrated reduced modal interference as fiber diameter was decreased, ultimately resulting in the appearance of LP₀₁ and LP₁₁ modes. The area circled in red in one of the images is incident light from elsewhere in the room during testing.

	Far-field Intensity Projections and Estimated Modal Volume		
	$\lambda=532\text{nm}$	$\lambda=783\text{nm}$	$\lambda=983\text{nm}$
Diameter: 125μm			
Diameter: 77μm Est. MV Reduction: 55.4%			
Diameter: 66μm Est. MV Reduction: 72.1%			
Diameter: 58μm Est. MV Reduction: 88.5%			
Diameter: 35μm Est. MV Reduction: 92.2%			



At the lowest fiber diameter analyzed (6.5 μ m), a low-order LP₁₁ mode is visible at a wavelength of 532nm, and the fundamental LP₀₁ mode is observed at wavelengths of 783nm and 983nm, representing the first known observance of the fundamental mode in a far-field projection from an air-clad sapphire optical fiber.

The injection angle of the laser light was altered by 15° (setup pictured in Figure 70, data in bottom row of Table 6) to confirm the stability of the observed LP₀₁ and LP₁₁ modes. Low-order modes would not be much affected by such a change because of their inherently high core confinement, but the intensity patterns would be significantly affected if the observed far-field projections were attributable to other sources, such as a coincidental superposition of other higher order modes (which propagate a higher percentage of power

near the cladding and would not be excited by angled input conditions). However, the far-field projections displayed near-identical behavior, confirming the observance of a low-order LP₁₁ mode at a wavelength of 532nm and the fundamental LP₀₁ mode at 783nm.

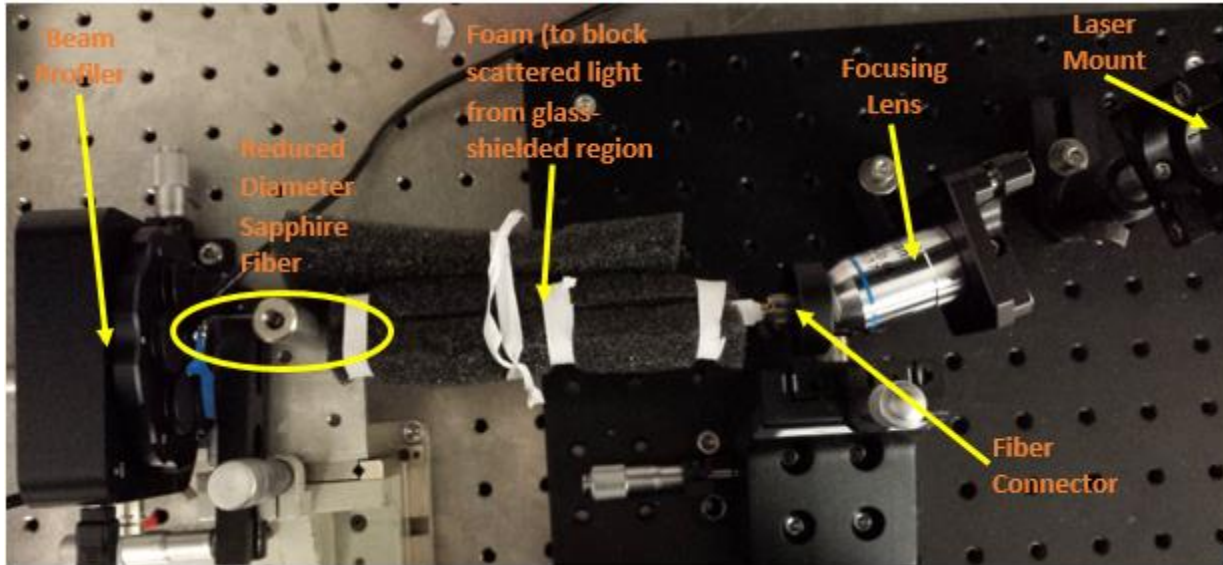


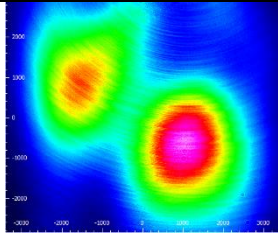
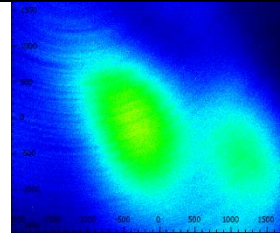
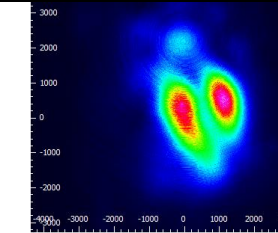
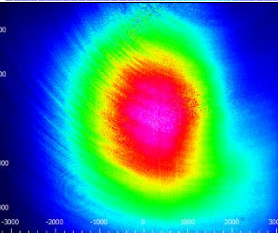
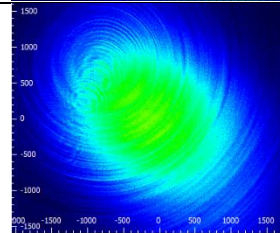
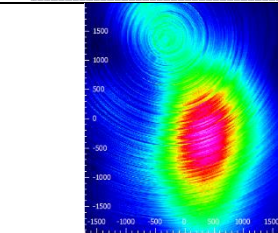
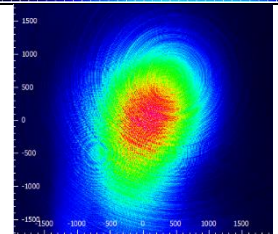
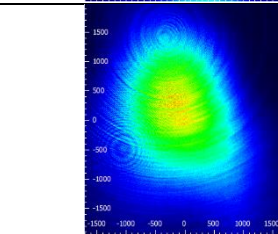
Figure 70: The conclusion that LP₀₁ and LP₁₁ modes were observed was supported by altering the injection angle of the laser light and observing the far-field patterns. The etched sapphire fiber with its tip diameter of 6.5 μ m is circled, though of course it is too small to be visible in the image. The polished tip of the fiber is inserted into a foil aperture in front of the beam profiler detector.

Injection conditions into the sapphire optical fiber with a tip diameter of 6.5 μ m were further altered to verify the stability of the low-order modes that were observed using direct free-space coupling of the laser. The same 6.5 μ m-diameter sapphire fiber yielding the Table 6 results was butt-coupled to other FC/PC-connected multimode (50/125 μ m step index) and single-mode (SMF-28e) fibers, which were then free-space coupled to the laser source.

The results are visible in Table 7. The mode profile remained largely unchanged regardless of input condition, with the same LP₀₁ and LP₁₁ modes appearing. The relatively low light

intensity inherent to small-core SMF results in a lower overall intensity in all patterns and prevents imaging of a clear pattern of any type at 983nm.

Table 7: Far-field patterns of the sapphire optical fiber with etched diameter of 6.5 μ m were largely similar regardless of whether light was input using direct free-space coupling or butt-coupled with SMF-28e or 50/125 step-index MMF patch cables.

Wavelength	Input: Direct	Input: SMF	Input: MMF
532nm			
783nm			
983nm		Intensity too low to distinguish from scattered light	

All tested input conditions yield similar results; the LP₀₁ and LP₁₁ modes appear in the far field projections of the 6.5 μ m-diameter sapphire optical fiber at the tested wavelengths regardless of all tested input conditions.

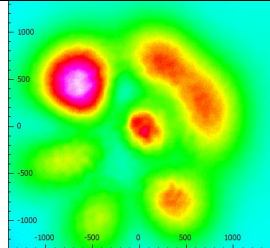
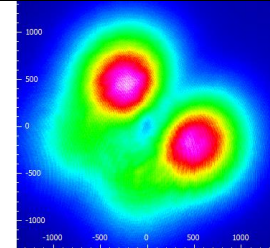
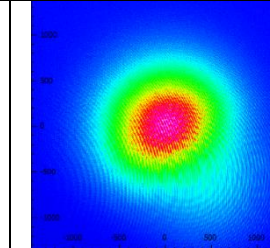
4.3.4 Mode Propagation Stability

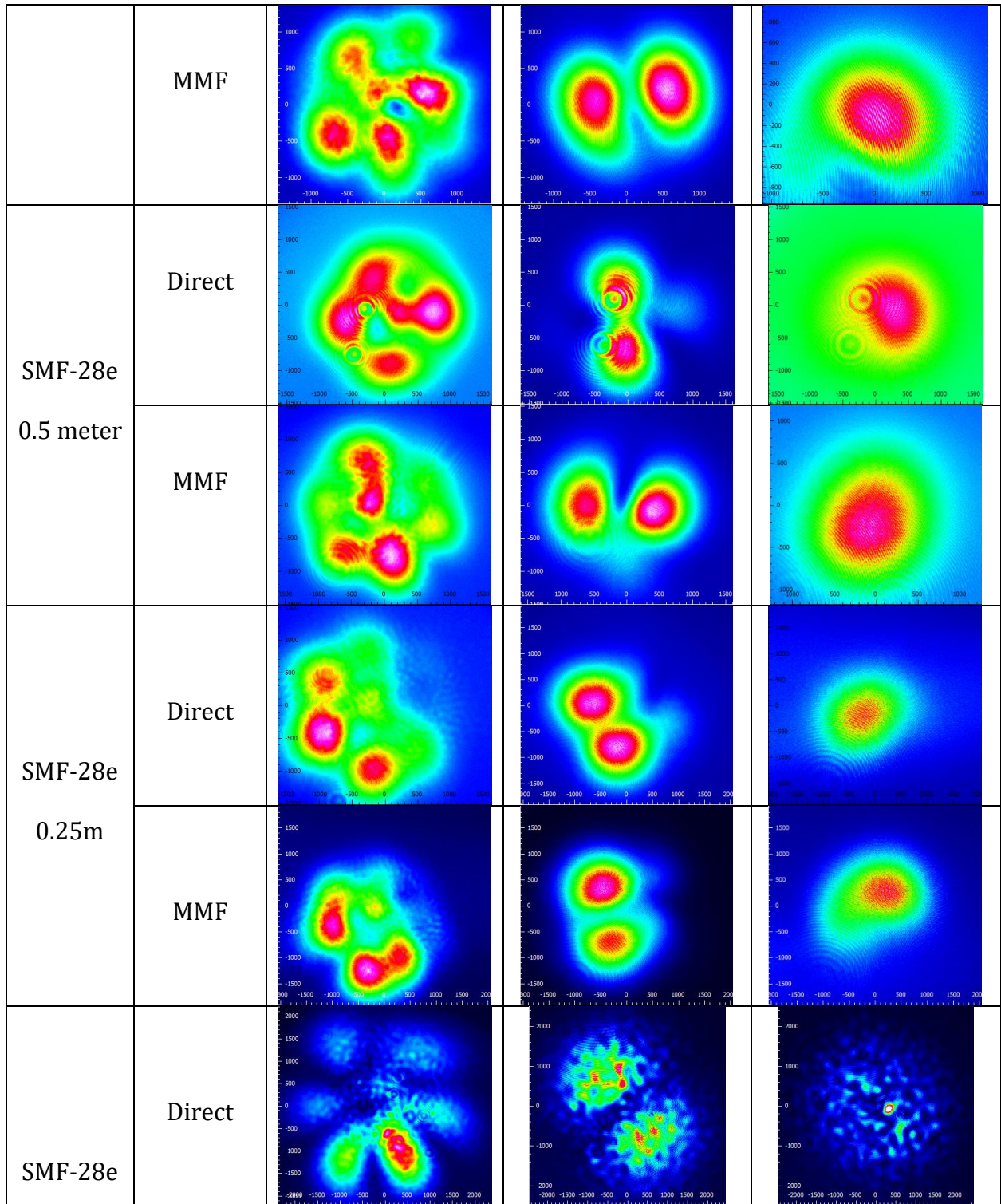
It is also of value to determine the general stability of propagating modes with regard to fiber length, as it could be anticipated that some length is required to reach equilibrium once the light has propagated beyond the input method (in this case, the 125 μ m-diameter glass-shielded region of sapphire fiber).

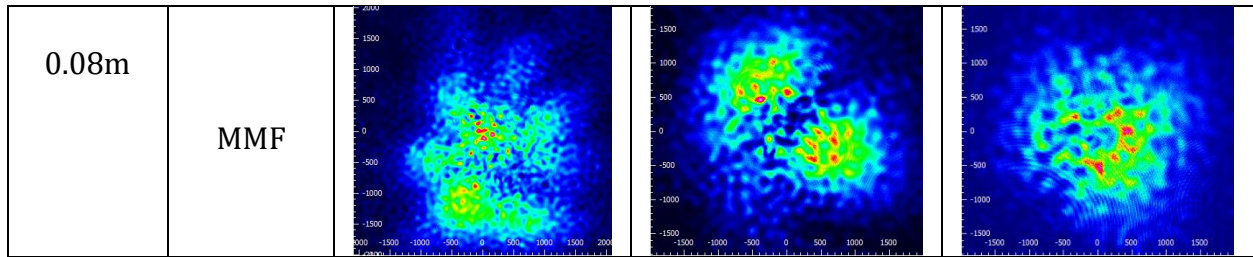
To help eliminate additional factors contributing to variation in the determination of the effect of fiber length on far-field projection stability, commercially-available single mode (SMF-28e) and multimode (50/125 μm step-index MMF) fibers were used in this analysis rather than any custom-built sapphire samples. SMF or MMF fibers of 1m, 0.5m, 0.25m, and 8cm were tested with the same lasers utilized in previous testing. Light was transmitted to these samples using either direct free-space coupling or butt-coupling of a patch cable of the opposite variety. The length of the MMF patch cable was 2.5m, while the length of the SMF patch cable was 1m, and laser light was injected into these patch cables using direct free-space coupling when it was supplying light to the other fiber during testing.

The far-field projections emanating from varying lengths of SMF-28e at three different wavelengths and two injection methods is shown in Table 8 below. Note that higher-order LP_{31} and LP_{11} modes are supported at wavelengths of 532nm and 783nm by this nominally “single-mode” fiber because it is designed to support only one mode at longer wavelengths (listed as $>1313\text{nm}$ ⁶⁷) than those used in this experiment.

Table 8: Far-field patterns captured from different lengths of SMF-28 were largely consistent for a given test wavelength regardless of fiber length or input condition. Interference (likely from unstripped cladding modes) was apparent at short lengths.

Test Fiber	Input Condition	$\lambda=532\text{nm}$	$\lambda=783\text{nm}$	$\lambda=983\text{nm}$
SMF-28e 1 meter	Direct			

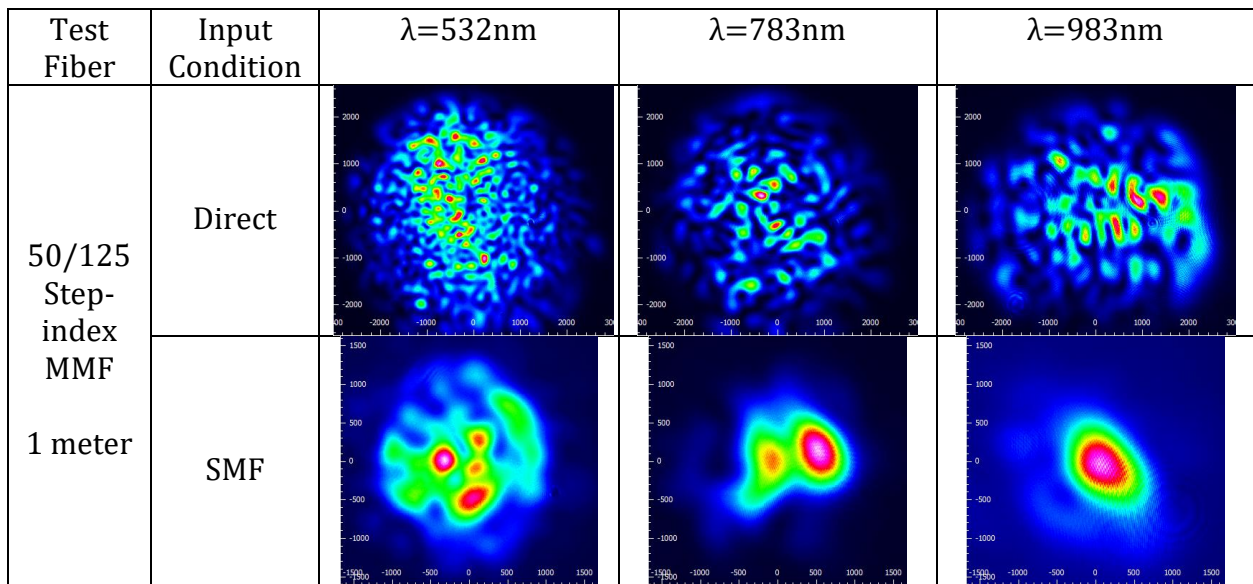


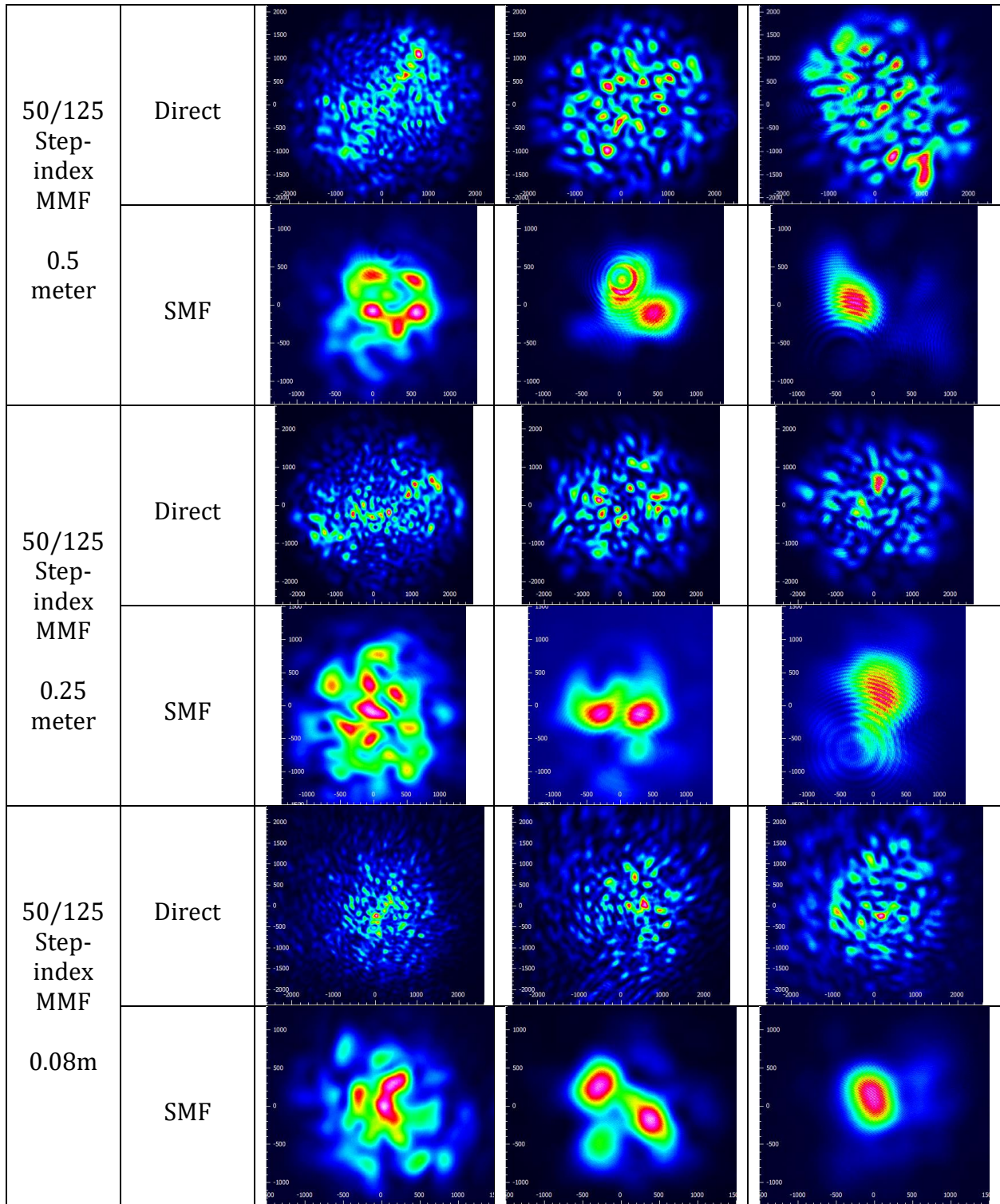


Regardless of input condition or fiber length, the same low-order modes were dominant for a given wavelength, with the LP₃₁ mode most prominent at 532nm and LP₁₁ and LP₀₁ modes visible at 783nm and 983nm, respectively. Speckled interference patterns were visible once the SMF length reaches 8cm (and also at 0.25m to the discerning eye), though the same mode patterns are apparent; this is likely due to interference from unstripped cladding modes.

A duplicate experiment was carried out using 50/125μm step-index MMF, with input conditions varying between direct free-space coupling and SMF input (Table 9).

Table 9: Far-field patterns were also consistent for various lengths of 50/125 step index MMF for a given test wavelength. The input method did significantly affect the observed far-field projections for MMF, unlike tested SMF or sapphire samples.

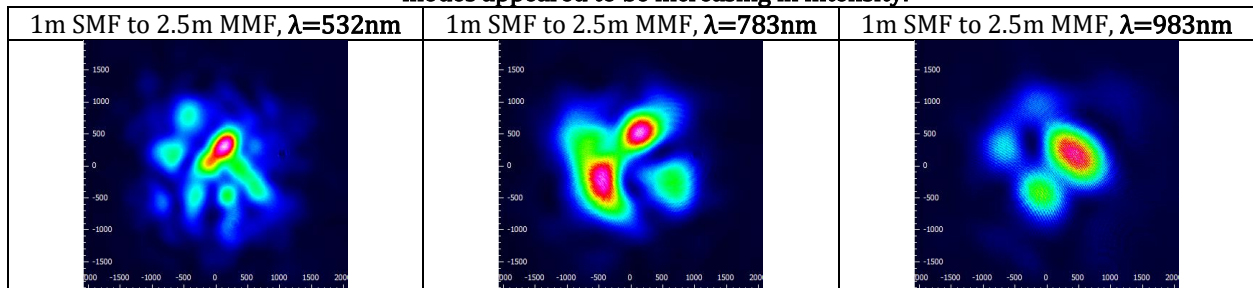




The length of the MMF had little effect on the observed far-field profile, as was seen in testing of the SMF. The SMF input did not directly excite the higher order modes supported

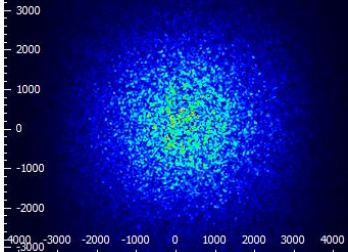
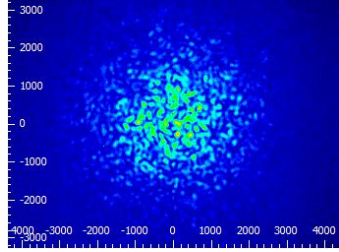
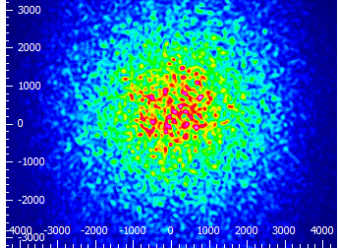
by the MMF, so LP₃₁, LP₁₁, and LP₀₁ intensity profiles remain dominant with some light leaking into other modes over the length of the MMF fiber to produce a background interference pattern. A full-length 2.5m MMF patch cable was also tested to determine whether this trend would continue (Table 10), and it appears that power coupled into higher-order modes does begin to increase with length as expected, but the threshold for obvious changes in power occur well beyond the previously-tested 1m length of MMF.

Table 10: Lower-order modes from a SMF input into 2.5m length of MMF were still apparent, but higher-order modes appeared to be increasing in intensity.



Interestingly, while use of SMF to provide input light into MMF results in significant observable power coupled into low-order modes at MMF lengths beyond 1 meter, this does not appear to be the case for sapphire fiber. A 125 μm -diameter sapphire fiber sample such as that tested previously in Table 6 was analyzed using the same variations on input conditions, but the only discernible effect on far-field projections was relative intensity (Table 11), largely due to the differences in core size; the core diameter of the SMF is 8.2 μm and that of the MMF is 50 μm ; the beam spot size of the direct free-space coupling method is around 500 μm , far larger than the 125 μm sapphire core.

Table 11: The input condition affected intensity of far-field projections of 125 μm -diameter sapphire fiber at a wavelength of 532nm but did not drastically affect the modal interference pattern.

Direct input to 125 μm diameter sapphire fiber, $\lambda=532\text{nm}$	SMF input to 125 μm diameter sapphire fiber, $\lambda=532\text{nm}$	MMF input to 125 μm diameter sapphire fiber, $\lambda=532\text{nm}$
		

4.3.5 Discussion of Observed Results in Comparison with Theoretical Models

While a quantifiable modal volume analysis method would be ideal, the demonstrated qualitative comparative far-field analysis method does yield repeatable results that accurately represent the true beam profile present in an optical fiber in typical conditions. In the case of the 6.5 μm -diameter sapphire fiber, low-order LP₀₁ and LP₁₁ modes are observed in the tested wavelength range of 532-983nm (the fundamental mode appears at wavelengths of 783nm and above).

Mathematical modal volume predictions presented in Section 2.1.2 estimated the support of 460-1600 modes at this air-clad sapphire diameter of 6.5 μm (corresponding to minimum and maximum wavelengths of 532nm and 983nm) using the theoretically-calculated numerical aperture for air-clad sapphire which is dependent solely on the refractive indices of sapphire and air. It is therefore reasonable to question why the LP₀₁ and LP₁₁ modes were observed in far-field patterns when hundreds of other modes should still have been supported according to the models in Section 2.1 using the theoretical NA (and therefore producing the familiar interference patterns seen at larger diameters).

It is well documented¹¹ that the measured effective numerical aperture of an optical fiber (especially sapphire⁶⁴) can differ greatly from the theoretically-calculated NA. Factors beyond refractive index can affect the effective NA, such as cross-sectional fiber geometry (sapphire fibers are not circular due to their hexagonal crystal structure), as well as the fact that the complex refractive index is not determined in these calculations, which would account for effects such as attenuation (Section 2.2). Therefore, this apparent deviation from theoretically anticipated results may be remedied through application of the measured effective NA for the reduced-diameter sapphire fiber providing the LP₀₁ and LP₁₁ mode projections seen in Table 6.

If the measured effective NA of the 6.5 μ m-diameter air-clad sapphire fiber (0.09, Table 5) is substituted for the theoretical NA calculated using the refractive indices of sapphire and air, perfect harmony between the theoretical models and observed modal behavior is observed. Modal volume estimations using the air-clad sapphire theoretical NA of ~ 1.4 predict the support of 1614, 736, and 461 modes at the respective tested wavelengths of 532nm, 783nm, and 983nm. Use of the measured effective NA of 0.09 for the 6.5 μ m sapphire fiber instead anticipates support of only the fundamental LP₀₁ mode at wavelengths greater than ~ 760 nm. The greater predictive power of using a measured effective NA rather than the inaccurate theoretical NA is highlighted in Figure 71. Inserting the correct NA into the modal volume estimation procedure described in Section 2.1.2 produces results that support the observed far-field patterns.

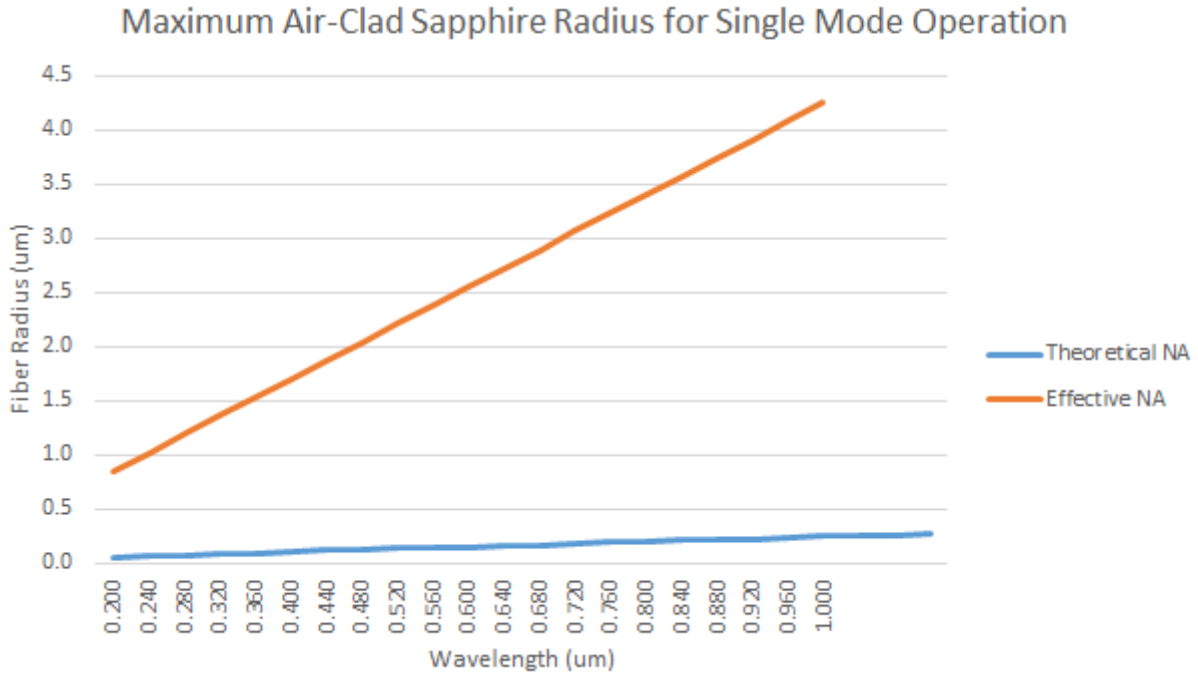


Figure 71: Use of the measured effective NA produces predictions that are perfectly in line with observed single-mode cutoff diameter and wavelength, contrasting predictions using the theoretical NA.

Furthermore, use of the precise modal volume calculations derived in Section 2.1.1 also predicts the support of only a single mode at wavelengths of 783nm and 983nm if the measured effective NA of the air-clad 6.5 μm -diameter sapphire fiber (0.09) is substituted for the theoretical NA (~ 1.4). The solution of the modal-volume-indicating characteristic equation for this device at $\lambda=783\text{nm}$ and $\lambda=983\text{nm}$ is pictured in Figure 72.

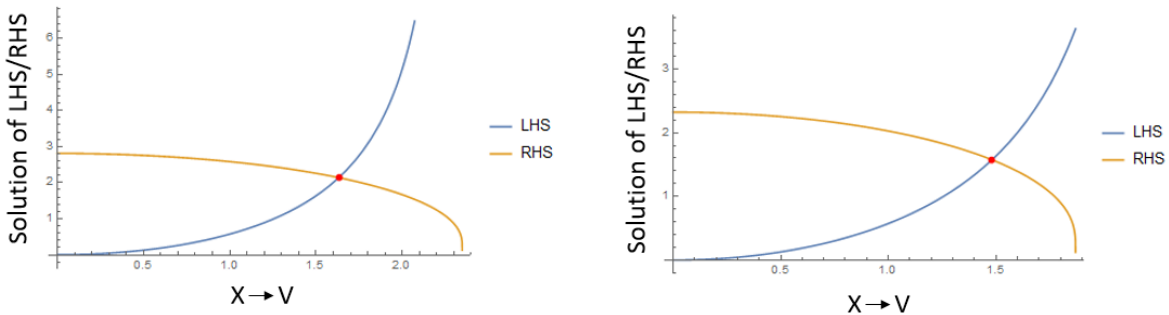


Figure 72: Use of precise modal volume calculation methods also indicates a single mode is supported for an air-clad 6.5 μm -diameter sapphire fiber with an effective NA of 0.09 at $\lambda=783\text{nm}$ (left) and $\lambda=983$ (right).

This is an extremely valuable discovery that is of imperative immediate importance in high-temperature sensing applications; a sapphire fiber measuring several microns in diameter is much more easily handled, protected, and deployed than submicron-diameter fibers that were originally predicted to be necessary for single mode behavior using the much larger theoretical numerical aperture. Furthermore, the predictive power of the models described at length in Section 2 are greatly bolstered by the observing the effect of utilization of the effective versus theoretical NA values; this point is magnified by the comparison displayed in Figure 71. It may now be stated with confidence that the first single-mode air-clad sapphire optical fiber has been demonstrated at diameters that are still useful for carrying of large amounts of optical power and inscription of features such as intrinsic Bragg gratings, not to mention much greater practical resiliency than submicron-diameter sapphire fibers.

Additionally, it was demonstrated that these low-order mode profiles were stable with a reduced-diameter sapphire fiber length of only 10cm and in a wide range of injection conditions, proving that sensing schemes requiring the reduced modal dispersion and consistent radial intensities provided by single-mode sapphire optical fibers are now within reach.

5 CONCLUSIONS

In this research, the only known method for reliably and consistently reducing the diameter of single-crystal sapphire below the 50 μ m limit of commercial fabrication techniques was thoroughly explored, developed, and demonstrated. The practical nuances of procuring optical-quality sapphire fibers for enhanced extreme-environment sensors and data transmitters were discussed, and in-depth analysis of the etching behavior of sulfuric and phosphoric acid and their 3:1 mixture with a-plane sapphire was presented for the first time. Further experimentation with the etching solutions revealed surprising and complex compositional characteristics in the phosphoric acid throughout the etching process, and the knowledge gained from these experiments was used to discern the cause behind differences in etching rates of a-plane and c-plane sapphire surfaces.

Sapphire fiber with a diameter less than the wavelength of visible light was produced for the first time. A method for tapering the fiber to induce additional optical advantages was also developed and demonstrated.

Testing of the effective numerical aperture of LMV sapphire optical fiber revealed a large disparity between the effective NA and theoretically-calculated NA. Use of the effective NA rather than the inaccurate theoretical NA was deemed to have a great effect on predicted optical properties of LMV sapphire fiber devices; use of the effective NA in predictive modal volume estimates demonstrated perfect agreement with observed results, contrasting the predictions made using the theoretically-calculated NA for LMV sapphire optical fiber.

The decreased laser pulse duration corresponding to decreased modal dispersion in a reduced-diameter sapphire fiber was also determined, providing a direct increase in the sensing resolution of Raman distributed temperature sensing methods.

A single-mode air-clad single-crystal sapphire optical fiber was demonstrated for the first time. The single-mode cutoff wavelength and diameter for the air-clad sapphire system was also determined, providing crucial information for future design of extreme environment sensors relying on reduced modal volume. Variations of input conditions and other potential factors were thoroughly explored to demonstrate the stability of the observed far-field projections.

Theoretical models to be used in the design of LMV sapphire fiber devices were also developed, specifically to more accurately predict modal volume and core confinement. These theoretical design tools, combined with the developed capability to produce sapphire optical fibers of any desired diameter, provide the foundation for a new class of extreme environment sensor materials based on the LMV sapphire platform. Observance of low-order LP₀₁ and LP₁₁ modes in micron-diameter sapphire fiber indicates sensing schemes requiring low modal volume can now be used in sapphire with stronger signal than could be transmitted through subwavelength-diameter cores.

The new contributions to the body of literature in this field of sapphire fiber optics are summarized as follows:

- The only known procedure for reducing the diameter of single-crystal sapphire optical fiber below that of standard fabrication limits (<50 μ m)

- Optimization of the parameters associated with this wet-acid etching procedure to predictably produce LMV sapphire fibers with optic-quality surfaces
- Demonstration of heating profiles that produce tapered sapphire optical fibers
- Presentation of the first air-clad single mode sapphire optical fiber
 - Single mode behavior demonstrated at wavelengths of 783nm and 983nm, and low-order LP₁₁ mode observed at a wavelength of 532nm
 - Determination of the single-mode cutoff for air-clad sapphire with respect to diameter and wavelength
- Demonstration that established optical fiber equations regarding modal volume prediction that are based on weakly-guiding assumptions are accurate for the high- Δ air-clad sapphire system if the effective NA is measured and utilized instead of theoretical NA
 - The first measurement of effective numerical aperture for a single-mode sapphire optical fiber
- Measurement of reduced laser pulse broadening corresponding to reduced modal dispersion in a reduced-mode sapphire optical fiber
 - Extrapolation of increased resolution in a Raman distributed sensing system as a result of decreased modal dispersion
- Enhanced understanding of the chemistry involved in the etching of sapphire using sulfuric and phosphoric acids and their 3:1 mixture
 - The first reporting of etch rates and activation energies of a-plane sapphire

- Discussion and experimental support for factors contributing to differences in etch rates of a-plane and c-plane sapphire surfaces
- Enhanced understanding of morphological transformations in sulfuric and phosphoric acids at elevated temperatures, including their interactions with one another

6 FUTURE WORK

This research has proved to be foundational in nature, enabling the first production of a whole new class of sensor materials (LMV and SDF sapphire devices). There is enormous opportunity to capitalize on the knowledge gained throughout this study and continue to develop exciting new technologies. Here are but a few of the research opportunities immediately enabled by the foundation laid in this document:

- Increased resolution of high-temperature distributed sensing techniques using LMV sapphire fiber
- Sensing techniques using intrinsic (or extrinsic) fiber Bragg gratings (FBG's) in LMV sapphire fiber
- Evanescent field-based sensing using sapphire SDF's
- Selective masking and etching studies to produce unique cross-sectional geometries in sapphire optical fiber
- Exploration of exotic applications of SDF and near-SDF sapphire fiber, such as supercontinuum generation and microring resonators
- Biomedical applications such as microstrain sensors and non-invasive soft tissue probes

REFERENCES

- 1 Levin, I. & Brandon, D. Metastable Alumina Polymorphs: Crystal Structures and Transition Sequences. *J. Am. Ceram. Soc* **81**, 1995-2012 (1998).
- 2 Stabel, J. M. Diamond dust for laps and sapphires for cutting tools. *American Machinist* (1904).
- 3 Parks, C. S. & Kelley, K. K. The heat capacities of some metallic oxides. *Journal of Physical Chemistry* **30**, 47-55 (1926).
- 4 Feigelson, R. S., Kway, W. L. & Route, R. K. Single crystal fibers by the laser-heated pedestal growth method. *Optical Engineering* **24**, 1102-1107 (1985).
- 5 Dils, R. R. High temperature optical fiber thermometer. *Journal of Applied Physics* **54** (1983).
- 6 Rensberger, R. High Temperature Optical Fiber Thermometer: New instrument measures temperatures to 2000C. *National Bureau of Standards* **TN-5387** (1983).
- 7 Tichenor, D. A., Hencken, K. R. & Bickes, R. W. Sapphire Fiber Optic Temperature Probe. *NTIS* **N87-21170** (1986).
- 8 Edl-Mizaikoff, B., Goetz, R. & Kellner, R. A. IR fiber optic evanescent field sensors for gas monitoring. *Proceedings of SPIE- The International Society for Optical Engineering* **2508**, 253-264 (1995).
- 9 Pickrell, G. & Wang, A. Single-Crystal Sapphire Optical Fiber Sensor Instrumentation. (Center for Photonics Technology, Bradley Department of Electrical Engineering, Virginia Tech, 2009).
- 10 Merberg, G. N. & Harrington, J. A. Optical and mechanical properties of single-crystal sapphire optical fibers. *Applied Optics* **32**, 3201-3209 (1993).
- 11 Nubling, R. K. & Harrington, J. A. Optical properties of single-crystal sapphire optical fibers. *Applied Optics* **36**, 5934 (1997).
- 12 Grobncic, D., Mihailov, S. J., Ding, H., Bilodeau, F. & Smelser, C. W. Single and low order mode interrogation of a multimode sapphire fibre Bragg grating sensor with tapered fibres. *Meas. Sci. Technol* **17**, 980-984 (2006).
- 13 Pickrell, G., Homa, D. & Wang, A. *Reduced Mode Sapphire Waveguide and Distributed Sensing System* (Virginia Polytechnic Institute and State University, 2013).
- 14 Gupta, B. D. & Singh, C. D. Evanescent-absorption coefficient for diffuse source illumination: uniform- and tapered-fiber sensors. *Applied Optics* **33**, 2737-2742 (1994).
- 15 Zaatar, Y. *et al.* Fabrication and characterization of an evanescent wave fiber optic sensor for air pollution control. *Materials Science and Engineering: B* **74**, 296-298 (2000).
- 16 Brambilla, G., Finazzi, V. & Richardson, D. J. Ultra-low-loss optical fiber nanotapers. *Optics Express* **12**, 2258-2264 (2004).
- 17 Lacroix, S., Bourbonnais, R., Gonthier, F. & Bures, J. Tapered monomode optical fibers: understanding large power transfer. *Applied Optics* **25**, 4421-4425 (1986).
- 18 Tong, L. *et al.* Subwavelength-diameter silica wires for low-loss optical wave guiding. *Nature* **426**, 816-819 (2003).
- 19 Ghosh, J. B. a. R. Power density of the evanescent field in the vicinity of a tapered fiber. *J. Opt. Soc. Am. A* **16**, 1992-1996 (1999).
- 20 Ding, B., Wang, M., Yu, J. & Sun, G. Gas Sensors Based on Electrospun Nanofibers. *Sensors* **9**, 1609-1624 (2009).

- 21 Lou, J., Tong, L. & Ye, Z. Modeling of silica nanowires for optical sensing. *Optics Express* **13** (2005).
- 22 Tan, W., Shi, Z.-Y. & Kopelman, R. Development of Submicron Chemical Fiber Optic Sensors. *Anal. Chem.* **64**, 2985-2990 (1992).
- 23 Xiao, L., Grogan, M. D. W., England, R., Wadsworth, W. J. & Birks, T. A. Gas Sensing with a Sub-Micron Tapered Fibre Embedded in Hydrophobic Aerogel. *IEEE* (2010).
- 24 Lacroix, S., Black, R. J., Veilleux, C. & Lapierre, J. Tapered single-mode fibers: external refractive-index dependence. *Applied Optics* **25**, 2468-2469 (1986).
- 25 Tai, Y.-H. & Wei, P.-K. Sensitive liquid refractive index sensors using tapered optical fiber tips. *Optics Letters* **35**, 944-946 (2010).
- 26 Bobb, L. C. & Shankar, P. M. Tapered optical fiber components and sensors. *Microwave Journal* **35** (1992).
- 27 Diez, A., Andres, M. V. & Silvestre, E. Tapered optical fiber devices. *SPIE* **3572**, 147-150 (1999).
- 28 Leon-Saval, S. G., Birks, T. A., Wadsworth, W. J. & Russell, P. S. J. Supercontinuum generation in submicron fibre waveguides. *Optics Express* **12** (2004).
- 29 Lou, J., Wang, Y. & Tong, L. Microfiber Optical Sensors: A Review. *Sensors* **14**, 5823-5844 (2014).
- 30 Shi, L. *et al.* Fabrication of submicron-diameter silica fibers using electric strip heater. *Optics Express* **14** (2006).
- 31 Saleh, B. E. A. & Teich, M. C. *Fundamentals of Photonics*. 2nd edn, 332-338 (John Wiley & Sons, Inc., 2007).
- 32 Wagner, D.
<http://www.rpi.edu/dept/phys/Dept2/APPhys1/optics/optics/node17_8.html> (1999).
- 33 RP Fiber Calculator (2014).
- 34 *Refractive index database*, <www.refractiveindex.info> (
35 <<http://www.micromaterialsinc.com/specsFiber.html>> (
36 <http://www.sedi-fibres.com/fr/images_db/page_20.pdf> (
37 Mathematica v. 10.0 (Wolfram, 2014).
- 38 Snyder, A. W. & Love, J. D. *Optical Waveguide Theory*. (Chapman and Hall Ltd, 1983).
- 39 Paschotta, R. *Modes, Photonics Encyclopedia*, <<https://www.rp-photonics.com/modes.html>> (
40 Feit, M. D. & J. A. Fleck, J. Light propagation in graded-index optical fibers. *Applied Optics* **17**, 3990-3998 (1978).
- 41 Olshansky, R. & Keck, D. B. Pulse broadening in graded-index optical fibers. *Applied Optics* **15**, 483-491 (1975).
- 42 Pickrell, G. *et al.* Microstructural Analysis of Random Hole Optical Fibers. *IEEE Photonics Technology Letters* **16**, 491-493 (2004).
- 43 Pickrell, G., Peng, W. & Wang, A. Random-hole optical fiber evanescent-wave gas sensing. *Optics Letters* **29**, 1476-1478 (2004).
- 44 Euser, T. G. *et al.* Dynamic control of higher-order modes in hollow-core photonic crystal fibers. *Optics Express* **16**, 17972-17982 (2008).
- 45 Knight, J. C., Birks, T. A., Cregan, R. F., Russel, P. S. J. & Sandro, J.-P. d. Large mode area photonic crystal fibre. *Electronics Letters* **34** (1998).
- 46 Knight, J. C., Birks, T. A., Russel, P. S. J. & Atkin, D. M. All-silica single-mode optical fiber with photonic crystal cladding. *Optics Letters* **21**, 1547-1579 (1996).

- 47 Russel, P. S. J. Photonic-Crystal Fibers. *Journal of Lightwave Technology* **24**, 4729-4750 (2006).
- 48 Song, Y. B. *et al.* Center-gapped sapphire photonic crystal fiber gas sensor. *ScienceJet* **4** (2015).
- 49 Watanabe, Y., Hotta, T. & Sato, H. Fabrication of flexible photonic crystal using alumina ball inserted Teflon tube. *Applied Physics A* **100**, 981-985, doi:10.1007/s00339-010-5906-7 (2010).
- 50 Gotz, R., Mizaikoff, B. & Kellner, R. in *Progress in Fourier Transform Spectroscopy* Vol. 14 *Mikrochimica Acta Supplement* 833-835 (1997).
- 51 Stiegel, G. J., Romanosky, R. R., Maley, S. M. & Wang, A. (U.S. Department of Energy, 2009).
- 52 Pfeiffenberger, N., Pickrell, G., Kokal, K. & Wang, A. Sapphire photonic crystal fibers. *Optical Engineering* **49**, 090501-090501 through 090501-090503 (2010).
- 53 Pfeiffenberger, N. T. & Pickrell, G. R. Modal reduction in 6-rod bundled single-crystal sapphire photonic crystal fibers. *Proc. of SPIE* **8370**, 837004-837001 through 837004-837008 (2012).
- 54 Tong, L., Lou, J. & Mazur, E. Single-mode guiding properties of subwavelength-diameter silica and silicon wire waveguides. *Optics Express* **12**, 1025-1035 (2004).
- 55 Nicholson, J. W., Yablon, A. D., Fini, J. M. & Mermelstein, M. D. Measuring the Modal Content of Large-Mode-Area Fibers. *IEEE Journal of Selected Topics in Quantum Electronics* **15**, 61-71 (2009).
- 56 Blin, S. *et al.* in *ECOC 2009* Vol. Paper P1.16 (Vienna, Austria, 2009).
- 57 Soh, D. B. Ph. D. thesis, Southampton University, (2005).
- 58 Carpenter, J. & Wilkinson, T. D. Characterization of Multimode Fiber by Selective Mode Excitation. *Journal of Lightwave Technology* **30**, 1386-1393 (2012).
- 59 Stepniak, G., Maksymiuk, L. & Siuzdak, J. Binary-Phase Spatial Light Filters for Mode-Selective Excitation of Multimode Fibers. *Journal of Lightwave Technology* **29**, 1980-1988 (2011).
- 60 Eijkelenborg, M. A. v. *et al.* Microstructured polymer optical fibre. *Optics Express* **9**, 319-317 (2001).
- 61 Ranka, J. K., Windeler, R. S. & Stentz, A. J. Visible continuum generation in air-silica microstructure optical fibers with anomalous dispersion at 800nm. *Optics Letters* **25**, 25-27 (2000).
- 62 Hecht, E. *Optics*. 5th edn, (Addison-Wesley, 2015).
- 63 Paschotta, R. in *RP Photonics Encyclopedia of Laser Physics and Technology* (2015).
- 64 *NA of Sapphire Fiber*, <http://micromaterialsinc.com/NA_sapphireFiber.pdf> (2015).
- 65 Chamberlain, G. E. *et al.* *Optical Fiber Characterization: Attenuation, Frequency Domain Bandwidth, and Radiation Patterns*. Vol. 2 (Electromagnetic Technology Division, Center for Electronics and Electrical Engineering, National Bureau of Standards, 1983).
- 66 Corning. *MM20* (2001).
- 67 Corning. *P11344* (2007).
- 68 Chandani, S. M. & Jaeger, N. A. F. Fiber-Optic Temperature Sensor Using Evanescent Fields in D Fibers. *IEEE Photonics Technology Letters* **17**, 2706-2708 (2005).
- 69 Falco, L., Berthou, H., Cochet, F., Scheja, B. & Parriaux, O. Temperature Sensor using single mode fiber evanescent field absorption. *SPIE Fiber Optic Sensors* **586** (1985).

- 70 Messica, A., Greenstein, A. & Katzir, A. Fiber-optic evanescent wave sensor for gas
detection. *Optics Letters* **19**, 1167-1169 (1994).
- 71 Gaston, A., Lozano, I., Perez, F., Auza, F. & Sevilla, J. Evanescent wave optical-fiber
sensing (temperature, relative humidity, and pH sensors). *IEEE Sensors Journal* **3**, 806-
811 (2003).
- 72 Hill, C. *et al.* Submicron diameter single crystal sapphire optical fiber. *Materials Letters*
138, 71-73 (2015).
- 73 Kirby, K. W. *Processing of Sapphire Surfaces for Semiconductor Applications* Master of
Science thesis, The Pennsylvania State University, (2008).
- 74 Williams, K. R. Etch Rates for Micromachining Processing. *Journal of*
Microelectromechanical Systems **5**, 256-270 (1996).
- 75 Reisman, A., Berkenblit, M., Cuomo, J. & Chan, S. A. The Chemical Polishing of
Sapphire and MgAl Spinel. *J. of Electrochem. Sci.* **118**, 1653-1657 (1971).
- 76 F. Dwikusama, D. S., T. F. Kuech. Study on Sapphire Surface Preparation for III-Nitride
Heteroepitaxial Growth by Chemical Treatments. *J of Electrochem Soc* **149**, G603-G608
(2002).
- 77 Wang, J. *et al.* Fabrication of Patterned Sapphire Substrate by Wet Chemical Etching for
Maskless Lateral Overgrowth of GaN. *Journal of the Electrochemical Society* **153**, C182-
C185 (2006).
- 78 Vardiman, R. G. The Chemical Polishing and Etch Pitting of Sapphire. *Journal of the*
Electrochemical Society **118**, 1804-1809 (1971).
- 79 Alford, W. J. & Stephens, D. L. Chemical Polishing and Etching Techniques for Al₂O₃
Single Crystals. *Journal of the American Ceramic Society* **46**, 193-194 (1963).
- 80 LLC, P. M.-O. (2014).
- 81 Lin, H.-C., Lin, R.-S., Chyi, J.-I. & Lee, C.-M. Light Output Enhancement of Ingan
Light-Emitting Diodes Grown on Masklessly Etched Sapphire Substrates. *Photonics*
Technology Letters IEEE **20**, 1621-1623 (2008).
- 82 Lee, Y.-J. *et al.* Study of Gan-Based Light-Emitting Diodes Grown on Chemical Wet-
Etching Patterned Sapphire Substrate with V-shaped Pits Roughening Surfaces. *Journal*
of Lightwave Technology **26**, 1455-1463 (2008).
- 83 Ridley, M. K., Wesolowski, D. J., Palmer, D. A., Benezeth, P. & Kettler, R. M. Effect of
Sulfate on the Release Rate of Al³⁺ from Gibbsite in Low-Temperature Acidic Waters.
Environmental Science and Technology **7**, 1922-1925 (1997).
- 84 Stachel, D., Svoboda, I. & Fuess, H. Phosphorus pentoxide at 233K. *Acta Cryst.* **C51**,
1049-1050 (1995).
- 85 F. Dwikusama, D. S., T. F. Kuech. Study on Sapphire Surface Preparation for III-Nitride
Heteroepitaxial Growth by Chemical Treatments. *Journal of the Electrochemical Society*
149, G603-G608 (2002).
- 86 Souder, W. & Hidnert, P. Measurements on the Thermal Expansion of Fused Silica.
Scientific Papers of the Bureau of Standards **21**, 1-30.
- 87 Dobrovinskaya, E. R., Lytvynov, L. A. & Pishchik, V. *Sapphire: Material,*
Manufacturing, Applications. 66-67 (Springer, 2009).
- 88 *Glass Properties for Various Glass Compositions used in Vitrocom products,*
<https://www.vitrocom.com/glass_facts.php> (
- 89 *Pyrophosphoric Acid,* <https://en.wikipedia.org/wiki/Pyrophosphoric_acid> (

- 90 *Phosphoric Acids and Phosphates*,
<https://en.wikipedia.org/wiki/Phosphoric_acids_and_phosphates#Polyphosphoric_acids> (
> (
91 MacDonald, D. I. & Boyack, J. R. Density, Electrical Conductivity, and Vapor Pressure
of Concentrated Phosphoric Acid. *Journal of Chemical and Engineering Data* **14**, 380-
384 (1969).
92 *Phosphorus Pentoxide*, <https://en.wikipedia.org/wiki/Phosphorus_pentoxide> (
93 Aota, N., Aida, H., Kimura, Y., Kawamata, Y. & Uneda, M. Fabrication Mechanism for
Patterned Sapphire Substrates by Wet Etching. *ECS Journal of Solid State Science and
Technology* **3**, N69-N74 (2014).
94 Sun, J., Timurdogan, E., Yaacobi, A., Hosseini, E. S. & Watts, M. R. Large-scale
nanophotonic phased array. *Nature* **493**, 195-199 (2013).

APPENDIX A: REFRACTIVE INDEX OF SAPPHIRE VS. WAVELENGTH

Meller Optics, Inc.				
Optics and Electro-Optics for Lasers, Industry, and Defense				
Sapphire Index of Refraction Table				03/11/02
Values at 20 ° C.				
Ordinary ray along C axis, extraordinary ray normal to C axis.				
λ μm	Ordinary Ray	Extraordinary Ray	Difference (Or - Ex)	% Change (Diff / Ord)
0.200	1.91271	1.90163	0.01108	0.58%
0.240	1.85446	1.84453	0.00993	0.54%
0.280	1.82437	1.81509	0.00928	0.51%
0.320	1.80604	1.79752	0.00852	0.47%
0.360	1.79467	1.78604	0.00863	0.48%
0.400	1.78652	1.77807	0.00845	0.47%
0.440	1.78059	1.77226	0.00833	0.47%
0.480	1.77610	1.76768	0.00842	0.47%
0.520	1.77260	1.76444	0.00816	0.46%
0.560	1.76980	1.76169	0.00811	0.46%
0.600	1.76750	1.75944	0.00806	0.46%
0.640	1.76558	1.75755	0.00803	0.45%
0.680	1.76394	1.75594	0.00800	0.45%
0.720	1.76252	1.75454	0.00798	0.45%
0.760	1.76126	1.75331	0.00795	0.45%
0.800	1.76013	1.75220	0.00793	0.45%
0.840	1.75911	1.75119	0.00792	0.45%
0.880	1.75817	1.75026	0.00791	0.45%
0.920	1.75729	1.74940	0.00789	0.45%
0.960	1.75646	1.74858	0.00788	0.45%
1.000	1.75568	1.74781	0.00787	0.45%
1.300	1.75043	1.74260	0.00783	0.45%
1.500	1.74705	1.73924	0.00781	0.45%
1.700	1.74351	1.73572	0.00779	0.45%
1.900	1.73971	1.73194	0.00777	0.45%
2.100	1.73558	1.72784	0.00774	0.45%
2.300	1.73110	1.72339	0.00771	0.45%
2.500	1.72623	1.71855	0.00768	0.44%
2.700	1.72095	1.71331	0.00764	0.44%
2.900	1.71523	1.70765	0.00758	0.44%
3.100	1.70907	1.70155	0.00752	0.44%
3.300	1.70243	1.69500	0.00743	0.44%
3.500	1.69531	1.68798	0.00733	0.43%
3.700	1.68768	1.68047	0.00721	0.43%
3.900	1.67951	1.67245	0.00706	0.42%
4.100	1.67080	1.66391	0.00689	0.41%
4.300	1.66151	1.65482	0.00669	0.40%
4.500	1.65161	1.64517	0.00644	0.39%
4.700	1.64108	1.63492	0.00616	0.38%
4.900	1.62989	1.62406	0.00583	0.36%
5.100	1.61799	1.61255	0.00544	0.34%
5.300	1.60536	1.60036	0.00500	0.31%
5.500	1.59195	1.58746	0.00449	0.28%

APPENDIX B: MATHEMATICA CODE

The following code was input to Wolfram Mathematica to calculate various plots and models generated in the theoretical segments of this work.

Appendix B.1: Modal Volume Measurement

Mode Counting

```
a =;  
n1 =;  
n2 =;  
\[Lambda] =;  
Where  
a = fiber radius in nanometers  
n1 = core refractive index  
n2 = cladding refractive index  
\[Lambda] = wavelength in nanometers  
NA = (n1^2 - n2^2)^(1/2);  
V = 2*Pi*a/\[Lambda]*NA  
modeestimatelargeV = 4/Pi^2*V^2  
modeestimateV = V^2/2  
k0 = (2*Pi)/\[Lambda];  
kT = (n1^2*k0^2 - \[CapitalBeta]^2)^(1/2);  
\[Gamma] = (\[CapitalBeta]^2 - n2^2*k0^2)^(1/2);  
Y = (V^2 - X^2)^(1/2);  
l = 1;  
LHS = X*(BesselJ[l + 1, X]/BesselJ[l, X]);  
RHS = Y*(BesselK[l + 1, Y]/BesselK[l, Y]);  
Plot[{LHS, RHS}, {X, 0, V}]  
intersections = {X, LHS} /. NSolve[{LHS == RHS, 0 <= X <= V}, X]  
modenum = Length[intersections]  
Plot[{LHS, RHS}, {X, 0, V}, PlotLegends -> "Expressions",  
Exclusions -> {Denominator[LHS] == 0},  
Epilog -> {Red, AbsolutePointSize[6],  
Tooltip[Point[#, #] & /@ intersections]}
```

Appendix B.2: Core Confinement

Independent Variables

$$n1=;$$

$$n2=;$$

$$a=;$$

$$d=;$$

$$\lambda=;$$

$$k=;$$

$$\epsilon_0=8.85418782*10^{-12};$$

$$\mu_0=1.25663706*10^{-6};$$

Where

n1= refractive index of core

n2= refractive index of cladding (air)

a= fiber radius in nanometers

λ = wavelength in nanometers (3500nm absorption peak for methane)

ϵ_0 = electric constant; permittivity of free space ($m^{-3} kg^{-1} s^4 A^2$)

μ_0 = magnetic constant; permeability of free space ($(m kg)/(s^2 A^2)$)

Update value for Usc from table if λ , a, n1, or n2 are changed

Equations

$$V=k*a*(n1^2 - n2^2)^{\frac{1}{2}}$$

$$\Delta=(1-n2^2/n1^2)/2;$$

$$\beta_{sc}=V/(a*(2*\Delta)^{\frac{1}{2}})*\left(1-\frac{4*\Delta}{V}\right)^{\frac{1}{2}}$$

$$NA=(n1^2-n2^2)^{1/2};$$

$$kT=(n1^2 * k_0^2 - B^2)^{\frac{1}{2}};$$

$$\gamma=(B^2 - n2^2 * k_0^2)^{\frac{1}{2}};$$

$$Y=(V^2 - X^2)^{\frac{1}{2}};$$

$$l=0;$$

$$LHS=X*(BesselJ[l+1,X]/BesselJ[l,X]);$$

$$RHS=Y*(BesselK[l+1,Y]/BesselK[l,Y]);$$

$$\text{Plot}\{\{LHS,RHS\},\{X,0,V\}\}$$

$$\text{intersections}=\{X,LHS\}/.\text{NSolve}\{\{LHS==RHS,0<=X<=V\},X\}$$

$$Xn=\text{Part}[\text{intersections},1,1];$$

$$kTn=Xn/a;$$

$$\beta=(n1^2 * k^2 - kTn^2)^{\frac{1}{2}};$$

$$R=r/a;$$

$$U=(d*(k^2 * n1^2 - \beta^2)^{\frac{1}{2}})/2;$$

$$W=(d*(\beta^2 - k^2 * n2^2)^{\frac{1}{2}})/2;$$

$$Jv=BesselJ[1,U];$$

$$Kv = \text{BesselK}[1, W];$$

$$HEeq = (Jv'/(U*Jv) + Kv'/(W*Kv)) * (Jv'/(U*Jv) + (n1^2 * Kv')/(n1^2 * W * Kv)) == (\beta/(k*n1))^2 * (V/(U*W))$$

$$a1 = (F2 - 1)/2;$$

$$a3 = (F1 - 1)/2;$$

$$a5 = (F1 - 1 + 2 * \Delta)/2;$$

$$a2 = (F2 + 1)/2;$$

$$a4 = (F1 + 1)/2;$$

$$a6 = (F1 + 1 - 2 * \Delta)/2;$$

$$F1 = ((U*W)/V)^2 * (b1 + (1 - 2 * \Delta) * b2);$$

$$F2 = (V/(U*W))^2 * 1/(b1 + b2);$$

$$b1 = 1/(2 * U) * (J0/J1 - J2/J1);$$

$$b2 = -1/(2 * W) * (K0/K1 + K2/K1);$$

$$J0 = \text{BesselJ}[0, U];$$

$$J1 = \text{BesselJ}[1, U];$$

$$J2 = \text{BesselJ}[2, U];$$

$$K0 = \text{BesselK}[0, W];$$

$$K1 = \text{BesselK}[1, W];$$

$$K2 = \text{BesselK}[2, W];$$

$$J0R = \text{BesselJ}[0, U * R];$$

$$J2R = \text{BesselJ}[2, U * R];$$

$$K0R = \text{BesselK}[0, W * R];$$

$$K2R = \text{BesselK}[2, W * R];$$

Z-Components of Poynting Vectors
Inside the Core ($0 < r < a$)

$$sz1 = 1/2 * \left(\frac{\epsilon_0}{\mu_0}\right)^{\frac{1}{2}} * ((k * n1^2)/(\beta * J1^2)) * (a1 * a3 * J0R^2 + a2 * a4 * J2R^2 + (1 - F1 * F2)/2 * J0R * J2R * \text{Cos}[2 * \phi]);$$

$$sz1lin = 1/2 * \left(\frac{\epsilon_0}{\mu_0}\right)^{\frac{1}{2}} * ((k * n1^2)/(\beta * J1^2)) * (a1 * a3 * J0R^2 + a2 * a4 * J2R^2 + (1 - F1 * F2)/2 * J0R * J2R);$$

Outside the Core ($a < r < \text{inf}$)

$$sz2 = 1/2 * \left(\frac{\epsilon_0}{\mu_0}\right)^{\frac{1}{2}} * ((k * n1^2)/(\beta * K1^2)) * (U^2/W^2) * (a1 * a5 * K0R^2 + a2 * a6 * K2R^2 - (1 - 2 * \Delta - F1 * F2)/2 * K0R * K2R * \text{Cos}[2 * \phi]);$$

$$sz2lin = 1/2 * \left(\frac{\epsilon_0}{\mu_0}\right)^{\frac{1}{2}} * ((k * n1^2)/(\beta * K1^2)) * (U^2/W^2) * (a1 * a5 * K0^2 + a2 * a6 * K2^2 - (1 - 2 * \Delta - F1 * F2)/2 * K0 * K2);$$

$$\text{core} = \text{Plot}[sz1lin, \{r, 0, a\}]$$

$$\text{clad} = \text{Plot}[sz2lin, \{r, a, 5000\}]$$

$$\text{Show}[\text{core}, \text{clad}, \text{PlotRange} \rightarrow \{\{0, 1000\}, \{0, 0.01\}\}]$$

$$\text{Clear}[a];$$

$$\text{intsz1} = \text{Integrate}[sz1, \{r, 0, a\}, \{\phi, 0, 2 * \text{Pi}\}];$$

$$\text{intsz2} = \text{Integrate}[sz2, \{r, a, \text{Infinity}\}, \{\phi, 0, 2 * \text{Pi}\}];$$

$$\eta = \text{intsz1}/(\text{intsz1} + \text{intsz2});$$

```
confine=Plot[η, {a, 0, 500}, PlotRange -> {{0, 500}, {0, 1}}, AxesLabel -> {"Fiber  
Radius(nm)", "Confinement Fraction"}, GridLines -> Automatic, GridLinesStyle -  
> Directive[Gray, Dashed]]
```